Title
Biomechanical Modeling Applications for Function-Preserving Lung Interventions

Author
Stiehl, Brad

Publication Date
2022

Peer reviewed|Thesis/dissertation

UNIVERSITY OF CALIFORNIA

Los Angeles

Biomechanical Modeling Applications for Function-Preserving Lung Interventions

A dissertation submitted in partial satisfaction of the

requirements for the degree Doctor of Philosophy in

Physics and Biology in Medicine

by

Bradley Joseph Stiehl

2022

ABSTRACT OF THE DISSERTATION

Biomechanical Modeling Applications for Function-Preserving Lung Interventions

by

Bradley Joseph Stiehl

Doctor of Philosophy in Biomedical Physics

University of California, Los Angeles, 2022

Professor Anand Prasad Santhanam, Co-Chair

Professor Daniel Abraham Low, Co-Chair

The measurement of the elastic properties of human tissue, or elastography, allows for the quantitative assessment of tissue functionality. Patients undergoing radiation therapy often present with lung disease, such as COPD, which is known to cause degradation of tissue elasticity. The reliance of normal lung function on these elastic properties is well established, underscoring the importance of function-preserving efforts in radiotherapy. Regional elasticity distributions may be used to identify regions of parenchymal tissue that contribute significantly to lung function. This knowledge can, in turn, aid in functional lung sparing efforts during the treatment planning process. Previous elastography efforts have been performed using a well-validated biomechanical model in combination with model-based CT images. Recent studies also suggest that biomechanical modeling and elasticity estimation may prove to have useful applications outside of the radiotherapy domain. These tools could potentially help improve the evaluation of patient candidacy and outcome prediction for various lung interventions, such as lung volume reduction surgery (LVRS) or bronchoscopic lung volume reduction (BLVR) procedures.

The first aim of the dissertation was to develop and improve current CT-based elastography algorithms and tools. This aim was addressed by carrying out a consistency study where elastography was performed using separate image datasets generated from scans acquired at different points in the breathing trace for each patient. As part of a feasibility study to test the hypothesis that additional elasticity information could be obtained using large deformation image pairs, an elastography method was developed for use with breath-hold CT images acquired at the forced breathing stages of residual volume (RV) and total lung capacity (TLC). The second aim was to investigate the applications of biomechanical modeling and elastography for other function-preserving treatment interventions. This work involved the development of a quorum-based machine learning approach to perform lobar segmentation for lobe identification in lung intervention simulations and lobe-wise analyses. A framework for simulating a lobectomy procedure by incorporating elasticity information and biomechanical modeling was also constructed. Using this framework, the feasibility of using the resulting predicted post-intervention lung geometry for approximating pulmonary function test (PFT) values was investigated. The third aim of this proposal was to develop and employ a machine learning application for elasticity estimation from single end-exhalation breath-hold CT scans. A conditional generative adversarial (cGAN) neural network was built and validated for elasticity estimation. We further investigated the effects of the imaging dose used during the acquisition of CT image data on the accuracy of the proposed machine learning implementation.

The expanded use of biomechanical modeling and elastography within the radiotherapy context has the potential to improve functional avoidance efforts for patients presenting with co-morbidities affecting lung function prior to treatment. Additionally, there is an opportunity to extend these tools toward improving and informing other lung intervention efforts. Finally, the

ability to take advantage of CT-based elastography methods through machine learning in scenarios where model-based CT is not typically available could expand the scope of CT-based elastography in both the radiotherapy domain and for the expanded use in other lung intervention workflows. The tools and applications presented in this dissertation aim to highlight and expand the benefits of CT-based biomechanical modeling and elastography within the radiotherapy domain and for use with other lung intervention procedures.

The dissertation of Bradley Joseph Stiehl is approved by:

Michael McNitt-Gray

James Michael Lamb

Daniel Abraham Low, Committee Co-Chair

Anand Prasad Santhanam, Committee Co-Chair

University of California, Los Angeles

2022

To Milo and Romeo

TABLE OF CONTENTS

[1] A version of this chapter has been published as a manuscript in Medical Physics
[2] A version of this chapter has been published as a manuscript in Medical Physics
[3] A version of this chapter has been submitted for review to Medical Physics
[4] A version of this chapter has been published as a manuscript in the International Journal of Computer Assisted Radiology and Surgery
[5] A version of this chapter has been published as a conference proceeding in SPIE Medical Imaging

LIST OF TABLES

LIST OF FIGURES

ACKNOWLEDGMENTS

I'd like to express my immense gratitude to my advisors and the co-chairs of my thesis committee, Dr. Anand Santhanam and Dr. Daniel Low, for being great mentors to me and guiding me in my research. I am constantly inspired by your passion, endless curiosity, and wealth of knowledge. I also want to acknowledge my committee members, Dr. Michael McNitt-Gray and Dr. James Lamb, who have been excellent resources and helped me grow as a researcher and establish the solid foundation on which this work was conducted.

I want to thank the Physics and Biology in Medicine (PBM) program at UCLA for the opportunity to pursue my academic goals. A special thank you to Michael McNitt-Gray and Reth Im for all the hard work that goes into running this program and for the support you have provided me over the years. The PBM faculty, staff, and students are an incredible group of people who elevate and support one another. I feel very lucky to have been a part of this program.

I want to thank my friends and colleagues Michael Lauria, Kamal Singhrao, Louise Naumann, and Caffi Meyer. You have all helped me immensely as a researcher and student. We have also made some great memories together and I look forward to making more in the future. I also want to acknowledge the work of Dr. Katelyn Hasse, Dr. Jack Neylon, and Dr. Dylan O'Connell for their excellent work that preceded and formed the foundation for my dissertation research.

I want to express my deep gratitude to my parents, Joe and Brenda, who have made countless sacrifices and spared no expense to give me every opportunity possible from a young age. I'm so thankful for the tremendous amount of love and support that you have shown me, none of this would be possible otherwise. I'd also like to thank my sister for always inspiring me, supporting me, and being goofy with me.

I want to thank my partner, Taylor, for her love, endless support, and incredible patience throughout this process. We've been through so much together and I am so lucky to have you by my side. I'd also like to thank our cats, Milo and Romeo, who have provided me an immeasurable amount of emotional support, even if they can't understand it.

Chapter 2 is a version of a manuscript published in *Medical Physics*: Stiehl B, Lauria M, O'Connell D, Hasse K, Barjaktarevic I. Z., Lee P, Low D. A., & Santhanam, A. P.. A quantitative analysis of biomechanical lung model consistency using 5DCT datasets. *Med Phys.* 2020;47(11):5555-5567.

Chapter 3 is a version of a manuscript published in *Medical Physics*: Santhanam A. P., Stiehl B, Lauria M, Hasse K, Barjaktarevic I, Goldin J, & Low D. A.. An adversarial machine learning framework and biomechanical model-guided approach for computing 3D lung tissue elasticity from end-expiration 3DCT. *Med Phys*. 2021;48(2):667-675. doi:10.1002/mp.14252

Chapter 4 is a version of a manuscript submitted to *Medical Physics*: Stiehl B, Lauria M, Singhrao K, Barjaktarevic I, Goldin J, Low D. A., & Santhanam A. P.. (2022). A quantitative analysis of lung elastography using large deformation breath-hold CT scans acquired during forced breathing. *Med Phys*. [Submitted].

Chapter 5 is a version of a manuscript published in *International Journal of Computer Assisted Radiology and Surgery*: Stiehl B, Lauria M, Singhrao K, Goldin J, Barjaktarevic I, Low D. A., & Santhanam, A. P.. Scalable quorum-based deep neural networks with adversarial learning for automated lung lobe segmentation in fast helical free-breathing CTs. *Int J Comput Assist Radiol Surg*. 2021;16(10):1775-1784. doi:10.1007/s11548-021-02454-6

Chapter 6 is a version of a conference proceedings published in *SPIE Medical Imaging*: Santhanam A. P., Stiehl B, Lauria M, Barjaktarevic I, Goldin J, Yanagawa J, & Low D. A.. A quantitative prediction of the post-operative lobectomy lung physiology using a GPU-based linear elastic lung biomechanics model and a constrained generative adversarial learning approach. Vol 11598: *SPIE*; 2021.

VITA

EDUCATION

M.S. University of California, Los Angeles 2022
Physics and Biology in Medicine

B.S. Loyola Marymount University 2017
Physics
Minor in Mathematics

PEER-REVIEWED PUBLICATIONS

Stiehl, B., Lauria, M., Singhrao, K., Barjaktarevic, I., Goldin, J., Low, D., & Santhanam, A. (2022). A quantitative analysis of lung elastography using large deformation breath-hold CT scans acquired during forced breathing. Med. Phys. *In Review.*

Stiehl, B., Lauria, M., Singhrao, K., Goldin, J., Barjaktarevic, I., Low, D., & Santhanam, A. (2021). Scalable quorum-based deep neural networks with adversarial learning for automated lung lobe segmentation in fast helical free-breathing CTs. *International journal of computer assisted radiology and surgery*, *16*(10), 1775–1784. https://doi.org/10.1007/s11548-021-02454-6

Santhanam, A., **Stiehl, B.**, Lauria, M., Hasse, K., Barjaktarevic, I., Goldin, J. and Low, D.A. (2021). An adversarial machine learning framework and biomechanical model-guided approach for computing 3D lung tissue elasticity from end-expiration 3DCT. Med. Phys., 48: 667-675. https://doi.org/10.1002/mp.14252

Lauria, M., Singhrao, K., **Stiehl, B.**, Low, D., Goldin, J., Barjaktarevic, I., & Santhanam, A. (2021). Automatic triangulated mesh generation of pulmonary airways from segmented lung 3DCTs for computational fluid dynamics. International Journal of Computer Assisted Radiology and Surgery. doi:10.1007/s11548-021-02465-3

Santhanam, A., **Stiehl, B.,** Lauria, M., Barjaktarevic, I., Goldin, J., Yanagawa, J., & Low, D. (2021). A quantitative prediction of the post-operative lobectomy lung physiology using a GPU-based linear elastic lung biomechanics model and a constrained generative adversarial learning approach (Vol. 11598): SPIE. https://doi.org/10.1117/12.2582271

Stiehl, B., Lauria, M., O'Connell, D., Hasse, K., Barjaktarevic, I.Z., Lee, P., Low, D.A. and Santhanam, A. (2020). A quantitative analysis of biomechanical lung model consistency using 5DCT datasets. Med. Phys., 47: 5555-5567. https://doi.org/10.1002/mp.14323

Hasse, K., Hsieh, S.S., O'Connell, D., **Stiehl, B**., Min, Y., Neylon, J., Low, D.A. and Santhanam, A.P. (2020), Systematic feasibility analysis of performing elastography using reduced dose CT lung image pairs. Med. Phys., 47: 3369-3375. https://doi.org/10.1002/mp.14112

Cao, M., **Stiehl, B**., Yu, V. Y., Sheng, K., Kishan, A. U., Chin, R. K., . . . Ruan, D. (2020). Analysis of Geometric Performance and Dosimetric Impact of Using Automatic Contour Segmentation for Radiotherapy Planning. Frontiers in Oncology, 10(1762). https://doi.org/10.3389/fonc.2020.01762

SELECTED CONFERENCE PRESENTATIONS

"Scalable quorum-based deep neural networks with adversarial learning for automated lung lobe segmentation in fast helical free-breathing CTs. International journal of computer assisted radiology and surgery," Computer Assisted Radiology and Surgery (CARS) Conference 2021. Munich, Germany (Virtual). June 21, 2021.
"A Quantitative Analysis of Lung Elastography Performance Using Large-Deformation CT Scans Acquired at Residual Volume (RV) and Total Lung Capacity (TLC)," AAPM 63rd Annual Meeting 2021. Columbus, Ohio (Virtual). July 26, 2021.

"Quantitative Analysis of Lung Elastography Using Free Breathing Fast Helical CT Scans," AAPM 62nd Annual Meeting 2020. Vancouver, Canada (Virtual). July 12, 2020.

"Improving Deformable Image Registration of 4DCTs Using a Generative Adversarial Deep Neural Network for Automated Lung Lobe Segmentation," AAPM 61st Annual Meeting 2019. San Antonio, Texas. July 18, 2019.

"On the Quantitative Analysis of Biomechanical Lung Model Consistency Using 5DCT Datasets. Scientific Abstracts and Sessions," AAPM 61st Annual Meeting 2019. San Antonio, Texas. July 14, 2019.

CHAPTER 1: INTRODUCTION TO THE DISSERTATION

1.1 Motivation

Radiation therapy is a key step in an often multi-faceted course of treatment for patients diagnosed with lung cancer.[1] However, patients undergoing radiotherapy can experience severe radiation-induced lung injuries to healthy tissue when exposed to excess dose.[2] The risk of treatment-related injury is further increased in patients with pre-existing lung diseases such as interstitial lung disease and chronic obstructive pulmonary disorder (COPD), which is found in 40-70% of patients.[3,4] Furthermore, greater rates of post-treatment side-effects and mortality have been observed in lung cancer patients with co-morbidities.[5,6] Therefore, a better understanding of patient-specific underlying regional lung function is necessary to identify and minimize risk for these patients. Recent advancements in treatment planning techniques and treatment delivery technologies have allowed for the sparing of identified functional lung regions.[7,8] To more accurately inform functional avoidance efforts in treatment planning for lung radiotherapy, we propose a biomechanical model-based CT elastography approach that considers the dynamic component of lung motion.

Outside of the radiotherapy domain, lung cancer patients with tumors localized to a single lobe of the lung are often considered for a lung lobectomy procedure, the surgical removal of one or more identified lung lobes.[9] Additionally, patients with severe lung disease may also be considered for surgical or interventional volume reduction procedures targeting low- or non-functioning lobe(s) of the lung.[10] These volume reduction procedures have been shown to increase overall lung function through the removal of non-functioning lung tissue and/or air trapped within non-functional regions of the lung.[11] While these methods have proven successful for some

patients, patient candidacy and outcome evaluation are limited to the review of quantitative CT measurements, such as RA950, standard pulmonary function tests (PFTs), and exercise tests.[12,13] These methods of patient evaluation and follow-up provide only overall patient lung function information but do not provide the regional lung function information necessary to fully understand complex patient-specific lung function before and following a procedure. We propose a biomechanical modeling approach, in combination with elasticity estimation, to predict post-interventional lung geometries and PFT results.

1.2 Background

1.2.1 Radiation Therapy and Radiation-Induced Lung Injuries

Lung cancer is the leading cause of cancer death in both men and women in the U.S., as reported by the Centers For Disease Control and Prevention (CDC) as recently as 2020, accounting for over 23% of all cancer deaths.[14] With over 218,000 new cases of lung cancer recorded in 2018 alone, radiation therapy is often prescribed as either a main treatment, following surgical tumor removal, or in coordination with systemic therapies, such as chemotherapy.[15,16] In fact, a recent study suggests that an increasing number of lung cancer patients, 77% of the cases reviewed, presented with an evidence-based indication for radiotherapy across all stages of disease.[17]

For some patients, thoracic radiotherapy can lead to the occurrence of a severe complication called radiation-induced lung injury (RILI). RILI may present acutely as radiation pneumonitis (RP) or chronically in the form of pulmonary fibrosis (PF) for up to 25% of lung cancer patients treated with radiation.[18] A recent review article by Arroyo-Hernández et al. stated that predisposing factors for RILI could be either treatment-related (lung dose, fractionation, chemotherapy, other concurrent treatments) or patient-related (smoking history, comorbidities, demographics, and genetics). Studies investigating the relationship between RILI and pre-existing

conditions, such as COPD, interstitial lung disease (ILD), and pulmonary emphysema, have reported higher incidence rates of radiation pneumonitis in patients with these comorbidities.[6,19-22]

1.2.2 Functional Lung Avoidance

Previous approaches for identifying functional lung regions for use in normal tissue sparing efforts during radiotherapy treatment planning include the use of magnetic resonance (MR), ultrasound (US), and single-photon emission computed tomography (SPECT) imaging.[23-25] However, these methods are limited due to their requirement of image modalities not currently present in a conventional radiotherapy setup. The use of CT is ideal for ventilation imaging and functional lung identification because it is already acquired, due to the reliance of dose calculation on electron density information. For this reason, CT ventilation and perfusion imaging have been proposed and investigated in multiple clinical trials.[24-27] In addition, more recently developed dose delivery methods like stereotactic body radiation therapy (SBRT) have been shown to be effective in the reduction of delivered dose to identified functional lung tissue.[26-28] The delivery of hypofractionated treatments, relatively large doses in fewer fractions compared to conventional methods, with a rapid isotropic dose fall-off from the tumor volume to surrounding normal tissue can be achieved with these approaches.[7,8] We envision the development of a CT-based characterization of patient lung function for function-preserving efforts during lung radiotherapy due to the availability of the imaging modality throughout the course of treatment.

1.2.3 Lobectomy and Lung Volume Reduction Strategies

Lobectomy procedures are one of the most common surgical approaches to treating early-stage non-small cell lung cancer (NSCLC).[29,30,31] The surgical removal of a lobe of the lung may reduce pulmonary function or capacity, patients undergo screening to predict the occurrence of postoperative pulmonary complications (PPC).[32] Advances in surgical techniques, such as minimally invasive approaches and sub-lobar resections, in combination with enhanced

perioperative care, have led to improved outcomes. This new paradigm is causing some to reevaluate the criteria by which patients are evaluated for operative candidacy.[33] For all lobectomy strategies, patient selection remains critical to ensuring clinically acceptable PPC and mortality rates.[34]

Many surgical approaches to treating dyspnea, emphysema, and other conditions and symptoms associated with severe lung disease have been investigated. However, some of the proposed procedures including costochondrectomy, phrenic crush, pneumoperitoneum, pleural abrasion, lung denervation, and thoracoplasty, did not produce the desired outcomes while also subjecting patients to the inherent risks associated with an invasive surgical procedure.[35]

One surgical procedure that initially proved beneficial to patients with acceptable mortality and morbidity rates was lung volume reduction surgery (LVRS).[36,37] As an alternative to lung transplantation, LVRS exhibits lower associated mortality and removes the need for a donor organ to become available, which typically consists of strict patient selection criteria and placing the patient on a lengthy waiting list.[38] Despite the stated benefits to patients who prove to be good candidates through presenting with necessary indications and a series of pre-operative workups, LVRS is considered an underutilized therapy in the US due to the assumed risk and high cost associated with the surgical procedure.[12]

An alternative, less invasive procedure currently being investigated is bronchoscopic lung volume reduction (BLVR), the placement of endobronchial valves inserted bronchoscopically to occlude an emphysematous lobe of the lung.[39] This approach aims to achieve partial or full lobar atelectasis and results in a similar reduction of hyperinflation as the previously described LVRS approach. The first randomized clinical trial of Zephyr Endobronchial Valves (Zephyr EBV, Pulmonx Corporation) was the VENT (Endobronchial Valve for Emphysema Palliation Trial), in

which the assessed endpoints of FEV1 and 6-minute-walk distance (6MWD) showed statistically significant but not clinically meaningful improvements.[40,41] There is a need for developing additional measures of patient candidacy and outcome prediction for these procedures to aid pulmonologists and surgeons. Tools to assist experts in these decision-making processes could be developed through a combination of applications such as biomechanical modeling, tissue property estimations, and machine learning applications.

1.2.4 Biomechanical Modeling

Biomechanical models of human anatomy are critical in understanding physiology and have been developed for applications ranging from deformable image registration (DIR) to image-guided treatment planning.[42,43] Such approaches have been used by peers to model complex motions of the face, neck, jaw, torso, hand, normal lungs, and the leg for purposes of surgical intervention, surgical guidance, forensics, and biomechanical impact studies.[44-47] In the context of radiotherapy, biomechanical models have been shown to be applicable for computing biomechanical changes caused by patient posture, physiological regression, and co-morbidities. For instance, biomechanical models of the lungs have been demonstrated to be useful for identifying regions with co-morbidities such as COPD, a progressive lung disease characterized by a reduction of airflow and hindrance of normal breathing efforts in patients due to narrowed airways.[48-51]

In a previous work by Neylon et al., GPU-accelerated patient-specific finite element biomechanical models were developed and validated to improve head and neck image registration.[52] This biomechanical modeling effort has since been extended to other anatomical sites including the liver, breast, and lung.[53-55] This has also allowed for the ability to perform physics-based deformations of patient anatomy and measure specific biomechanical properties.

1.2.5 Elastography

Several methods, using various imaging modalities, have been identified for measuring the elastic properties of human tissues, such as the breast, liver, and lungs.[56-58] Specifically, magnetic resonance elastography (MRE) has been proposed for estimating lung tissue elasticity.[59-61] Ultrasound (US) elastography has also been used to measure the elasticity of tumor characteristics and lung disease assessment.[62,63] However, the use of these elastography methods within the radiotherapy setup has yet to be systematically investigated due to the need for an additional imaging step in the radiotherapy treatment planning workflow. There is a need to employ elastography methods for the lung anatomy using imaging modalities that are already in use within the clinical radiotherapy workflow, such as CT imaging.[64]

A quantitative measure of lung function has been identified in the measurement of the elastic properties of the parenchymal lung tissue. Normal lung function depends on the production of elastin and the presence of elastic fibers throughout the lung parenchyma and the inhibition of production or degradation of existing fibers can result in lung dysfunction and diseases, such as COPD.[50,65,66] An established elastography method using motion-model generated images has been previously developed and validated for the accurate estimation of patient lung elasticity.[51,67] The approach allows for elasticity distributions to be estimated by a biomechanical model, which is informed by deformably registered pairs of breath-hold CT images that are generated according to a motion model assembled from a series of FHFBCT scans.[68] There is ample opportunity to advance and improve upon the current implementation of CT-based elastography, as well as expand potential uses throughout the radiotherapy treatment workflow. Furthermore, additional uses of elastography may be investigated for other lung interventions where an understanding and assessment of regional lung function assessment is important.

1.3 Specific Aims

One goal of this dissertation is to continue investigating and expanding the uses of CT-based biomechanical modeling and elastography for improving functional lung avoidance efforts in radiation therapy. The second goal is to extend these tools for use in other function-preserving lung interventions. The first aim, to further develop and improve current lung elastography methods, was addressed by conducting a consistency study evaluating results obtained using images acquired during different points in the patient breathing trace. Additionally, an elastography approach was developed using large deformation datasets acquired during a forced breathing maneuver that may provide additional elasticity information when compared to free-breathing datasets. The second aim of this work was to develop biomechanical modeling applications for function-preserving lung interventions outside of the radiotherapy domain. The first step taken to address this aim was the development of a quorum-based machine learning approach for lobar segmentation, for accurate lobe identification. Feasibility studies were also carried out in which post-operative lung geometries and PFT results were predicted through biomechanical simulation. The third aim was to develop a framework for performing elasticity estimation from a single breath-hold CT scan. A machine learning approach to CT-based lung elasticity estimation was investigated to address this aim. In addition, the effect of simulated reduced dose images on the accuracy of the machine learning-based elastography method was studied.

Specific Aim 1 (SA1): Develop and improve upon current elastography algorithms and tools.

1. Conduct a consistency study evaluating the results of a CT-based elastography method with two separate sets of 5DCT pseudo-breath-hold images acquired at different points in a patient breathing trace.

2. Investigate the feasibility of elastography with breath-hold CT images acquired during the forced breathing stages of residual volume (RV) and total lung capacity (TLC) for obtaining additional elasticity information.

Specific Aim 2 (SA2): Demonstrate biomechanically modeled function-preserving treatment interventions.

1. Develop a quorum-based machine learning approach to lung lobe segmentation for acquiring lobe-wise boundary constraints and performing lobe-wise analyses.
2. Estimate lobectomy and lung lobe volume reduction post-procedure lung geometries.
3. Predict post-operative pulmonary function test (PFT) results using generated post-procedure lung geometries.

Specific Aim 3 (SA3): Develop methods for performing elasticity estimation from single end-exhalation breath-hold CT scans.

1. Formulate a machine learning algorithm for generating elasticity from a single end-expiration breath-hold CT scan.
2. Evaluate the effects of imaging dose on a machine learning algorithm's ability to produce accurate elasticity results.

1.4 Overview

In this dissertation, Chapters 2-6 are versions of manuscripts that have been published or are under review in peer-reviewed academic journals and conference proceedings. The following is a breakdown of chapters and the stated Specific Aims that they address. Chapter 2 addresses SA1.1 through a study of the consistency of an elastography method when using image data acquired at different points in a patient breathing phase. SA1.2 Is addressed in Chapter 3 through a feasibility study in which the elastography approach is applied to large deformation breath-hold images acquired at forced breathing. Chapter 4 addresses SA3.1 and 3.2 through the development

and evaluation of a machine learning-based approach to performing elasticity estimation with a single breath-hold CT scan. SA2.1 is addressed in Chapter 5, in which a quorum-based machine learning application is proposed for the task of lung lobe segmentation. Chapter 6 addresses SA2.1 and 2.2 through a proposed method of post-lung intervention lung geometry estimation and pulmonary function prediction.

CHAPTER 2: A quantitative analysis of biomechanical lung model consistency using 5DCT datasets

Biomechanical lung model consistency analysis

A version of this chapter has been published as a manuscript: Med Phys, Vol. 47, No. 11, 2020. doi: 10.1002/mp.14323

2.1 Introduction

Normal lung function is dependent on the elasticity (Young's Modulus) of the lung tissue and diseases such as COPD cause a loss in tissue elasticity.[49] This results in air-trapping in the lungs upon exhalation and an increase in difficulty breathing as documented by studies of excised tissue of lung disease patients who exhibited variations in biomechanical properties of lung parenchyma.[69,70] The current gold-standard spirometry-based measures of disease onset and staging are unable to characterize regional lung tissue mechanics.[71] Recent efforts made to identify voxel-specific COPD phenotypes (emphysema, gas-trapping, and small airways disease) include post-processing and deformable registration techniques of inspiratory and expiratory CT lung scans.[72-74] However, these methods are limited by their inability to sufficiently represent the underlying tissue physiology.[75] The overall goal of this area of research is to achieve a quantitative understanding of lung physiology by measuring the regional lung elasticity using a biomechanically-guided procedure. In our previous research effort, a novel biomechanically-guided elastography method, performed via an in-house GPU-driven physics-based biomechanical model, has been proposed and validated.[50] The accuracies of the measurements were systematically validated using soft phantoms that can deform for a given known distribution of boundary constraints and elasticity distribution. Furthermore, lung tissue elasticity measured using the biomechanical model has been established as a biomarker in determining disease staging,

designating new endpoints in clinical trials, and developing new targeted treatments for COPD patients.[51]

A critical analysis that needs to be performed and documented is the consistency of the estimated elasticity. The consistency, in this case, refers to the repeatability with which the elasticity can be measured for a given patient when a new set of images are employed and when no physiologic change in elasticity is expected. For example, if the images are formed from data acquired at the same imaging session but at different times. We employed a well-validated 5DCT breathing motion model with two sets of CT scans to generate pseudo-breath-hold images at inhalation and exhalation and used those images to estimate elasticity, comparing the two elasticity datasets. The purpose of this paper is to evaluate the robustness and consistency of the biomechanical model's lung tissue elasticity estimation.

2.2 Materials and Methods

In this study, 5DCT datasets for 10 lung cancer patients were acquired under IRB approval and with patient consent (IRB# 11-000620-CR-00004). Patient characteristics and history are detailed in Table 2-1. Imaging occurred before treatment on Siemens Definition Flash, Biograph 64, and Definition AS scanners for 5, 3, and 2 patients, respectively. Images were reconstructed with 1 mm slice thickness and a 500 x 500 mm^2 field of view, with subsequent interpolation to 1 x 1 x 1 mm^3 voxels.

2.2.1 5DCT Protocol

A detailed description of the 5DCT protocol is described by Low et al.[76] Figure 2-1 describes the 5DCT image acquisition and motion model generation workflow.[77] The protocol used 25 low-mA repeated free-breathing fast-helical CT (FBFHCT) scan acquisition with a simultaneous abdominal bellows-based breathing surrogate proportional to tidal volume. The

resulting prediction motion model provides motion-sorting-artifact-free images and allows for the generation of images at user-selected breathing phases, like end-inhalation and end-exhalation, while also maintaining accurate Hounsfield units and noise characteristics similar to non-4D CT techniques. These advantages over traditional 4DCT allow for an accurate biomechanical model to be constructed and, as a result, a reliable elasticity estimation. For this work, the scans were subdivided into the first 12 and the last 12 scans with each batch analyzed separately. Between these two sets of image acquisitions, patients remained on the table and there was a brief time pause. 5DCT motion models built from 12 scans were deemed sufficient since Thomas et al. concluded that 10 scans, regardless of breathing trajectories scanned, were required to produce an accurate prediction model.[78]

Patient	Age	Gender	Staging	Smoking History	Pre-Existing Conditions	Prior Thoracic Radiation	Has COPD?
1	85	M	T2a	Former Smoker	Hypertension, coronary artery disease, anemia, BPH, and lung cancer	No prior	No
2	59	F	T2b Nx M1a	Non-Smoker	N/A	No prior	No
3	61	F	N/A	Smoker, 45 pack years	Diverticulitis, kidney stones	No prior	No
4	68	M	T1b N0 M0	Former Smoker, 50 pack years	Intrathoracic lymphadenopathy, diabetes mellitus, hypertension, and coronary artery disease	No prior	No
6	26	F	Stage IV metastatic synovial sarcoma	6 years of tobacco; medical marijuana use	N/A	No prior	No
10	82	F	T1b N0 M0	Former Smoker, 20 pack years	N/A	No prior	No
11	74	M	T1b N0 MX	Former Smoker, 7 pack years	Diabetes mellitus, COPD, bilateral lung nodules, and pulmonary TB	No prior	Yes

15	78	F	Stage IIIA NSCLC (TX N2)	N/A	N/A	IMRT: LUL, 66 Gy	Yes
26	70	M	T1a N0 MX	Current Some Day Smoker, 12.5 pack years	Hypertension, COPD, pulmonary hypertension, pancreatitis, colon cancer, colostomy, depression, congestive heart failure, anemia, high output ileostomy, chronic kidney disease, gouty arthritis, and sleep apnea	No prior	Yes
28	75	M	T1a N0 M0	Never Smoker	Hypertension, GERD (gastroesophageal reflux disease), Parkinson's disease, coronary artery disease, diabetes mellitus, congestive heart failure, incontinence, and hemorrhoids	No prior	No

Table 2-1: Patient characteristics for 10 lung cancer patients included in this study (N/A denotes that the information was not available in patient chart)

Next, for each of the two batches, the 5D motion model was used to characterize tissue motion as a function of breathing amplitude (v) and rate (f). The position X of a piece of lung tissue that was at position $\overrightarrow{X_o}$ at $v = 0$ and $f = 0$ was calculated using Equation 2-1:

$$X = \overrightarrow{X_o} + \vec{\alpha}v + \vec{\beta}f \tag{2-1}$$

where α and β were vector fields that described that tissue's motion. For this work, $v = 0$ was defined as the 5th percentile breathing amplitude and correspondingly labeled exhalation. The equation was used to compute the deformation vector field between exhalation and inhalation, defined here as the 85th percentile of v.

An analysis of patient-specific breathing traces was performed to quantify differences in breathing patterns during the period of image acquisitions used to build the two motion models,

the first 12 and last 12 scans. As these images are the input for the biomechanical modeling and elasticity estimation process, the differences measured in breathing trace at the time of imaging and their influence on the images obtained could influence the ability to gain consistent elasticity estimation.

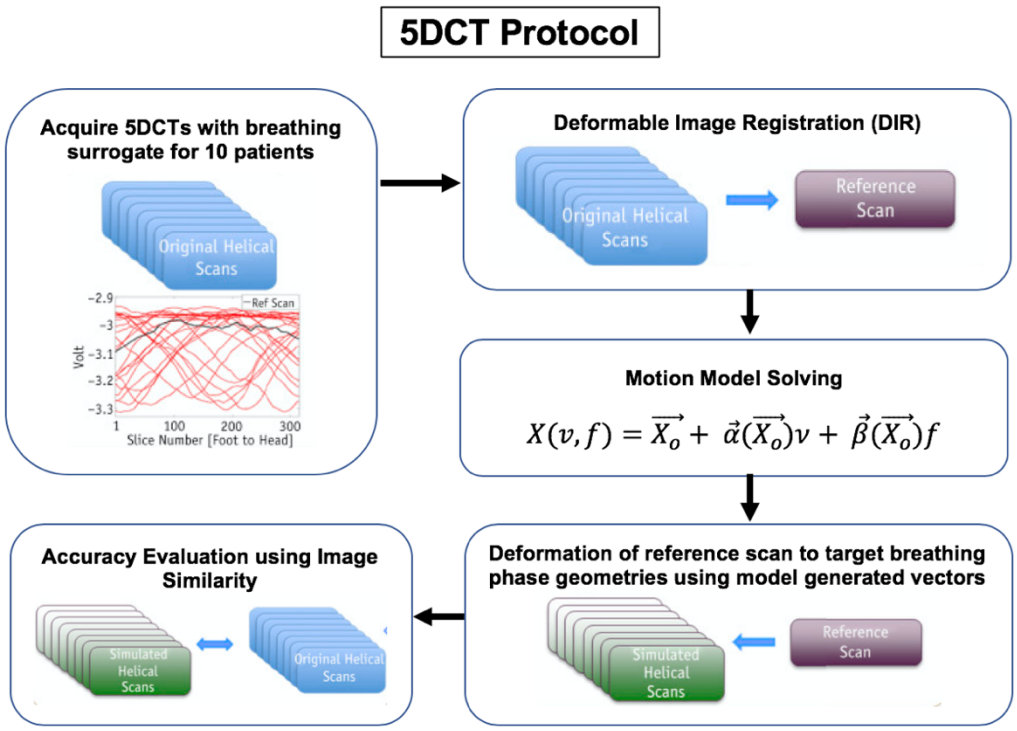

Figure 2-1: 5DCT acquisition and motion model generation workflow[77]

2.2.2 Elastography

A well-validated forward biomechanical model along with the 5DCT-defined exhalation geometry, boundary conditions, and deformation vector fields (DVFs) were used to determine the elasticity by solving the inverse elasticity problem.[79] In an effort to include only parenchymal lung tissue in the elasticity estimation, input CT lung datasets underwent thresholding to remove voxels greater than -350 HU, including large blood vessels and major bronchi.[80] Figure 2-2 details the workflow of the biomechanical model and generation of elasticity and displacement distributions.

The model operated by way of an iterative process of biomechanical property estimation and inverse deformation methods aimed at replicating the provided ground-truth displacements and achieving voxel-level convergence. Each voxel is represented as a finite element with an assigned density-based initial elasticity value and ground-truth displacement value defined by the 5DCT model-derived deformation vectors pointing from end-inhalation to end-exhalation. The deformation vectors of the voxels at the lung boundary (i.e., rib cage and diaphragm) act as boundary conditions for the biomechanical model while the voxels within the lung geometry are free to deform according to linear elastic forces felt due to defined boundary displacements. Elasticity estimations are posed as a parameter optimization problem with the solution being the elasticity distribution that minimizes the difference between model-computed and ground-truth displacements. The optimization process iteratively adjusted elasticity values until $p\epsilon \geq 0.95$, where the maximum iteration limit was set to be 100. The second convergence criteria evaluated the percentage of voxels converged within 10% of the minimum deformation, or $\epsilon_2 = 0.1*\max_a(|d_a|)$. Once these constraints were satisfied, the resultant elasticity was recorded along with the model-achieved displacement vector for each voxel. The convergence and percent accuracy were computed as follows:

$$c_a = \begin{cases} 1: & \| |d_a| - |d_g| \| < \epsilon \\ 0: & otherwise \end{cases} \quad (2-2)$$

$$p_\epsilon = \frac{\sum_1^n c_a}{n} \quad (2-3)$$

In Equation 2-2, c_a represents the model error and is calculated for each voxel through the comparison of L2-norm (ϵ) and the difference between resultant model-achieved displacement (d_a) and ground-truth DVF (d_g). In Equation 2-3, the percent accuracy (p_ϵ) is defined as the sum of the error (c_a) divided by the total number of voxels *n*.

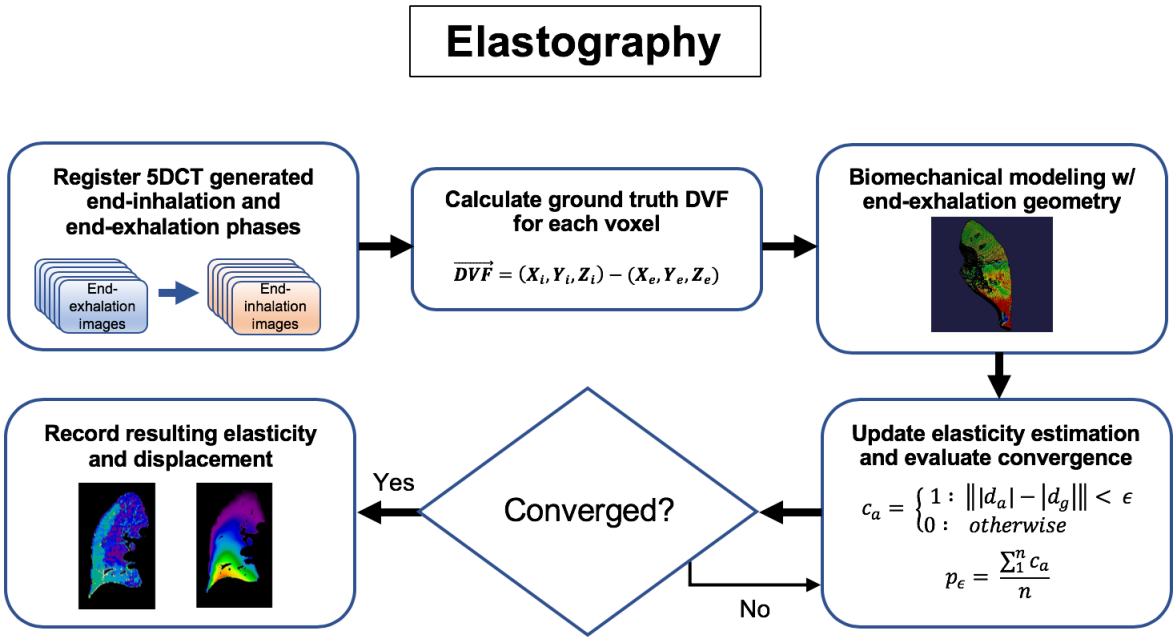

Figure 2-2: Elastography workflow

2.2.3 Consistency Analysis

The elasticity estimations were performed for each of the 5DCT models generated as previously explained in Section 2.2. The inverse DVFs, which pointed from end-exhalation to reference geometry, defined as the geometry of the first 5D scan used as a reference for both 5DCT models, were used to warp the resulting distributions to a common geometry for voxel-level evaluations. This was performed by the following equations:

$$(x', y', z') = (x + U, y + V, z + W) \qquad (2-4)$$

Equation 2-4 describes the voxel-specific application of 3D-deformation vectors (i.e., U, V, and W) to the end-exhalation voxel position (x,y,z) to establish the voxel's new location (x',y',z') in the reference geometry after warping.

The metrics used in the quantitative analysis of differences in resultant elasticity and displacement values among 5DCT models were: Let E_i^1 and E_i^2 represent the elasticities of a given reference voxel position i. Let c_i^e represent a given reference voxel's criteria passing decision. Let d_i^1 and d_i^2 represent the displacements computed from the biomechanical model using the elasticities E_i^1 and E_i^2, respectively. Let c_i^d represent a given reference voxel's criteria passing decision.

$$\overline{\Delta E} = \frac{\sum_{i=1}^{n} \left| E_i^1 - E_i^2 \right|}{n} \tag{2-5}$$

$$p_e = \frac{\sum_{i=1}^{n} c_i^e}{n} \quad where \quad c_i^e = \begin{cases} 1: & \left\| E_i^1 - E_i^2 \right\| < 2\ kPa \\ 0: & otherwise \end{cases} \tag{2-6}$$

$$\overline{\Delta d} = \frac{\sum_{i=1}^{n} \left| d_i^1 - d_i^2 \right|}{n} \tag{2-7}$$

$$p_d = \frac{\sum_{i=1}^{n} c_i^d}{n} \quad where \quad c_i^d = \begin{cases} 1: & \left\| d_i^1 - d_i^2 \right\| < 2\ mm \\ 0: & otherwise \end{cases} \tag{2-8}$$

The average difference in lung elasticity, $\overline{\Delta E}$, was calculated in Equation 2-5 as the sum of voxel elasticity differences between models over the total number of voxels. In Equation 2-6, p_e describes the percentage of total lung voxels with an elasticity value difference less than 2 kPa between models. Similarly, average voxel displacement, $\overline{\Delta d}$, was calculated in Equation 2-7, as the sum of all voxel displacement differences between models over total voxels. In Equation 2-8, p_d, describes the percentage of total lung voxels with a displacement value difference of less than 2 mm between models. In addition to quantitative analysis, colormaps were generated for a qualitative comparison and are further discussed in the results section.

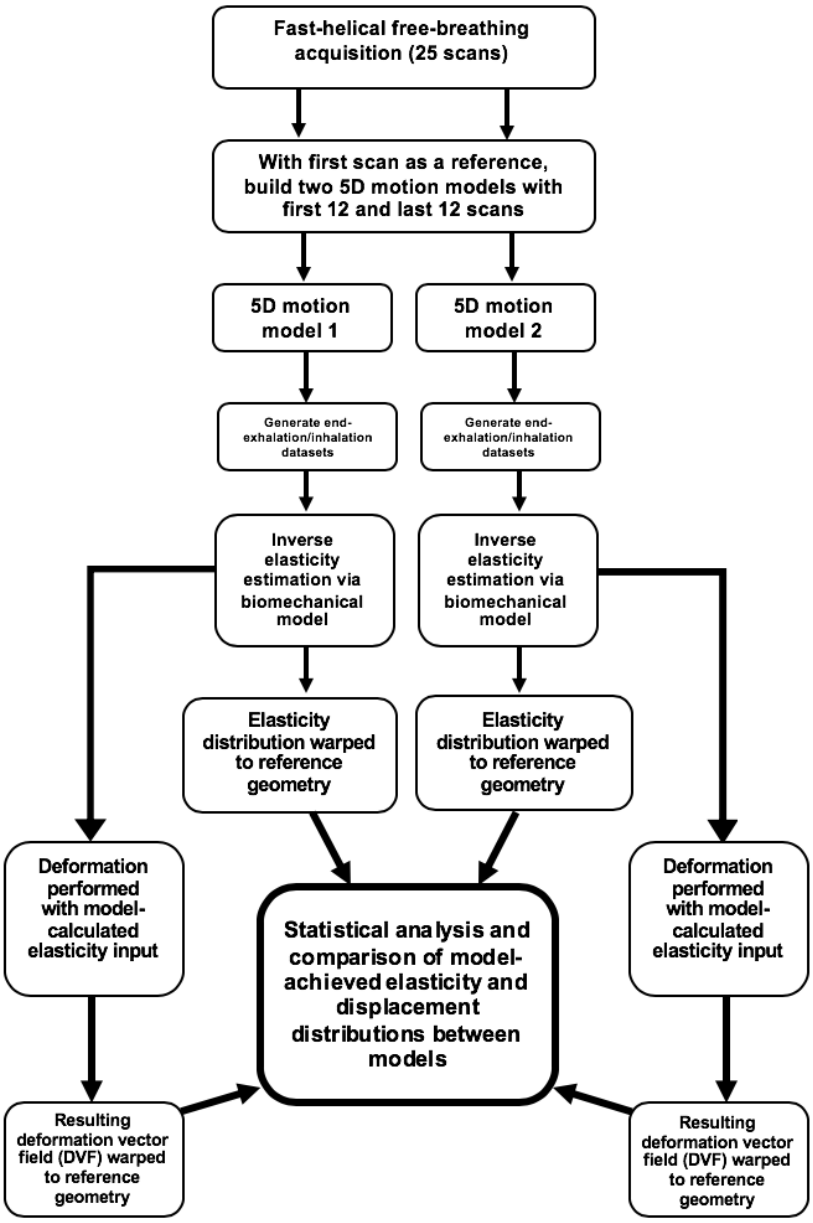

Figure 2-3: Study methodology

2.3 Results

Figure 2-4 provides an example of the distinct time intervals, identified by dashed and bolded portions of the breathing trace, over which two sets of 12 free-breathing CT scans were acquired to construct the two independent 5DCT motion models. For all patients, a comparison

of breathing traces associated with the two 5DCT datasets showed a mean percent difference of 8.9% and a correlation analysis resulted in an average correlation coefficient of 0.22. Figure 2-5 compares breathing trajectories for the 5DCT acquisitions of Patient 3 (Figure 2-5a) and Patient 6 (Figure 2-5b). From a qualitative standpoint, the breathing traces are noticeably different in frequency, amplitude, and homogeneity over time as noted for patient 3 (Figure 2-5a) during the initial time interval of 0 to 3000 ms. For quantitative measurement, a comparison of breathing traces showed mean percent differences in breathing traces of 20.7% and 18.7% for patients 3 and 6, respectively. Correlation analysis of each patient's two model-associated breathing traces found the lowest recorded correlation coefficients were 0.02 and 0.05. The results of these analyses showed the level of significant breathing variations observed, both qualitatively and quantitatively, over the time in which the scans were acquired.

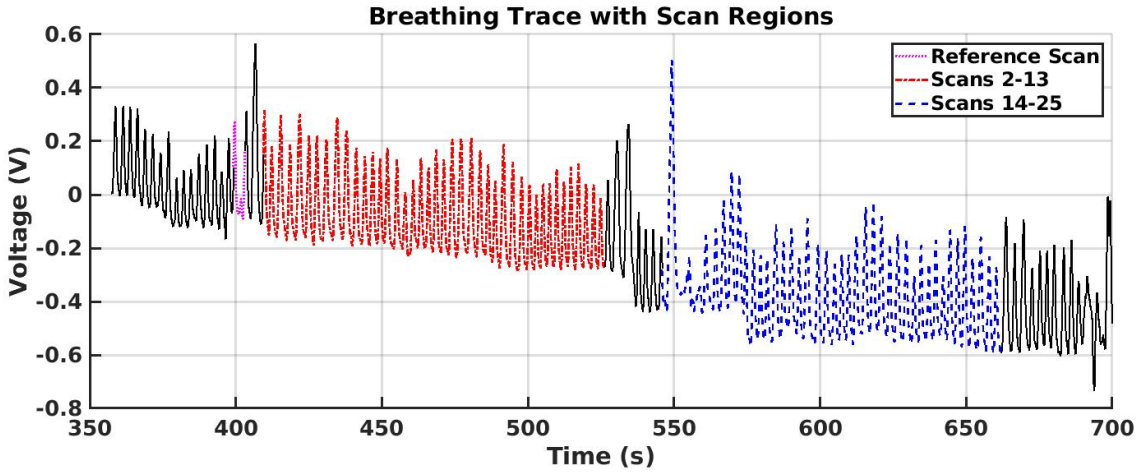

Figure 2-4: Breathing trace with differentiated scan acquisition time intervals for 5DCT models

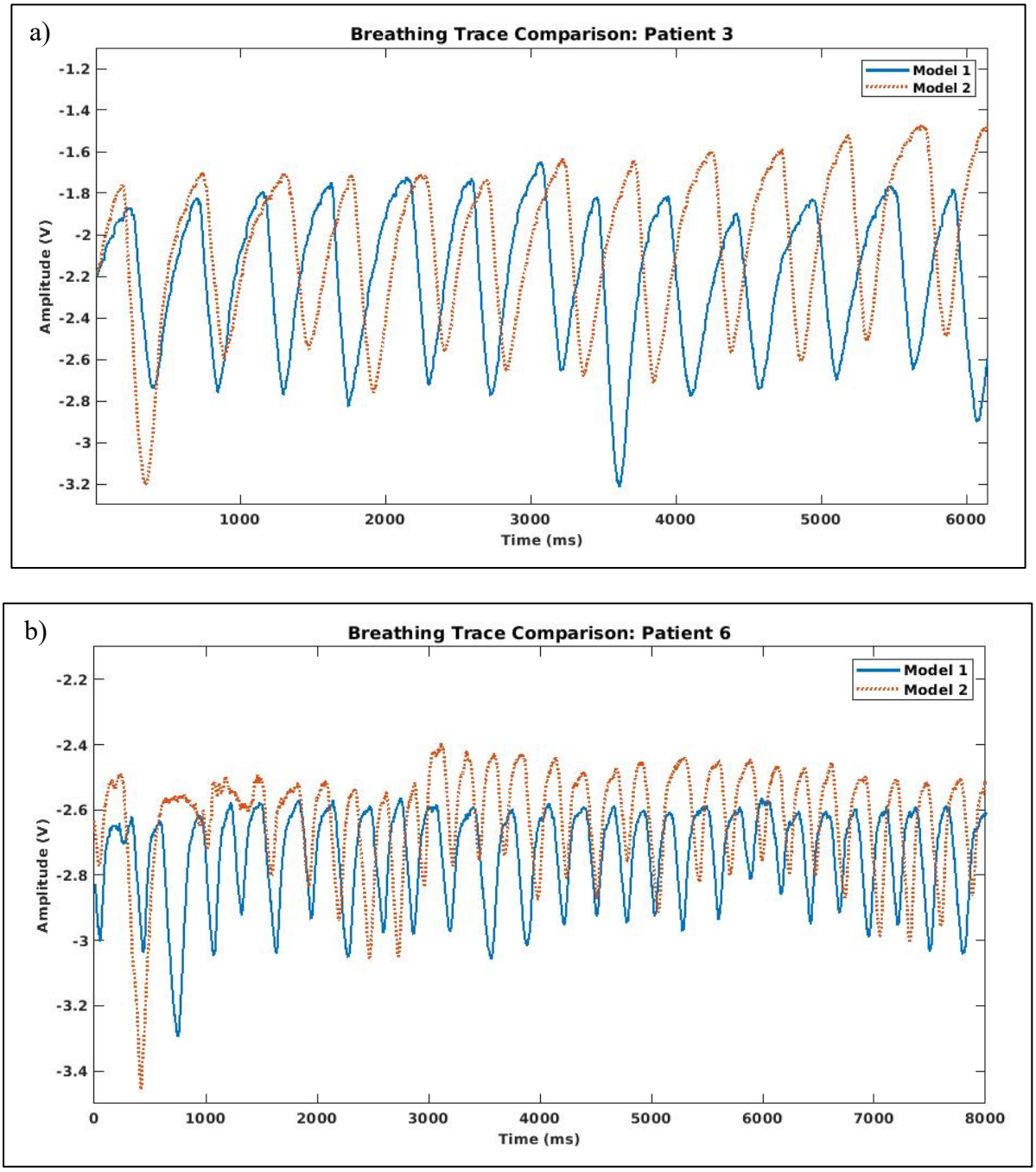

Figure 2-5: Comparison of breathing traces during 5DCT acquisition for each model for (a) patient 3 and (b) patient 6

The biomechanical model estimated elasticity distributions for both 5DCT datasets associated with each patient. Figure 2-6 shows a 2D slice of elasticity estimation results for coronal

slices of the right and left lungs for a single patient using the biomechanical model and the 5DCT datasets. Figures 2-6a and 2-6b and Figures 2-6c and 2-6d present the elasticity associated with a left and right lung slice, respectively, for the initial and repeat 5DCT. It can be seen from these images that the heterogeneous elasticity distributions for each of the cases appear to be regionally similar to their associated repeat 5DCT. A consistent trend, observed amongst the entire cohort of patients, was the upper medial side of both the right and left lungs had a distribution of elasticity values ranging from 0-5 kPa. Similarly, the lower lateral region of each lung displayed consistent distributions in the elasticity range from 5-10 kPa. Specific elasticity values of voxels belonging to structures such as small blood vessels (5 to 7.5 KPa) and regions of air trapping (0 to 2.5 KPa) also matched well. Certain voxels at the boundary of the lung, where motion was dictated by ground-truth DVF, and of rigid vessels took on elasticity values greater than those of the surrounding parenchymal tissue, in the range of 10-20+ kPa due to their immobility, as dictated by the boundary conditions.[81] Qualitative colormaps showed a high level of consistency in regional elasticity distribution trends among the 5DCT datasets.

Figure 2-7 shows the voxel elasticity value differences between datasets for each patient. The largest measured median value, denoted by the midline of the boxes, was a 0.11 kPa difference with the average of these medians being 0.02 kPa. The 25^{th} and 75^{th} percentile values are marked by the top and bottom boundaries of the boxes, respectively. The 25^{th} and 75^{th} percentile had mean values of -0.76 kPa and 0.71 kPa, respectively, and were greater than +/- 1 kPa only for patients 3, 6, and 9. Finally, the whiskers represent the minimum and maximum values, within +/- 2.7σ, with mean values of 2.91 kPa and -2.97 kPa, respectively. A boxplot representation and quantitative analysis of voxel elasticity value differences display the agreement of distributions at the voxel level.

Measures of elasticity differences between the two estimations for the 10 patient datasets are tabulated in Table 2-2. The mean elasticity value difference between models for voxels of less than 5 kPa, an elasticity range used as a biomarker for COPD staging, was 0.60 kPa and the percentage of voxels differing by less than 2 kPa was 92.0%.[75] For all lung voxels, the mean difference was found to be 1.69 kPa, with 74.1% of voxels differing by less than 2 kPa between datasets. When considering all voxels classified as parenchymal tissue, defined by voxels with CT numbers between -600 and -900 HU, the average difference was 0.82 kPa and the percentage of voxels differing by less than 2 kPa was 86.7%. The mean correlation coefficient for all patient elasticity distribution model pairs was 0.81. Clinically agreeable elasticity value differences for voxels within the elasticity range of interest point to collectively consistent distributions across all patients.

The differences in biomechanical model-achieved versus ground truth displacements were analyzed at the voxel level, as described in Table 2-3. The average displacement difference for all lung voxels was 0.82 mm with 90.4% of voxels differing by less than 2 mm. Similarly, for parenchymal lung voxels with elasticity less than 8 kPa, the average difference in displacement was 0.62 mm and the percentage of voxels that differed by less than 2 mm was 94.6%. For voxels with elasticity less than 5 kPa, the average difference in voxel displacement was 0.49 mm and the percentage of voxels that differed by less than 2 mm was 96.6%. The mean correlation coefficient between model-achieved displacement distributions for all patients was 0.845. This supports the idea that the biomechanical models exhibit a consistent behavior across patients when comparing data acquired at different time points in a single session. Quantitative measures of differences in biomechanical model-achieved displacement values between 5DCT datasets show a strong agreement in model performance.

Figure 2-8 shows the elasticity distribution for a single patient within the elasticity range of lung parenchyma (1-8 kPa). The differences are small and the elasticity accuracy between the two estimations is consistent for the parenchymal elasticity range. The average percent difference in voxel count across bins 1-8 kPa was 3.8% for this patient. For all 10 patients, the average percent difference across bins was 7.1%, indicating a high consistency of elasticity distribution outputs.

Figure 2-9 shows displacement map differences of lung slices generated using the biomechanical model. Figures 2-9a and 2-9b show a comparison of displacement maps of the left lung, while Figure 2-9c and 2-9d show an example of the right. With only minor variations observed between displacement maps and boundary conditions, the qualitative evaluation shows high correlation between displacement distributions. The range of voxel displacement in the superior half of the lung 0-7.5 mm is consistent across both lungs for both models. Similarly, a consistent range of 7.5-16 mm was measured in the inferior half of the lung. Qualitative representations of the displacement distributions show largely consistent regional trends between the displacement outputs of 5DCT datasets.

Figure 2-10 shows the model-achieved voxel displacement value differences between 5DCT datasets for each patient. Calculated median differences for each patient, denoted by the box midline, were smaller than 0.60 mm and the average median was found to be 0.14 mm. The top and bottom boundaries of the boxes represent the 25^{th} and 75^{th} percentile values, respectively. These percentile values were greater than +/- 1 mm only for patients 6 and 9 with mean values of -0.35 mm and 0.63 mm for the 25^{th} and 75^{th} percentiles, respectively. The whisker extensions show the minimum and maximum values within +/- 2.7σ, with mean values across all patients of -1.82 mm and 2.10 mm, respectively. A box plot and reported quantitative measurements of voxel displacement values show clinically agreeable differences. Consistency in model performance is

established through relatively small voxel-to-voxel differences between model-achieved displacement values for each 5DCT dataset.

Bland-Altman plots describing the elasticity and model-achieved displacement difference distributions results are shown in Figure 2-11. Elasticity difference distributions for left and right lungs are described in Figures 2-11a and 2-11b. The plots include a line denoting the mean of the differences in elasticity (in kPa), as well as lines above and below marking +/- 1.96σ from the mean. For left and right lungs, the mean differences were 0.17 kPa and -0.15 kPa, respectively. It can be seen from the displayed value density that all regions comprising > 3% of the voxels were within a 1 kPa difference for both lungs. Similarly, Figures 2-11c and 2-11d show Bland-Altman plots for displacement difference distributions with means of 0.08 mm and 0.16 mm for left and right lungs, respectively. The analysis of value density showed that regions comprising > 5% of the voxels were within a 1 mm difference. These results give further evidence that both the elasticity and displacement results were consistent across 5DCT datasets.

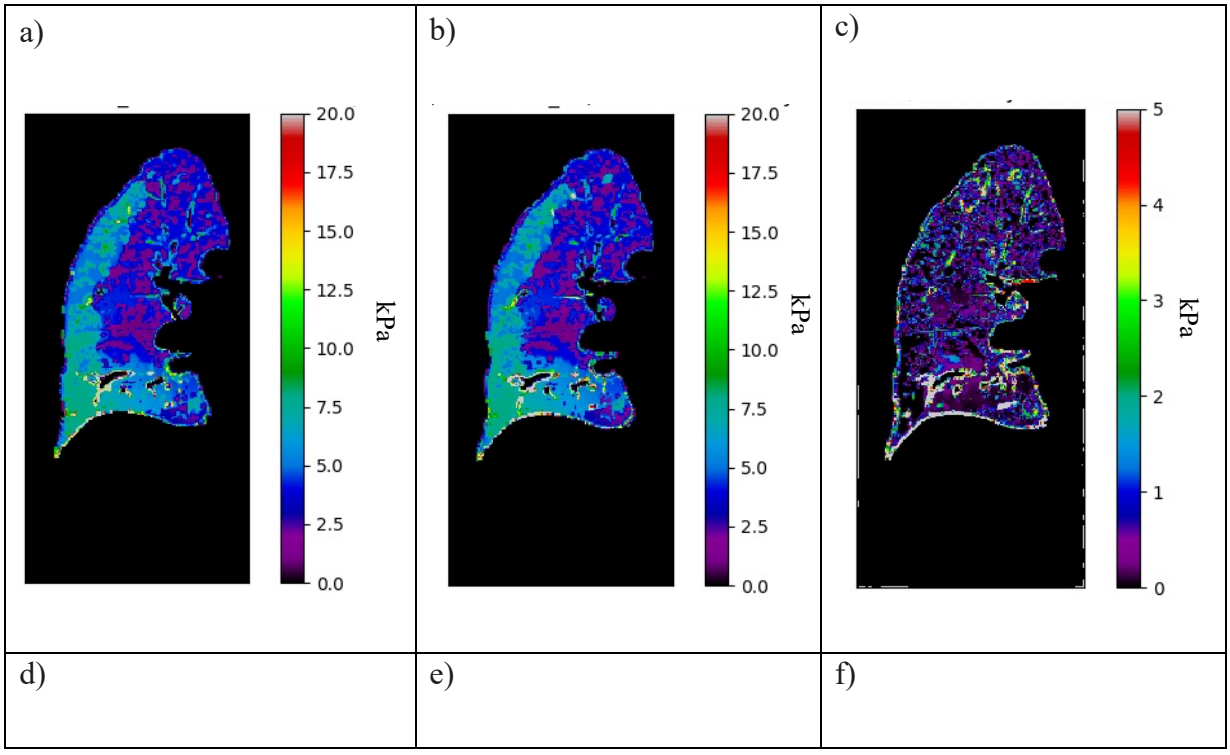

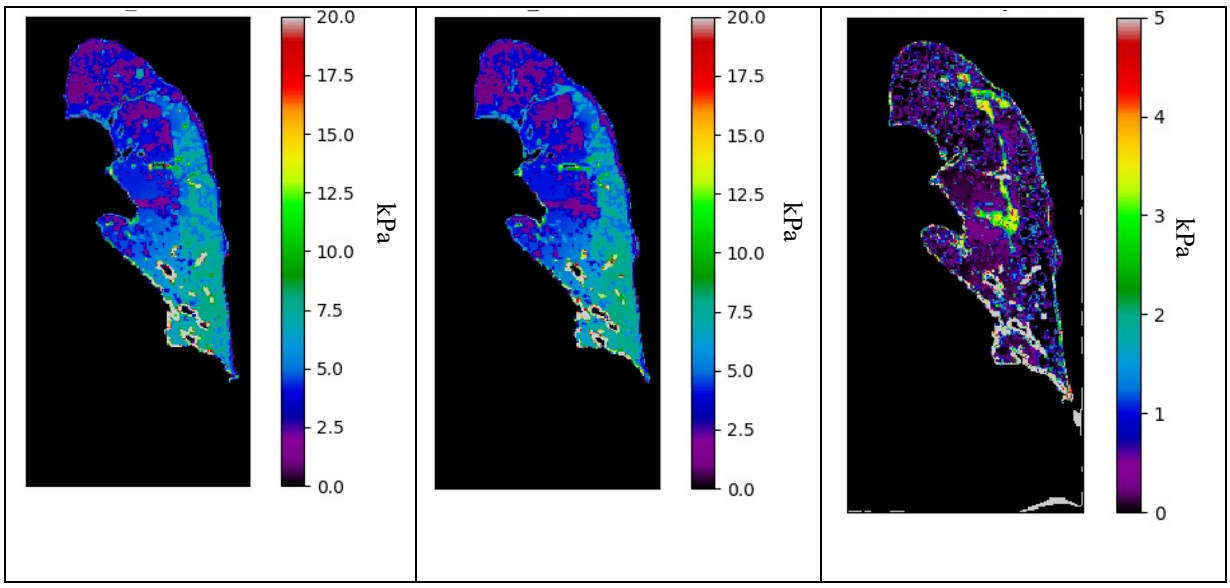

Figure 2-6: Elasticity estimated from the two 5DCT datasets for Patient 1 where (a) and (d) show elasticity distribution for a right lung slice, (b) and (e) show elasticity distribution for a left lung slice, and (c) and (f) show the difference between model distributions

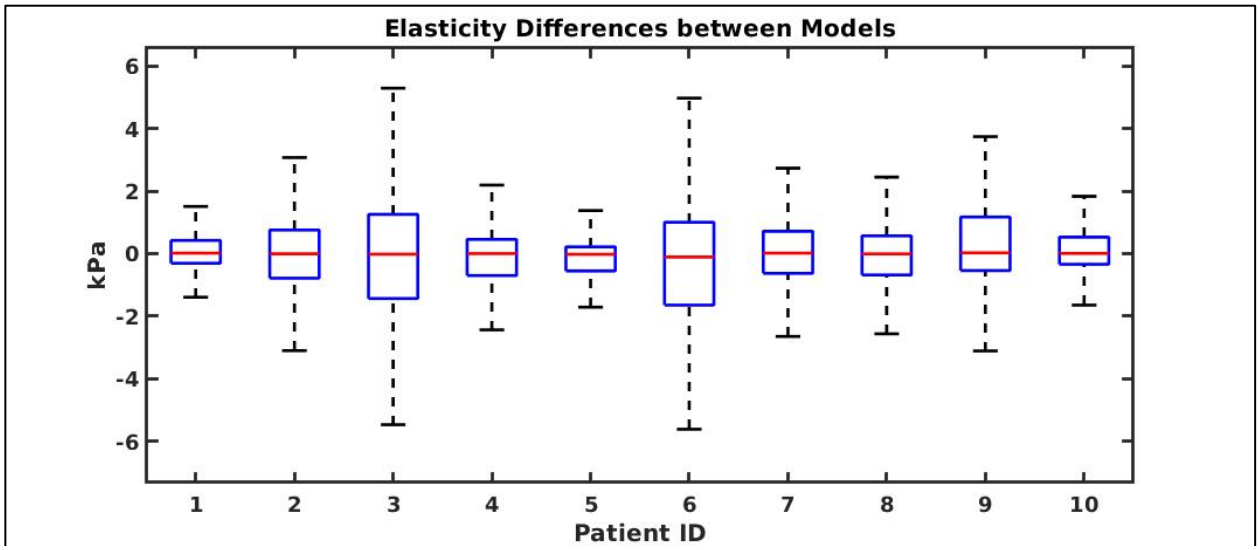

Figure 2-7: Distribution of voxel elasticity differences between models for each patient

Elasticity Difference for lung parenchymal voxels				
Patient ID	Percent voxels < 1 kPa Difference	Percent voxels < 2 kPa Difference	Average Difference (kPa)	Correlation Coefficient
1	86.05%	99.5%	0.454	0.898
2	84.06%	94.80%	0.480	0.799
3	60.51%	80.86%	0.990	0.732
4	77.03%	92.32%	0.608	0.846
5	95.37%	98.4%	0.207	0.811
6	66.01%	86.72%	0.882	0.750
7	78.55%	93.56%	0.619	0.774
8	80.53%	94.35%	0.558	0.885
9	68.51%	86.82%	0.842	0.759
10	87.90%	96.87%	0.390	0.841
Mean:	78.48%	92.03%	0.603	0.810

Table 2-2: Percentage of voxels < 1 kPa difference, < 2 kPa difference between 5DCT models, average voxel elasticity difference for voxels of < 5 kPa, and correlation coefficients

Displacement Difference for lung parenchymal voxels				
Patient ID	Percent voxels < 1 mm Difference	Percent voxels < 2 mm Difference	Average Difference (mm)	Correlation Coefficients
1	96.13%	99.93%	0.311	0.912
2	78.40%	94.49%	0.679	0.781
3	76.81%	96.98%	0.68	0.824
4	98.94%	99.45%	0.122	0.942
5	90.08%	98.88%	0.504	0.727
6	61.0%	83.52%	1.028	0.822
7	95.43%	99.41%	0.358	0.885
8	74.36%	96.43%	0.707	0.958
9	56.72%	79.19%	1.213	0.864
10	91.60%	98.19%	0.399	0.739
Mean:	81.94%	94.65%	0.60	0.845

Table 2-3: Percent voxels < 1 mm difference, < 2 mm difference between 5DCT models, average voxel displacement difference for voxels of < 5 kPa, and correlation coefficients

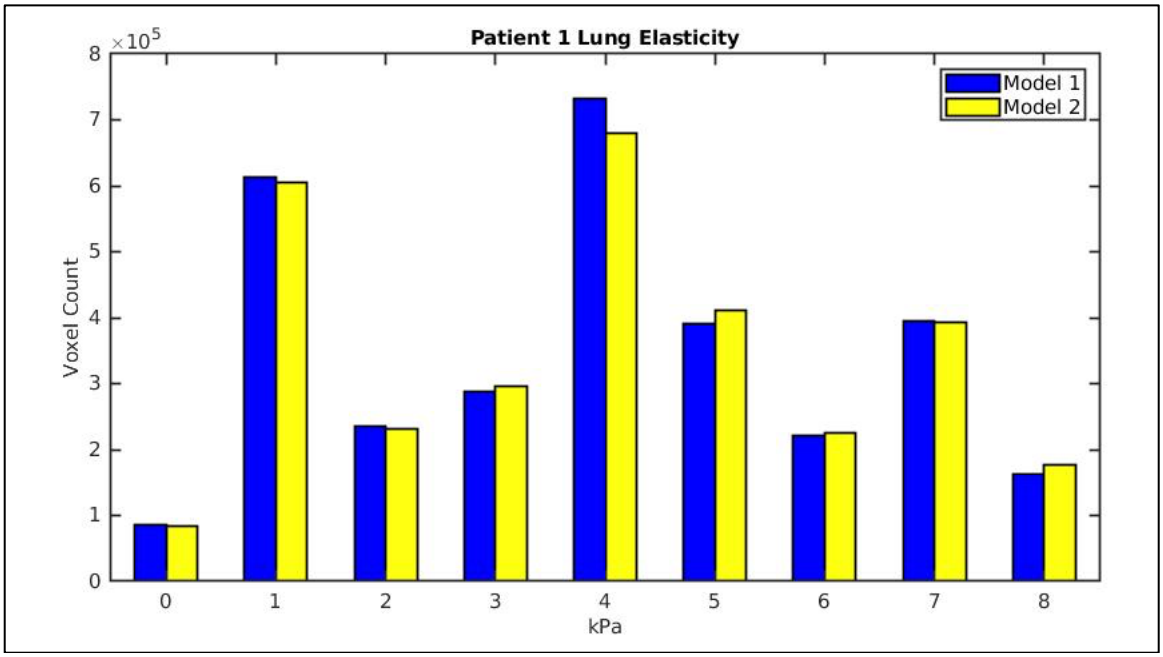

Figure 2-8: Histogram of the elasticity distribution obtained from the two 5DCTs for Patient 1

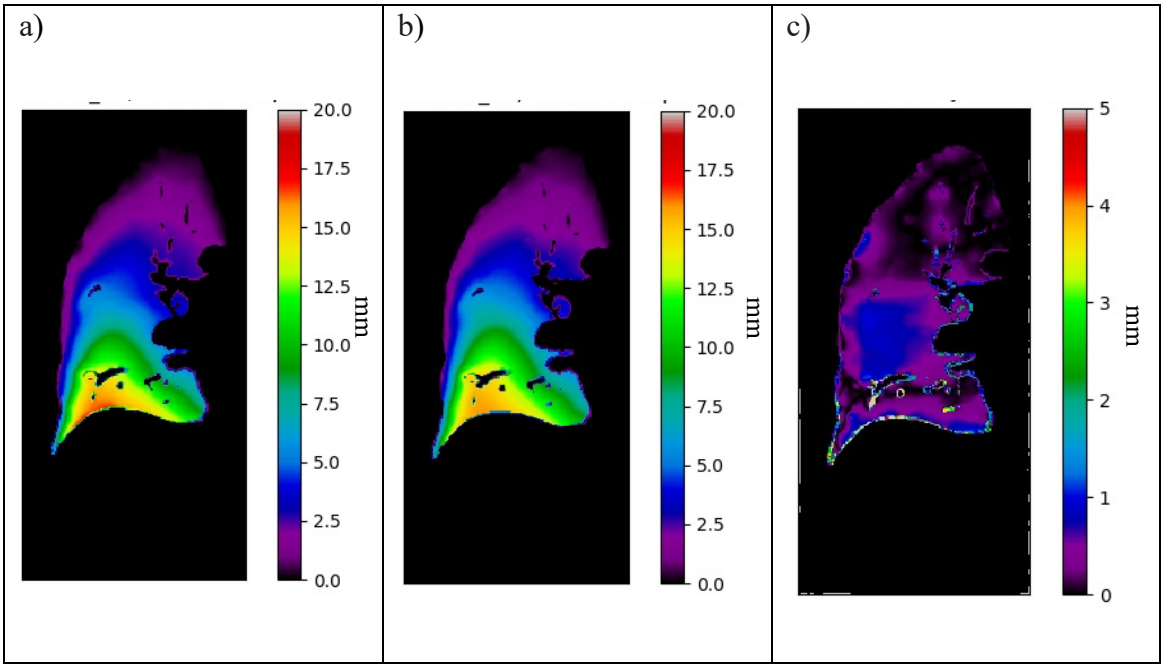

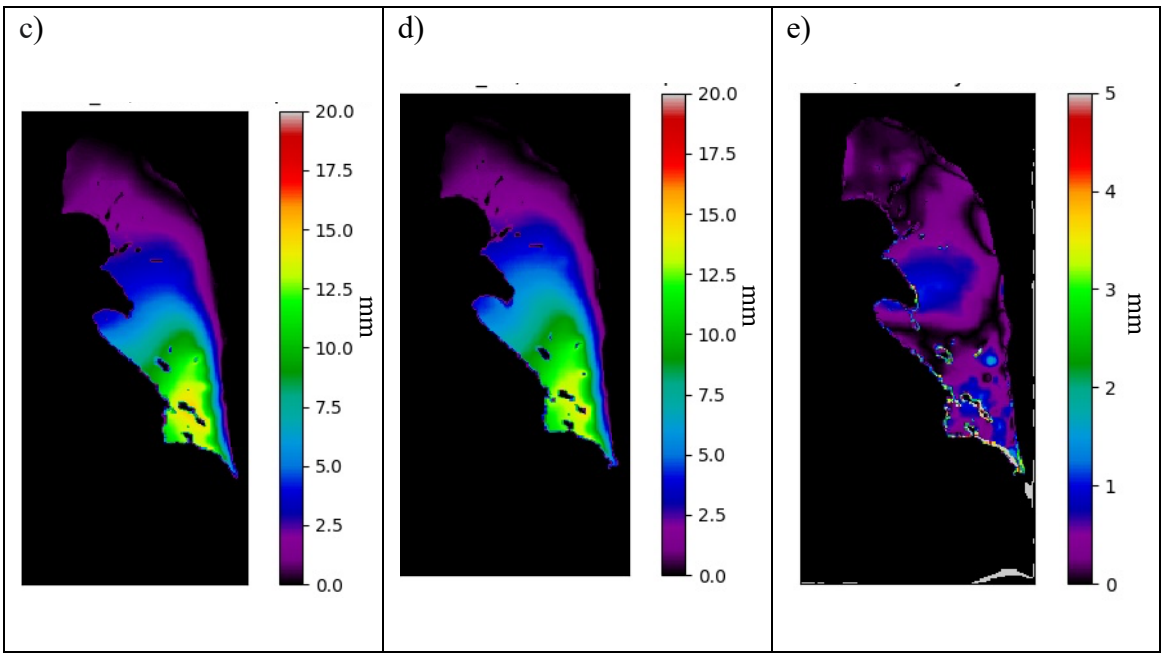

Figure 2-9: Displacement estimated from the two 5DCT datasets for Patient 1 where (a) and (c) show the displacement map for a right lung slice, (b) and (d) show the displacement map for a left lung slice, and (c) and (e) shows the difference between model distributions

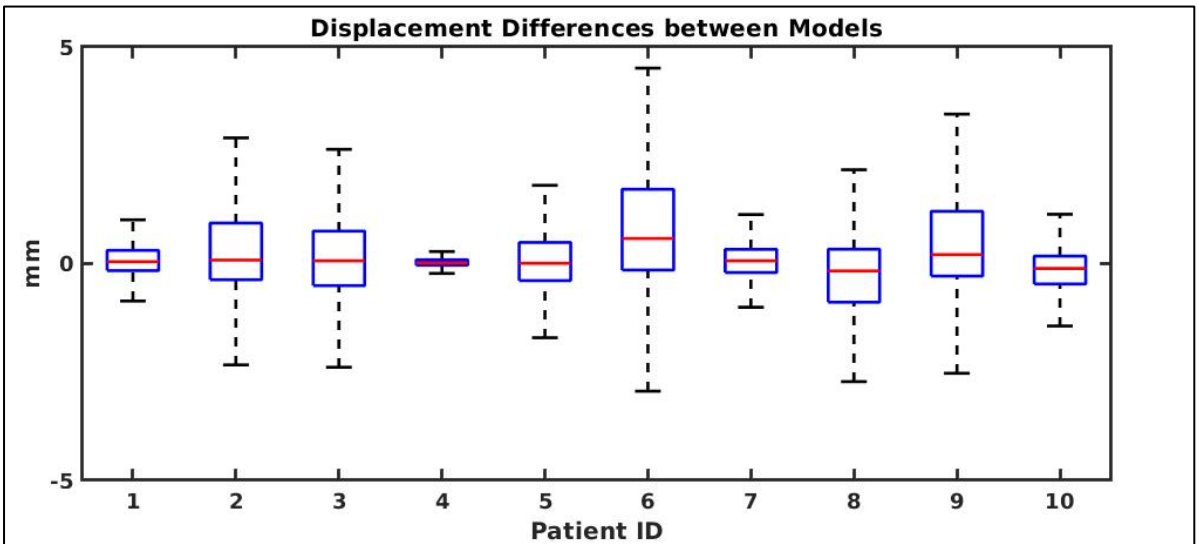

Figure 2-10: Distribution of voxel displacement differences between models for each patient

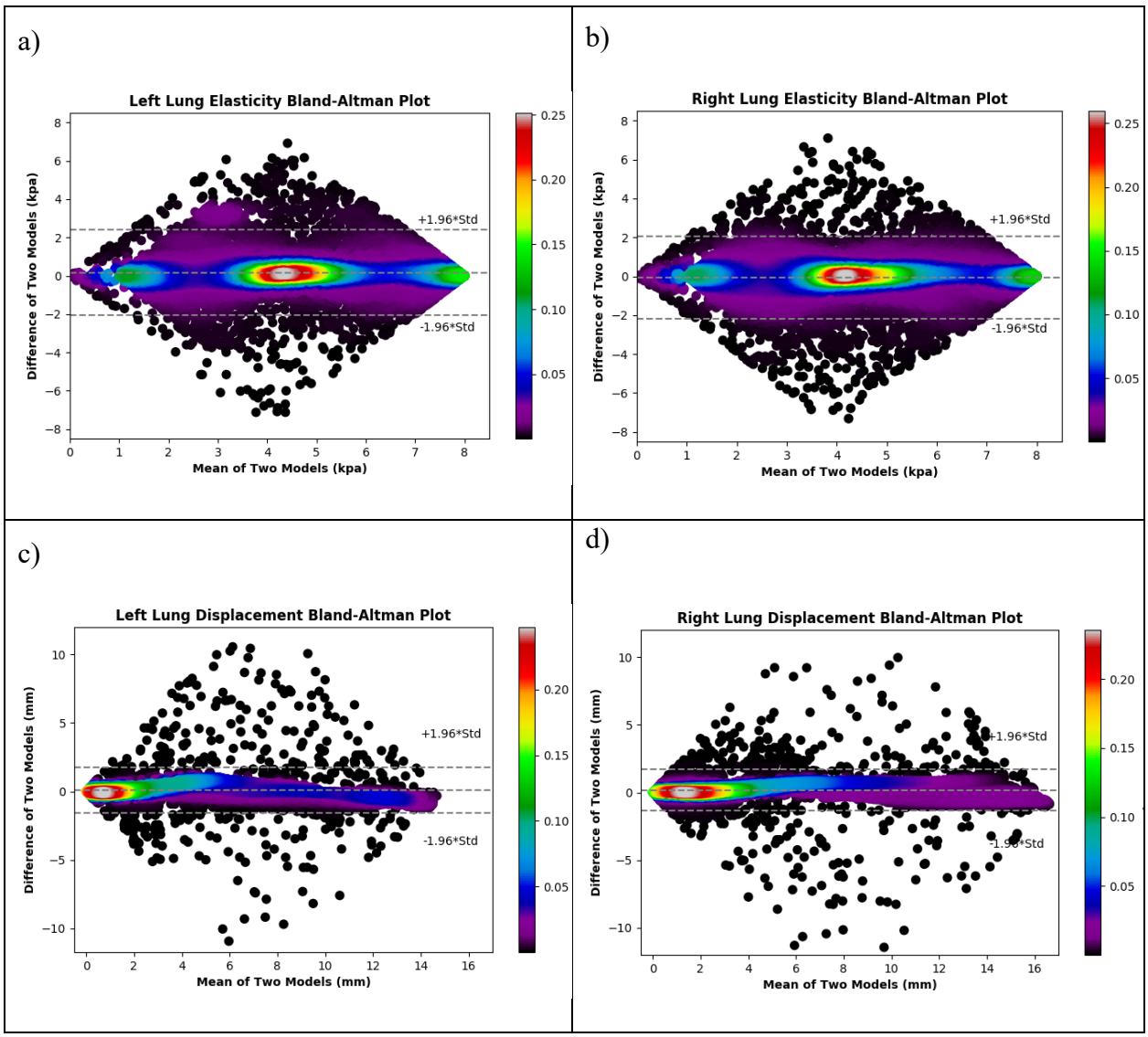

Figure 2-11: Bland-Altman plots of elasticity and displacement distributions for (a and c) left lung (b and d) right lung, respectively

2.4 Discussion

In this study, only the displacement of lung tissue was considered and variations in motion of static boundaries such as ribcage and diaphragm were not accounted for directly. Taking this additional source of motion into account in future work could further quantify the consistency of biomechanical model performance for scenarios when the 5DCT images are collected over

significant time intervals. This further test of consistency in circumstances of more physiologically extreme breathing motion differences could be conducted given there is adequate accessible clinical data.

In a related work, Du et al. investigated the reproducibility of lung expansion measurements by performing two repeat 4DCTs of free-breathing humans and calculating the associated Jacobian.[82] This study found the reproducibility of the Jacobian to be largely reliant on the reproducibility of patient respiration and breathing pattern. In comparison, our study found a similar trend in which reported that consistency measures were lower for those patients showing the largest differences in breathing pattern sections. However, all patients included in our study had less than a 1 kPa and 1 mm mean difference in elasticity distribution and model-achieved displacement distribution, respectively.

Future work would also focus on making hyper-elastic measurements that can take deep inhalation and exhalation patterns into account for elasticity estimation. Recent studies have shown that modeling the lungs as an inhomogeneous material with hyperelastic behavior led to an improved prediction of the lung tissue motion.[83] This consideration could lead to a more physiologically accurate characterization of elasticity distribution in the presence of hyperelastic behavior in lung tissue.

The current biomechanical modeling approach does not consider airflow dynamics. An investigation is underway to further improve the accuracy of the biomechanical model through an accurate representation of airflow and pressure distributions within the lungs. Due to obstructed airflow and narrowed airways observed in patients with lung diseases such as COPD, airflow dynamics can play a significant role in informing a biomechanical modeling approach. The incorporation of such dynamics will serve to supplement and validate elasticity estimations as an

indicator of lung function. This approach also does not incorporate motion due to blood flow dynamics and cardiac motion. While previous studies by White et al show the impact of blood flow on lung deformations using 4DMR-based imaging, we don't expect significant blood flow changes between the two imaging sessions.[84]

2.5 Conclusions

This research has demonstrated the feasibility of using finite element biomechanical lung models to estimate lung elasticity with consistency in patient lung dynamics. This was accomplished through the integration of the 5DCT imaging protocol and subsequent creation of two 5D motion models to obtain images at any point in a patient's breathing trajectory. Taking the resultant DVFs and boundary conditions as ground truth, elastography was performed by an iterative forward model to obtain model-achieved elasticity and displacement distributions for each 5DCT dataset. We show that when patient breathing variations are taken into consideration, the consistency of a previously well-validated elastography method is observed in both the qualitative results and quantitative measures. The results of this study further validate the ability to estimate lung elasticity consistently and accurately with a biomechanical model for COPD disease staging.

CHAPTER 3: An adversarial machine learning framework and biomechanical model-guided approach for computing 3D lung tissue elasticity from end-expiration 3DCT

A version of this chapter has been published as a manuscript: Med Phys, Vol. 48, No. 2, 2021. doi: 10.1002/mp.14252

3.1 Introduction

Radiation therapy is a clinical procedure that is commonly used to treat lung cancer.[85,86] With an increasing focus on hypo-fractionated radiotherapy and improved patient quality of life following treatment, there is a greater need to spare the normal lung regions while precisely targeting the lung tumor.[87,88] This requires an ability to precisely differentiate regions of the lung tissue as either functional or diseased. Lung tissue elasticity is a biomechanical metric associated with each lung voxel that can characterize tissue functionality.[89] Spatial variation in the lung tissue elasticity is illustrative of differences in the local tissue compliance. In-vivo measurement of these parameters will enable a clearer understanding of patient-specific lung pathophysiology and lead to the development of treatment plans that optimally spare normal tissue while also delivering greater tumor doses.[90,91]

The ability to estimate lung tissue elasticity has been demonstrated using magnetic resonance elastography (MRE).[59-61] This approach is limited within a conventional radiotherapy setup due to the availability of this imaging modality. Therefore, there is a need to establish elastography methods using imaging modalities already acquired as part of the clinical radiotherapy workflow, such as computed tomography (CT) imaging.[64] Recently, the possibility of estimating the lung tissue elasticity from four-dimensional CT (4DCT) datasets was documented in Hasse et al.[54] This work proposed a methodology to estimate lung tissue elasticity, as Young's modulus (YM), using three-dimensional (3D) deformation vector field (DVF) information computed from DIR of 4DCT lung images. However, the approach is highly

computationally expensive, which limits the feasibility of clinical implementation and use on a large number of datasets.

In this paper, we formulate a machine learning (ML) mechanism to learn elasticity distribution using the subject-specific lung end-expiration CT geometry. The learning process consisted of a supervised approach, in which a deep neural network (DNN) was trained on known lung geometry (lung boundary and internal substructures) and elasticity information. The elasticity for the training process was estimated using a biomechanically guided inverse estimation procedure using 4DCT as the image data.[50] Once trained, the neural network model can infer patient lung tissue elasticity distribution given a single end-exhalation CT lung image dataset. From a clinical perspective, the proposed approach is applicable for radiotherapy as no additional imaging modality is required for the lung elastography process. The expanded availability of lung tissue elasticity opens new avenues of research in the assessment of lung function and may also be extended in applications such as interventional lung treatment. Finally, the computational time reduction provided by the proposed deep learning approach enables near real-time estimation of patient lung dynamics.

3.2 Materials and Methods

In this section, we first present the biomechanical model used for the lung tissue elasticity estimation. We then discuss the inverse optimization process during the elasticity estimation process, used to generate training data. Then, we describe the cGAN used for the machine learning process. Finally, we detail the steps involved in the machine learning of the lung tissue elasticity for a given end-exhalation CT.

3.2.1 Biomechanical model

The biomechanical model presented here is tasked with computing the lung tissue deformation for a given lung boundary displacement and associated elasticity distribution.[54,92-94] The deformation space was defined as a virtual three-dimensional space, where the model geometry was initialized and deformed. The lung model geometry, which consisted of the lung boundary conditions and substructures inside the lung, was represented by finite mass element nodes corresponding to the center of each voxel of anatomy in the CT image. The high-resolution biomechanical lung model was assembled from a segmented lung CT end-expiration geometry using the steps previously discussed in Neylon et al., with the resulting mesh density being representative of the input CT. In this work, each finite element was considered a mass element. Mass elements were connected to neighboring elements by linear elastic connections in the deformation space to form a regular polygonal volumetric mesh with the same resolution as that of the CT image (~1 mm^3) to ensure a physically realistic deformation. The distance between two connected element centers, termed the rest length, and orientation of each connection were then recorded and assigned an elasticity value and a Poisson's ratio as the final step in model initialization. As patients are expected to breathe normally during a 4D imaging session, a locally heterogeneous distribution of linear elastic material properties (Poisson's ratio = 0.43) was used for this study.[95-97]

For deforming the modeled lung geometry, we employed a biomechanical constitutive equation (Hooke's law), with the tissue elasticity represented by the YM. From a biomechanical standpoint, the lung deformation occurs due to the internal corrective forces compensating for the lung boundary displacement obtained from the five-dimensional CT (5DCT) data. As previously discussed in Hasse et al., no external forces were applied for this purpose.[50,66] The biomechanical lung model was actuated using the lung surface element displacements as pointwise and fixed

boundary constraints. For the given boundary displacements, the corrective forces on each mass element were calculated as the summation of tensile, shear, and dashpot damping forces. Initially, the elastic internal corrective forces were set to zero at rest. During induced model deformation, the mass elements were relocated to new positions inside the deformation space, causing the internal corrective forces to take on non-zero values. For each finite element, a, the elastic force, $\vec{f}_{E,ab}$, shear force, $\vec{f}_{S,ab}$, and the dashpot damping force, $\vec{f}_{v,ab}$, were calculated for each connected element, b, and summed to find the total internal corrective force, $\vec{f}_a$, according to Equation 3-1:

$$\vec{\mathbf{f}}_{\mathbf{a}} = \sum_{\mathbf{b}} \left(\vec{\mathbf{f}}_{\mathbf{E,ab}} + \vec{\mathbf{f}}_{\mathbf{S,ab}} + \vec{\mathbf{f}}_{\mathbf{v,ab}} \right), \tag{3-1}$$

where the elastic force acting between two mass elements is described by:

$$\vec{\mathbf{f}}_{\mathbf{E,ab}} = \sum_{\mathbf{b}} \left(\mathbf{E_{ab}} \times \left(\frac{|P_{ab}| - |l_{ab}|}{|l_{ab}|} \right) \frac{P_{ab}}{|P_{ab}|} \right) \tag{3-2}$$

in which the term E_{ab} refers to the elasticity between node elements a and b, l_{ab} is the rest length orientation, and P_{ab} is the projection vector. The shear force was computed as the force along the rejection vector, computed as a difference between the deformed vector between the elements and the projection vector. Finally, the dashpot damping force was computed from the velocities of the neighboring mass elements and the Poisson ratio.[52]

As the material elasticity is assumed to be linear, Equation 3-2 is derived from the relationship between elasticity and the magnitude and directions of displacement vectors.[98] The new locations and velocities of mass elements were then updated from their previous values, using

implicit (or backward) Euler integration and total internal corrective force. The calculation was performed using a graphics processing unit (GPU) setup to allow for fast computations.[92]

3.2.2 Inverse elasticity estimation

An approach to estimating lung tissue elasticity from 4DCT datasets was documented in Hasse et al.[54] For clarity, we will briefly describe this technique. The work proposed a methodology to estimate lung tissue elasticity (YM) using dynamic lung information extracted from 4DCT lung images. The problem was formulated as a parameter optimization, where the aim was to determine the distribution of elasticity values that would minimize the difference between the ground-truth DVFs and those computed by the biomechanical model. The stated parameter optimization problem was solved in two steps. First, we estimated the DVF for every voxel with an HU-based initial guess elasticity distribution and changes in lung surface boundary constraints. Each lung phantom voxel was assigned an initial ground-truth YM based upon the HU value, with elasticity values ranging from 1 and 20 kPa — an extended approximation of the range of elastic moduli values for normal and fibrotic lung tissues.[89,99] We then iteratively optimized the elasticity distribution to best reproduce the registration-defined DVF. For our studies, we employed 4D lung datasets generated using the 5DCT imaging protocol. The DVFs were computed as part of the 5D model generation process, accounting for motion artifacts, large displacements, and potential sliding motion.

In the first step, lung boundary conditions were applied according to the calculated DVF and the interior elements were allowed to deform according to the generated elastic constitutive forces, as described in Section 3.2.1. The iterative scheme for estimating the elastic distribution was based on the inverse relationship between elasticity and displacement. Given an initial elasticity distribution, the constitutive model computed the volumetric displacements.[100] These

displacements were then compared with the ground-truth DVFs obtained from DIR and the effective elasticity was iteratively updated until a defined convergence threshold, or quantitative measure of agreement, between registration-defined and model-generated displacements, was met. New displacement values were then generated for each iteration by updating the effective elasticity distribution according to a modified Gauss-Newton optimization scheme.[101] Since the pleural cavity between the lung and the inner chest wall forms a hydrostatic seal, we translate the lung surface's displacement as a boundary constraint for the lung tissue's elasticity estimation. The lung surface displacement was calculated by an in-house optical flow registration framework, which has been previously validated for lungs and the head and neck.[102,103]

3.2.3 Deep neural network

The individual lung CT voxel geometry was used in conjunction with a machine learning approach to obtain corresponding elasticity distributions. During inferencing, we took as input the breath-hold CT. The DNN employed in this work was a cGAN.[104] This network consisted of two neural networks, namely Generator and Discriminator networks. The generator network enabled the generation of pseudo label images intended to match true label images in the training data. The matching and evaluation process was performed by the discriminator network. The adversarial nature of this approach enabled both networks to be developed simultaneously and continuously. Voxel-specific Hounsfield Units (HU) were evaluated as input to the cGAN, resulting in a corresponding elasticity value output from the generator network.

Generator DNN: The generator network consisted of a five-layer neural network, of which the first three layers were convolutional neural networks and the last two layers were regular fully connected neural networks.[105] During the optimization process, a series of weights and biases associated with the generator network were optimized.

Discriminator DNN: The discriminator network consisted of a four-layer neural network of which the first two layers were convolutional neural networks, and the last two layers were regular fully connected neural networks. Network accuracy was continually monitored by inferencing an output from the discriminator during the learning process. The input values to the discriminator were the pseudo label images from the generator neural network and the ground-truth labels.

To compute accuracy, the input data were processed by the hidden layers of the model, with the results passed to an additional hidden layer, and then to a final output layer. The loss function and accuracy function of the training algorithm evaluate the output layer result against the ground-truth result. The loss function, in the form of a quadratic cost, quantitatively measured the error between the output layer result and the ground-truth elasticity values.[105,106]

3.2.4 Training and validation

Fifteen lung datasets were employed for the training process while 13 lung datasets were used for validation purposes. For each training dataset, the elasticity distribution obtained through the elastography method described in Section 3.2.2 and the source geometry were considered the label and the source during the learning process. Each dataset was first separated into left and right lungs and resampled to 2D axial slices at 1-mm resolution. The training process was allowed to iterate for a fixed number of generator and discriminator updates until the reported discriminator network accuracy became stagnant.

For a quantitative study of the accuracy, we compared the ground-truth elasticity, derived using the inverse elasticity estimation procedure, with the cGAN-generated elasticity using an L2-Norm difference. It is formulated as

$$e_a = \begin{cases} 0: & \| E_a - |E_{a,0}| \| < \epsilon_1 \\ 1; & otherwise \end{cases} \tag{3-3}$$

Where $E_{a,0}$ and E_a refer to the ground-truth and model-generated elasticity of voxel a, respectively. In Equation 3-3, ϵ_1 represents the threshold elasticity value for the L2-norm for each voxel a within the lung volume V and was set to 1 kPa, consistent with previous lung elastography studies.[50,54] As a second validation approach, we reintroduced the estimated elasticity distribution and the source geometry into the biomechanical model.[52,93] The biomechanical model attempted the registration-defined lung deformations for given boundary conditions and recorded the model-generated displacements. We then compared the deformations obtained from the integrated model with the DVFs of the ground-truth 4DCT datasets. The number of voxels that converged within a defined epsilon value, ϵ_2, of ground truth was characterized as the error quantification for the cGAN-estimated lung elasticity distribution. An L2-norm difference was then applied to quantitate the voxel-by-voxel displacement differences. Letting $d_{a,0}$ and d_a be the ground-truth and model-generated displacements of voxel a, respectively:

$$c_a = \begin{cases} 1: & \| |d_a| - |d_{a,0}| \| < \epsilon_2 \\ 0: & otherwise \end{cases} \tag{3-4}$$

$$p(\epsilon) = \frac{\sum_1^n c_a}{n} \tag{3-5}$$

In Equation 3-4 above, ϵ_2 represents the threshold for the L2-norm of the deformation vector for each voxel a within the lung volume V, and c_a represents the error for each voxel. Two different epsilon values were investigated. First, we looked at $\epsilon_2 = 1$ mm, or the voxel percentage that converged within 1 mm of the ground-truth deformation matching the CT image resolution. Secondly, since lung deformation can vary widely between patients and breathing phases, we

measured the percentage of voxels that converged within 10% of the maximum deformation, or $\epsilon_2 = 0.1 \times \max_a(|d_a|)$. The percent accuracy $p(\epsilon)$ was then tabulated by summing the voxel error, c_a, over all voxels, n, in lung volume V according to Equation 3-5.

Finally, using the model-generated displacement described above, an attempt was made to warp the initial end-exhalation CT to end-inhalation geometry. The resulting warped image was then compared with the ground-truth end-inhalation CT. We investigated three image similarity metrics (ISMs), namely (a) mutual Information (MI), (b) structured similarity index (SSIM), and (c) normalized cross-correlation (NCC). MI was employed as it provided a symmetric and nonnegative similarity measure. SSIM is sensitive to structural changes of the underlying anatomy. NCC was considered as a metric that is invariant to contrast within the elasticity distribution.

3.2.5 Evaluation of Reduced Dose Images

To test the accuracy of the trained cGAN elastography model when inferenced with test images acquired at reduced dose levels, low-dose images were simulated using a noise injection algorithm.[107] Due to the fact that reducing tube current is considered the simplest and most direct method of lowering the delivered dose, the simulated images aimed to reflect the additional noise profiles present at lowered tube current-time product levels, measured as mAs.[108] Characteristic noise was injected on each 2D slice by forward projecting to estimate the attenuation of each ray. It was assumed that the scanner used a fan-to-parallel re-binning reconstruction scheme that preserved noise uniformity and sampled rays in a parallel beam fashion. The number of photons incident on the detector was calculated according to the estimation that 1.8×10^6 photons/mm^2-mAs arrive at the detector in the absence of attenuation for a typical spectrum at 120 kVp.[109] The number of photons was then multiplied by an efficiency factor E that incorporated geometric efficiency and noise from scatter (Swank factor). The noise-adding sinogram was filtered by a

smoothing function, reconstructed, and added to the original CT image, simulating a reduced dose CT scan. In a previous study by Hasse et al., efficiency factor and smoothing function were determined by reconstruction of water cylinder phantom scans using the same protocol as the clinical acquisition.[110]

FHFBCT image datasets acquired for seven patients as part of the 5DCT imaging protocol were used for reduced dose image generation and network inferencing. For each patient, an FHFBCT acquired with a current-time product of 140 mAs is used as a reference scan. Patient-specific noise profiles were characterized for each patient through the calculation of HU standard deviation in a 50 x 50 x 20 mm^3 region of interest (ROI) of the liver, due to its homogenous nature in CT. Image datasets with tube current–time products of 30, 25, and 20 effective mAs were then simulated using the noise injection method. The lowest test value of 20 mAs has been identified as a lower limit for applications such as lung cancer screenings and the evaluation of asbestosis, emphysema, bronchiectasis, and pulmonary embolism.[111]

The trained cGAN model was then inferenced using the noise injected images, at each simulated mAs value, and the resulting estimated elasticity distributions were compared to ground-truth elasticity values. The percentage of voxels differing by less than 1 kPa and 2 kPa were calculated.

3.3 Results

First, we present the cGAN elasticity results generated from the lung end-exhalation CT. Figures 3-1a, b, and c show the lung CT geometry, the underlying displacement magnitude, and the Jacobian distribution, respectively. Figure 3-1d shows the elasticity estimation associated with the lung CT.

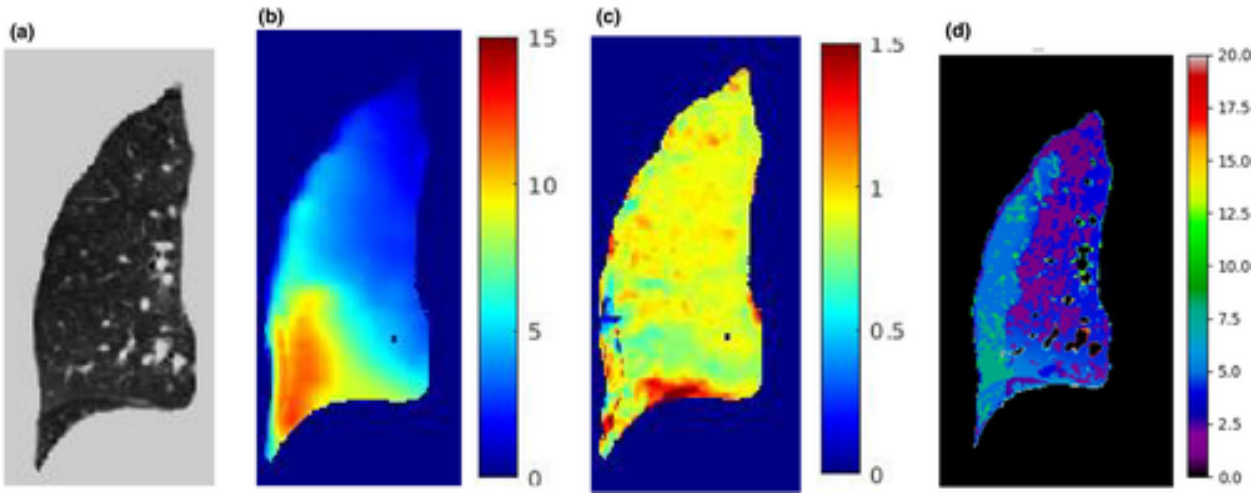

Figure 3-1: (a) The lung computed tomography (CT) geometry, (b) the underlying displacement magnitude (in mm), and (c) the Jacobian distribution are shown. (d) Shows the elasticity estimation associated with the lung CT (in kPa)

We now present the elasticity accuracy generated from the machine learning process. Figure 3-2 shows a comparison of the ground-truth elasticity (3-2a and 3-2d) and cGAN-generated elasticity (3-2b and 3-2e). It can be seen that the distributions show good agreement with each other as shown by the difference maps between the two distributions (3-2c and 3-2f). Specific lung substructures that have a higher elasticity in the ground truth also have a higher elasticity in the cGAN-generated elasticity distribution. This supports the fact that the lung elasticity distribution can be predicted using a machine learning approach.

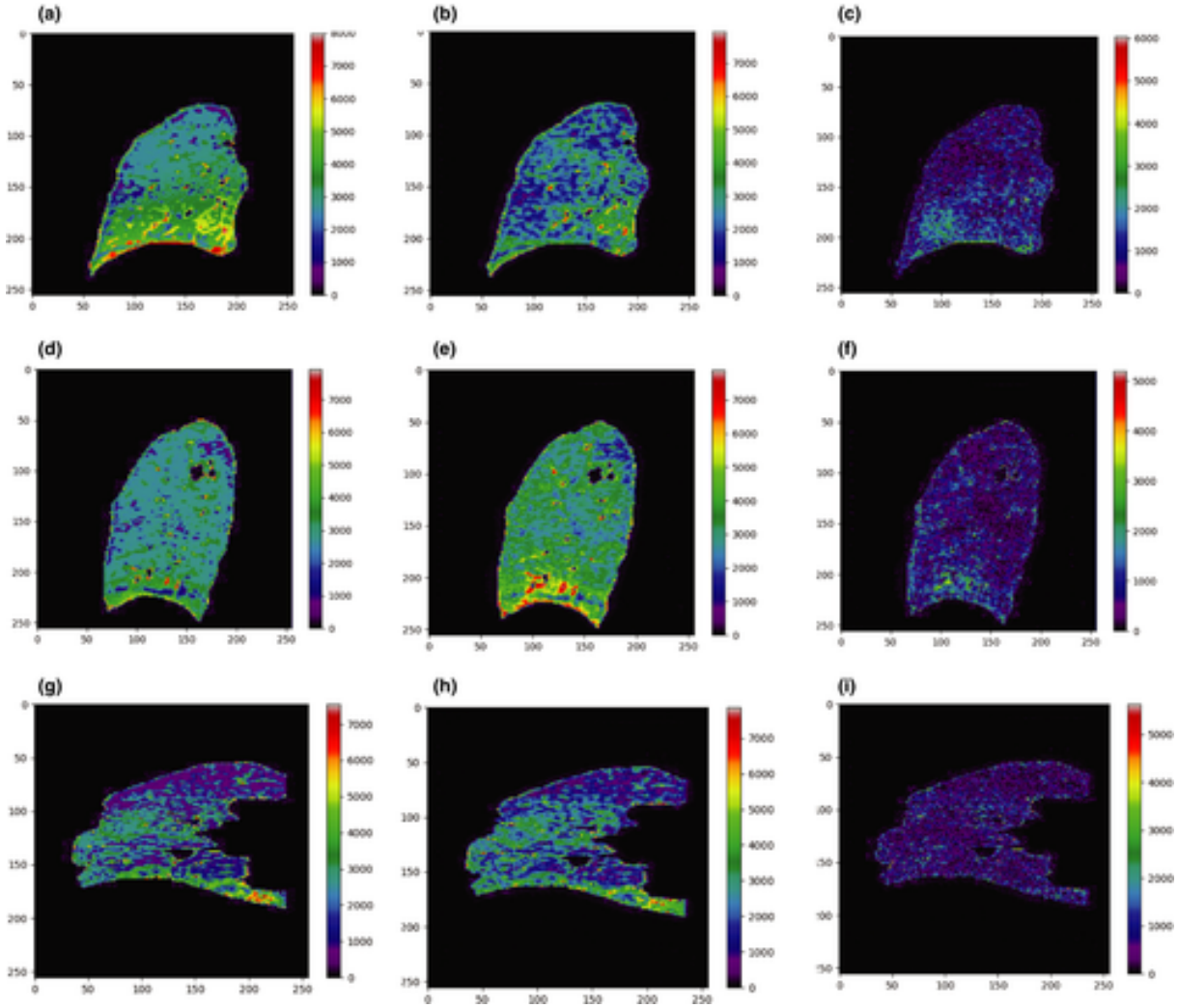

Figure 3-2: Lung tissue elasticity estimated from the biomechanical model-guided estimation for lung cancer (a and d) and COPD patients (g). Lung tissue elasticity distribution estimated from the cGAN for lung cancer (b and e) and COPD patients (h). The resulting differences in the elasticity are shown in figures c, f, and i, respectively. The units are Pascals for all images.

The elasticity distributions are known to vary from one subject to another as well as with the disease complexity. To demonstrate the ability of our learning process to account for such variations, we present the elasticity distribution for a lung cancer patient with severe COPD.

Figures 3-2g and 3-2h show a comparison between the elasticity generated as ground truth and the work presented in this paper for a subject with both lung tumor and severe COPD prevalence, respectively. Figure 3-2i shows the difference between the two estimations. As seen from the ground-truth images, the elasticity range was lower than that of the case when the patient only has a lung tumor (Figures 3-2a and 3-2d). The elasticity distributions generated by the cGAN match the ground-truth elasticity well. This supports the fact that variations in the patient geometry as well as the disease pathophysiology can be represented by the machine learning approach presented in this paper.

Figure 3-3 shows an elasticity distribution of a lung cancer subjects with (Figure 3-3a) and without COPD (Figure 3-3b). The elasticity distribution difference can be vividly seen. The purple region corresponds to (2–4 KPa) representing the COPD-affected region. The blue, green, yellow, and red regions represent ranges of (4–6 KPa), (6–8 KPa), (8–10 KPa), and (>10 KPa), respectively. The voxels in the elasticity range (2–4 KPa) represent COPD-affected regions and they can be seen to be largely present for the COPD patient. This demonstrates that the cGAN-based elasticity estimation can be effective in estimating the image-biomarker (elasticity distribution).

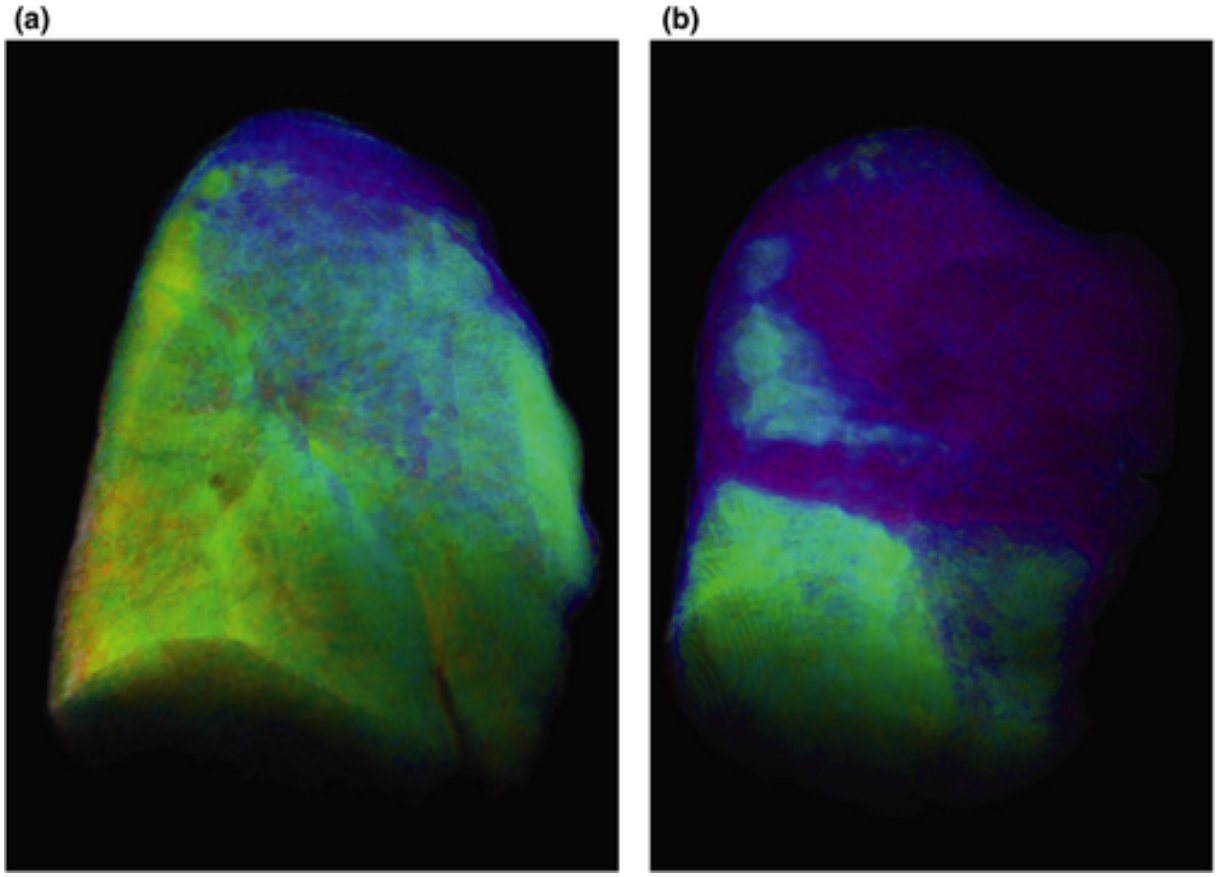

Figure 3-3: Three-dimensional conditional generative adversarial neural network generated elasticity distribution of a (a) normal cancer patient and a (b) COPD patient lung. The purple region corresponds to (2–4 KPa) representing the COPD-affected region. Blue, green, yellow, and red colors are coded as (4–6 KPa), (6–8 KPa), (8–10 KPa), and (>10 KPa), respectively

Table 3-1 documents the accuracy in learning the elasticity distributions for the 15 lung datasets. Since the current paper focuses on the DNN-based lung elasticity generation, the ground-truth results associated with the Tables 3-1 and 3-2 stem from the inverse elasticity estimation. Results show that for the training data set, we obtained a learning accuracy of 0.44 ± 0.2 KPa. For the validation dataset, consisting of 13 4D datasets, we were able to obtain an accuracy of 0.87 ± 0.4 KPa as tabulated in Table 3-2. Our previous studies for elastography showed that a difference of <1 kPa interval yields clinically agreeable deformation accuracy.[54,66] Since elasticity

is known to have a range of 0–12 kPa as documented in two of our previous papers, the current error is < 8% of the expected tissue elasticity range. These results show that the cGAN-generated elasticity correlates well with that of the ground-truth elasticity.

Patient	Accuracy (KPa)
1	0.3 ± 0.2
2	0.2 ± 0.1
3	0.4 ± 0.1
4	0.6 ± 0.2
5	0.3 ± 0.2
6	0.2 ± 0.1
7	0.2 ± 0.1
8	0.2 ± 0.1
9	0.4 ± 0.3
10	0.3 ± 0.3
11	0.2 ± 0.1
12	0.2 ± 0.1
13	0.3 ± 0.2
14	0.4 ± 0.4
15	0.2 ± 0.2
Average	**0.4 ± 0.3**

Table 3-1: Quantitative analysis of the lung elasticity estimation accuracy enabled by the deep learning framework

Patient	Elasticity Accuracy (KPa)	Deformation Accuracy (mm)
1	0.9 ± 0.7	0.8 ± 0.3
2	0.6 ± 0.5	0.6 ± 0.4
3	0.5 ± 0.3	0.4 ± 0.2
4	0.4 ± 0.2	0.3 ± 0.2
5	0.8 ± 0.4	0.6 ± 0.4
6	0.9 ± 0.3	0.6 ± 0.2
7	0.6 ± 0.4	0.5 ± 0.3
8	0.7 ± 0.5	0.5 ± 0.5
9	0.7 ± 0.6	0.5 ± 0.3
10	0.4 ± 0.3	0.3 ± 0.1
11	0.6 ± 0.5	0.4 ± 0.3
12	0.7 ± 0.3	0.6 ± 0.2
13	0.6 ± 0.4	0.4 ± 0.2
Average	0.8 ± 0.4	0.5 ± 0.3

Table 3-2: Quantitative analysis of the elasticity and displacement accuracy on testing datasets

To further quantitate the accuracy, we integrated the cGAN-generated elasticity with a lung biomechanical dynamic model for simulating the lung deformation for given boundary constraints. The displacement vectors generated from this setup were then compared with the displacement vectors generated using 4DCT DIR results. Specifically, the deformation vectors that represent a tidal breathing range were compared. Table 3-2 summarizes the results for the two accuracy measures discussed in Section 2.D. The ground-truth elasticity for the accuracy column stems from the inverse elasticity estimation process.[50] For each of the measures, the cGAN-generated elasticity facilitated an accuracy of ~89%. In addition, the average displacement accuracy was

observed to be 0.5 mm supporting the fact that the cGAN estimation elasticity closely represented the inverse elasticity estimation results.

The resulting deformed model was then transformed into lung 4DCT images and the Image Similarity Metrics (ISMs) were applied. Our results as documented in Table 3-3 show that the cGAN-generated images were very similar to that of the original 4DCT. The warped images had an average ϵ_1 and ϵ_2 accuracy of 89.5 and 88.7, respectively thereby demonstrating a close match.

Patient	ϵ_1 accuracy (%)	ϵ_2 accuracy (%)	MI	SSIM	NCC
1	87.6	87.89	1.81	0.88	0.96
2	86.08	82.9	1.99	0.83	0.94
3	94.08	84.37	2	0.95	0.99
4	87.36	89.14	1.87	0.87	0.97
5	80.63	87.72	1.77	0.87	0.96
6	85.46	87.57	1.76	0.87	0.97
7	85.83	84.14	1.62	0.86	0.95
8	99.24	75.7	1.78	0.89	0.98
9	95.55	73.79	1.5	0.92	0.98
10	82.37	75.85	1.79	0.87	0.96
11	95.41	74.64	1.8	0.91	0.98
12	88.16	78.98	1.72	0.88	0.97
13	96.48	86.46	1.57	0.91	0.97
Average	89.56	88.76	1.77	0.89	0.97

Table 3-3: Quantitative analysis of the 4DCT generated from the cGAN-generated lung elasticity distribution

The average value of the MI was 1.77 indicating the high local symmetricity between the ground truth and the cGAN elasticity-generated 4DCT data. The average value of the structural similarity for the 13 patients was observed to be 0.89 indicating the high structural integrity of the cGAN elasticity-generated 4DCT. In addition, the average NCC value of 0.97 indicated that potential variations in the contrast and brightness of the cGAN elasticity-generated 4DCT did not lead to any differences from the ground-truth 4DCT. In summary, the differences, as evaluated by the ISMs, were quite small. This bolsters the fact the cGAN-generated lung tissue elasticity can be employed within acceptable numerical boundaries.

Figure 3-4 shows example CT images at original 140 mAs and simulated 30, 25 and 20 mAs images, in a-d, respectively. Resulting elasticity distributions from inferencing the cGAN model with simulated reduced dose CT images were found to have poor agreement with ground-truth elasticity values, as reported in Table 3-4. The percentage of voxels in left and right lung differing by less than 1 kPa were consistent across the simulated mAs levels at less than 38% and 31%, respectively. Similarly, the percentage of voxels in left and right lung differing by less than 2 kPa were calculated to be less than 62% and 53%, respectively. Mean difference between the two elasticity distributions were measured to be 1.77 kPa and 2.13 kPa for right and left lungs, respectively. These results suggest that the cGAN model did not accurately predict elasticity distributions when inferenced with simulated reduced dose images.

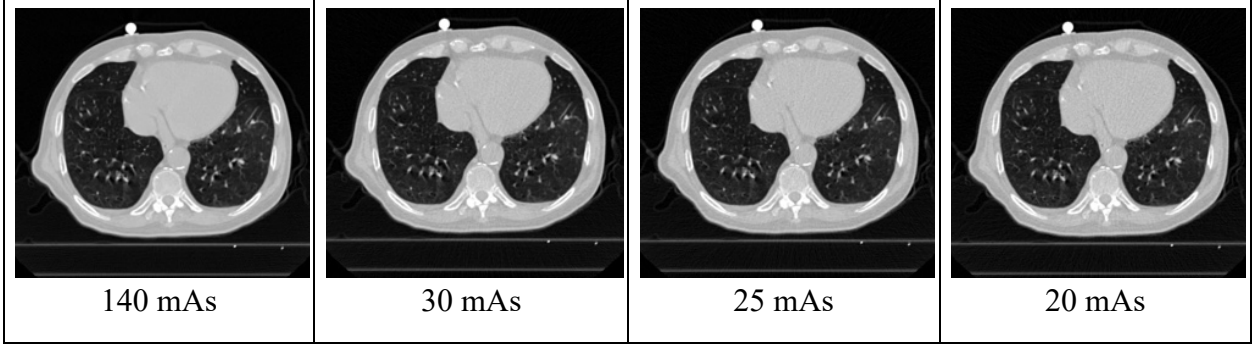

Figure 3-4: Example CT images at a) acquired 140 mAs and simulated b) 30 mAs c) 25 mAs and d) 20 mAs

Left Lung									
	% Voxels with < 1 kPa Difference			% Voxels with < 2 kPa Difference			Mean Difference (kPa)		
Patient	**30 mAs**	**25 mAs**	**20mAs**	**30 mAs**	**25 mAs**	**20mAs**	**30 mAs**	**25 mAs**	**20mAs**
3	35.55	35.48	35.38	57.02	57.08	57.06	1.88	1.88	1.89
4	35.66	35.74	35.68	63.63	63.65	63.48	1.77	1.77	1.77
6	46.75	46.59	46.53	71.18	71.15	71.10	1.48	1.48	1.48
8	42.80	42.88	42.92	68.79	68.83	68.76	1.54	1.53	1.54
14	26.51	26.42	26.54	47.97	47.93	48.09	2.15	2.15	2.15
18	32.25	32.21	31.94	59.12	59.04	58.65	1.88	1.89	1.90
20	40.21	40.05	39.66	64.30	64.14	63.84	1.65	1.66	1.67
Average	**37.11**	**37.05**	**36.95**	**61.72**	**61.69**	**61.57**	**1.77**	**1.77**	**1.77**
Right Lung									
3	39.27	39.20	39.13	62.86	62.84	62.81	1.70	1.70	1.71
4	39.50	39.50	39.47	66.26	66.23	66.22	1.69	1.69	1.69
6	26.89	26.86	26.81	44.26	44.26	44.15	2.38	2.38	2.38
8	22.41	22.28	22.38	43.97	43.96	43.88	2.40	2.41	2.41
14	21.77	21.73	21.74	39.62	39.53	39.53	2.66	2.66	2.66
18	23.53	23.53	23.64	46.82	46.78	46.81	2.29	2.30	2.30
20	37.77	37.53	37.16	60.66	60.49	60.19	1.76	1.77	1.78
Average	**30.16**	**30.09**	**30.05**	**52.06**	**52.01**	**51.94**	**2.13**	**2.13**	**2.13**

Table 3-4: Comparison of simulated reduced dose elasticity images

3.4 Discussion

In this paper, a machine learning-based lung tissue elastography method is proposed using the lung elasticity estimated from 4DCT datasets and a linear elastic biomechanical model as the training data. From a biomechanics perspective, our current work focused on using a linear elastic approach, which was applicable for most of the scenarios within the domain of lung radiotherapy. However, we envision that for more complex diffuse lung diseases, a hyper-elastic approach would be required. In the future, we would also focus on characterizing the hyper-elastic nature of the lung tissue elasticity, which will provide more information on the hyper-compliance of the diseased tissue.

The need for elasticity distributions is seen in diagnostic and therapeutic CT imaging, where elasticity distributions can potentially be used as image-based biomarkers. The ability to perform inverse elasticity estimation has been previously investigated and validated.[50] [67]Specifically, the estimated elasticity was shown as a biomarker for characterizing the degree of COPD.[51] Our ultimate vision is to develop a ML process that can compute the elasticity using a non-4D imaging modality. This was because only radiotherapy commonly uses the 4D/5D lung imaging modalities.

An additional usage of CT based lung tissue elastography is in the study of chronic diseases, such as COPD, where imaging protocols with high dosage (e.g., 4DCT protocols) are not conventionally prescribed.[51] Enabling the ability to extract lung tissue elasticity information from a single CT (e.g., end-exhalation CT) will lead to critical advancements in the treatment and management of such diseases, which forms the focus of this paper. While the current paper shows feasibility of using the machine learning approach for COPD patients, the training data cohort was small and included only four COPD lung cancer datasets. Future work would focus on using a

larger cohort of both cancer and COPD patients with known GOLD staging and phenotype information. Such a cohort will further improve the accuracy and investigating such a machine learning setup would provide great help in characterizing the lung tissue elasticity for COPD patients using only diagnostic CT images.

The ability to predict accurate elasticity distributions using low dose CT imaging techniques could allow for the extension of lung elastography to applications such as lung disease diagnosis and treatment. When our trained cGAN elastography model was tested with simulated low dose images in this study, we observed poor agreement between predicted and ground-truth elasticity values. In future work, we will investigate a transfer learning approach to take advantage of the pre-trained cGAN model in this study and due to the limited amount of available reduced dose training data. It has also been proposed that the acquisition of additional reduced dose images be added to the imaging protocol in the future as a secondary validation of the noise injection algorithm and bolstering of training data.

In this paper, we employed an end-expiration CT for generating the elasticity distribution. While it may be physically stressful for the patient to hold his/her breath during the end-expiration phase CT imaging, two specific reasons exist for using a breath-hold CT as our input data. First, our current framework is based on generating training data from 5DCT datasets and biomechanical models, which inherently generates lung anatomy at specific breathing phases that does not have motion artifacts. Secondly, the elastography also requires the lung voxels to be at any given reference phase in order to maintain the voxel's local neighborhood. While both end-inhalation and end exhalation maintain the lung anatomy in a reference phase, we chose end exhalation as our lung CT since it is considered as the resting phase during normal breathing. Future work would focus on developing a machine learning algorithm that will translate the phase specific elasticity

distribution to a given free breathing CT scan that includes motion artifacts. The results of this work will be submitted as a separate work.

In our studies, we have employed accuracy estimates (in Tables 3-1 and 3-2) that represent the absolute error in the elasticity distribution, considering the inverse elasticity estimated results as the ground truth. Table 3-2 also includes two columns of the cost function that was designed to calculate the number of voxels that does not satisfy a specific limit in the difference between the inverse estimated elasticity and the CGAN estimated elasticity. Such an accuracy study was important to quantify the percentage of voxels where clinically acceptable results were observed. Finally, using the 4DCT generated from the cGAN-generated elasticity and inverse elasticity estimation processes, we verified the proposed method's accuracy.

The cGAN training process was observed to reach convergence within the specified number of iterations. Since the training was performed only once and in a GPU environment, the computational time, although high, was not considered a limiting factor. So, the total number of iterations was set to be a high fixed value. Also, since we have two neural networks competing in an adversarial manner and constantly updating each other, an adaptive approach for stopping criteria needs to be carefully designed. Future work would focus on designing such a novel cost function for the generator DNN that will stop the learning process based on its learning gradient. In addition, a comparison to probabilistic elasticity models would be performed.[75]

Finally, the computational time for this training process approach was approximately 24 hours on a Nvidia GTX titan card. However, once trained, the network predicted the lung elasticity in near-real time. Future work would focus on developing a multi-GPU approach for the learning process, where the learning time can be significantly reduced.

3.5 Conclusions

The methods and results of a machine learning-based lung tissue elastography method presented in this paper shows the feasibility of estimating the lung tissue elasticity in real time. The input data employed for the learning process stem from a biomechanically based inverse elasticity estimation process, which was considered as a ground truth for a direct estimation of the elasticity distribution for each patient is not practical. Future work would focus on using image data from elastography imaging techniques such as the MRE, where the lung elasticity can be measured directly and will lead to more data generation for the learning process. Since the machine learning process is agnostic to the underlying imaging modality, future work would employ and integrate such imaging innovations into the learning process. In addition, for scenarios where elasticity needs to be estimated from 5DCT, the cGAN-estimated lung tissue elasticity can be used as a very close a priori value thereby leading to a smaller number of iterations.

CHAPTER 4: A quantitative analysis of lung elastography using large deformation breath-hold CT scans acquired during forced breathing

Lung elastography for forced breathing

A version of this chapter has been submitted for publication as a manuscript to Medical Physics

4.1 Introduction

Radiotherapy is a key step in an often multi-faceted intervention for patients with lung cancer.[1] In recent years, it has been established that an increasing number of lung cancer patients present an evidence-based indication for radiotherapy.[17] However, patients undergoing radiotherapy can experience severe radiation-induced lung injuries to healthy tissue when exposed to excess dose. The risk of treatment-related injury is further increased in patients with pre-existing lung diseases such as interstitial lung disease and COPD, which is found in 40-70% of patients.[3,4] In addition, greater rates of post-treatment side-effects and mortality are observed in lung cancer patients with co-morbidities.[5,6] For this reason, a greater understanding of patient-specific underlying regional lung function is necessary and several functional lung avoidance imaging and dose delivery methods have been introduced for this purpose.

Approaches to identifying functional lung tissue have previously been investigated using MRI, SPECT, and PET for ventilation and perfusion imaging.[23] However, these approaches are limited in a radiotherapy setup due to the availability of additional imaging modalities. Alternatively, nearly all lung cancer patients receiving radiotherapy undergo 4DCT simulation for treatment planning purposes due to the high geometric accuracy and electron density information important for dose calculation. For this reason, the use of already acquired CT imaging for ventilation imaging and subsequent functional lung identification has been proposed and evaluated in multiple clinical trials.[24-27] Additionally, the increased use of hypofractionated dose delivery

methods such as stereotactic body radiotherapy (SBRT) has been shown to be effective in sparing identified functional lung tissue.[28] These methods allow for the delivery of relatively large doses in fewer fractions compared to conventional methods and a rapid isotropic fall-off of dose from the tumor volume to surrounding normal tissue can be achieved.[7,8]

We envision that a CT-based characterization of patient lung function based on the measurement of specific biomechanical properties is ideal for function preserving lung radiotherapy. A quantitative measure of lung function has been identified in the measurement of elastic properties of the parenchymal lung tissue. Normal lung function depends on the production of elastin and the presence of elastic fibers throughout the lung parenchyma and the inhibition of production or degradation of existing fibers can result in lung dysfunction and diseases, such as COPD.[65] A previously proposed method for employing a well-validated biomechanical model for estimating regional elasticity distributions of lung parenchyma from free-breathing 4DCT images has been systematically studied and validated using virtual physics-based lung phantoms.[66,79] The methodology has also shown to be an effective biomarker for COPD and a good overall indicator of regional lung function.[51] Finally, a consistency study was performed evaluating the elastography method when employed for images acquired at different points in patient breathing trace.[67]

Lung deformation information obtained from DIR serves as input to lung elasticity estimation methods, in which parameter optimization is driven by the ability for a biomechanical model to accurately reproduce registration-defined deformation vectors. Previous model-based elastography studies were demonstrated using normal free-breathing scans. In these studies, regions of lung tissue, specifically in the superior lobes, did not undergo significant displacement during free breathing. The elastography model depends on DVFs obtained from DIR to accurately simulate voxel-specific displacement for biomechanical property estimation. Therefore, no motion

or minimal deformations observed for a significant number of lung voxels could hinder the ability of the model to properly characterize elasticity values for these voxels. This was quantitatively observed in a recent study, where a lobe-wise analysis of elasticity distributions derived from free-breathing datasets showed that up to 30% of voxels in a given lung lobe and 10% of total lung voxels undergo < 2 % expansion.[112] We envision that the use of scans acquired during a forced breathing maneuver will enable a more accurate characterization of the lung tissue.

A previously proposed novel convergence magnification method by Hasse et al. showed that artificially increasing the magnitude of deformation for lung voxels, which undergo relatively little displacement in the image registration-defined deformation, resulted in greater overall model convergence.[66] A newly introduced force was applied to a subset of voxels identified as minimally displaced to enforce local heterogeneity. This force is applied unidirectionally over each axis of motion to encourage convergence amongst a different subset of voxels and maximize the number of voxels reaching convergence during the elasticity estimation process.

In this study, we propose to perform elastography using CT images obtained during a forced breathing maneuver. Images acquired at residual volume (RV) and total lung capacity (TLC) and registered by DIR display substantially larger displacement values than those measured during free breathing. We hypothesize that the noted increase in the magnitude of observed lung motion will allow for a more accurate estimation of elasticity distributions, specifically in regions of the lung that experienced minimal deformation during normal breathing. Improved lung elasticity distributions obtained from the method proposed in this study could provide important additional information for characterizing regional lung function for functional lung sparing in radiotherapy treatment planning and delivery.

4.2 Materials and Methods

The purpose of this study was to evaluate the feasibility of using a well-validated biomechanical model and an elastography algorithm for processing CT images acquired during a forced breathing maneuver. Such an analysis of lung tissue elasticity estimation using CT lung images acquired during forced breathing is novel and forms the key contribution of this paper.

The outline of the methodology, described in Figure 4-1, is as follows: CT lung images acquired during RV and TLC breathing phases are taken as input. The RV image is taken as the reference image. The deformation vector field that associates each voxel in RV to the voxels in the TLC scans is first estimated (Section 4.2.2). The blood vessels are segmented from the RV scans and masked since the tissue elasticity estimation process involves only the parenchyma, as explained in Section 4.2.3. A biomechanical model of the lung parenchyma is then assembled in the RV geometry with the lung boundary and the blood vessels forming the boundary conditions (Section 4.2.4). The DVFs associated with the voxels making up the lung boundary are then employed as boundary constraints to estimate the parenchymal lung tissue elasticity, as detailed in Section 4.2.5.

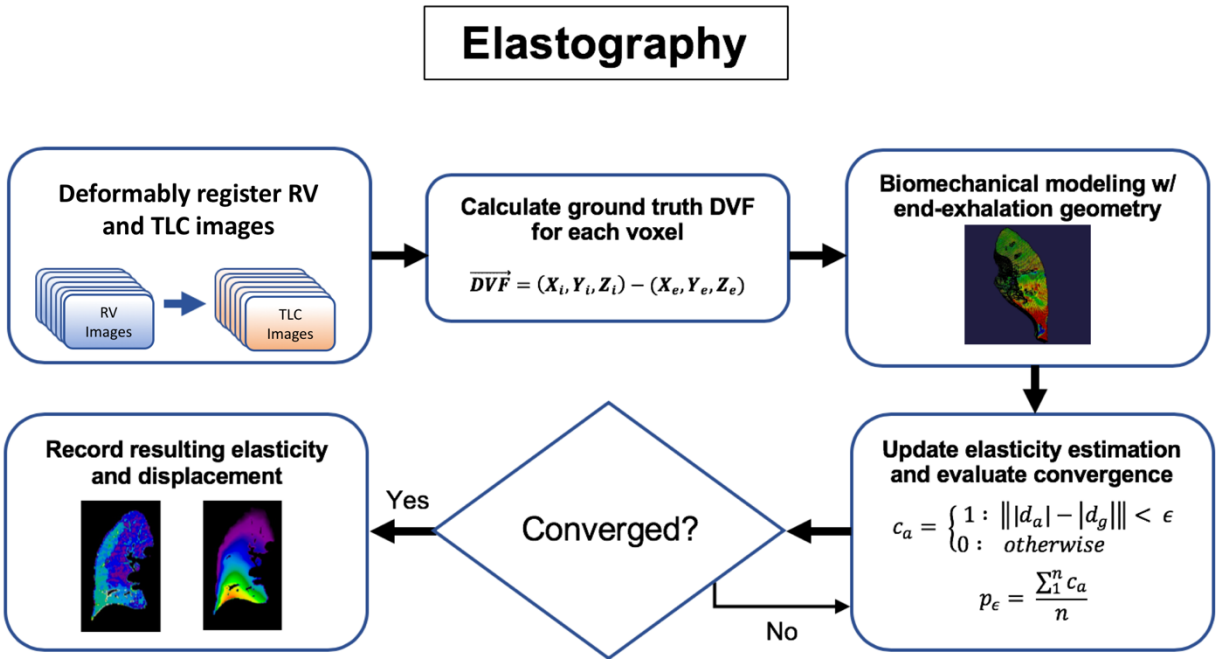

Figure 4-1: Flowchart of elastography workflow[67,79]

4.2.1 Data Acquisition

This work utilized 10 retrospective patient datasets originally acquired as part of the Endobronchial Valve for Emphysema Palliation Trial (VENT) clinical trial (ID: NCT00129584).[40] CT acquisition was performed by the imaging core at the David Geffen School of Medicine at UCLA. Images were acquired during a breath hold at both TLC and RV and reconstructed with slice thickness ranging from 1.25 to 3 mm with subsequent interpolation to 1 x 1 x 1 mm^3 voxels. A Siemens Sensation 16 scanner with the following parameters was employed for this purpose: 120 kVp, 80 effective mAs, 0.5 sec. rotation time, 16 × 0.75 mm collimation, and 18 mm/rotation table feed with pitch 1.5.[113] Images acquired for the VENT clinical trial have previously been used in several studies evaluating endobronchial valves for emphysema patients and investigating the use of CT lung volume measurements.[41,114-116]

4.2.2 Deformable Image Registration

A published DIR algorithm, as described in Vishnevsky et al., was employed to obtain DVFs between RV and TLC images.[117] In this method, isotropic total-variation regularization, and linear grid interpolation were used to perform parametric image registration. The registration algorithm has been shown to accurately approximate anatomical sliding motion, which is necessary to properly model sliding interfaces in the thoracic region. Estimation of the displacement field mapping a moving image to a fixed image was defined as the following optimization problem:

$$\mathrm{d}^* = argmin\, \mathcal{F}(\mathrm{d}) = argmin\, E_D(\mathrm{d};\, \mathrm{f_f}, \mathrm{f_m}) + \lambda E_R(\mathrm{d}) \tag{4-1}$$

Where d^* represents the optimal displacement field, d is the current displacement field, E_D represents a dissimilarity metric calculated between the fixed ($\mathrm{f_f}$) and moving ($\mathrm{f_m}$) images, E_R is a regularization term, and λ is a parameter that controls the regularization strength and is tuned for each type of application.

Isotropic total variation (TV), which considers all components of the displacement gradients collectively, was found to better describe motion that is not aligned with Cartesian axes than a previously proposed anisotropic TV method.[118] The TV spatial displacement regularization (E_R^{TV}) of the displacement field was calculated as:

$$E_R^{TV}(\mathrm{d}) = v \sum_{l \le L} \sqrt{\sum_{i,j \le N} (\nabla_i \mathrm{d}_j\,[l])^2} = v \|\mathcal{D}(\mathrm{d})\|_{2,1} \tag{4-2}$$

Where v represents the voxel volume, L is the number of voxels in the image, l is the voxel index, N is the number voxel dimensions, i and j are voxel position coordinates, and $\mathcal{D}(\mathrm{d})$ are the directional displacement gradient vectors.

A common limitation with DIR has been the poor performance of gradient descent methods in solving non-differentiable convex terms. To address this limitation, a variant of the dual descent

method termed alternative direction method of multipliers (ADMM) was employed. Parametrization of the displacement field was performed by interpolating displacements on a control point grid, followed by a 1st-order B-spline to bound interpolated values between adjacent control points and enable sharper transitions. Registration quality was dependent on three tunable parameters. First, a regularization parameter, λ, that considered modality, noise, and approximate amount of motion. Second, a weighting kernel bandwidth, ω, which depends on the image modality and pixel resolution. Lastly, control point grid spacing, K, for which small values of K give finer grid resolution and greater degrees of freedom in the transformation but come with an increased computational cost. For this study, these values were identified, according to the parameter sensitivity analysis described in Vishnevskiy et al., to be 0.15, 2.5 pixels, and 4 x 4 x 4 voxels for λ, w, K, respectively.

4.2.3 Image Segmentation for Elastography

Due to the non-expanding behavior of blood vessels and other rigid substructures within the lung, we segmented the parenchymal tissue for analysis in this study. In order to remove vessels and other non-parenchymal structures, CT images were segmented with a designated threshold of -700 HU in our elastography estimation workflow.[119] Karimi et al. found that a threshold value of -700 HU may be used to separate high-density lung tissue and ensure the exclusion of voxels containing vessels and borders of dense structures.[80]

4.2.4 Biomechanical Model

A forward biomechanical model proposed and validated in previous publications by Hasse et al. and Neylon et al. was utilized in our elasticity estimation framework.[52,66] For clarity, we now present an overview of the biomechanical model. Lung geometry was represented as finite mass elements positioned at the center of each voxel in the CT image. The total simulated lung geometry

was deformed by applying changes to the boundary constraint voxels, as defined by the associated DVF values obtained from DIR. The deformation process is an iterative one, defined by a set number of incremental displacement changes and followed by another set number of timesteps during which the displaced voxels may settle at their newly defined locations in the deformation space. During the deformation process, resulting corrective forces are enacted on each inner mass element at pre-defined simulation timesteps (δ) and recorded. The total force $\vec{f}_a$ on each element, a, was calculated by summing the elastic ($\vec{f}_{E,ab}$), shear ($\vec{f}_{S,ab}$), and dashpot damping ($\vec{f}_{v,ab}$) forces, exerted by each connected element, b.[79]

$$\vec{f}_a = \sum_b \left(\vec{f}_{E,ab} + \vec{f}_{S,ab} + \vec{f}_{v,ab}\right) \tag{4-3}$$

The elastic force between each connection was calculated by:

$$\vec{f}_{E,ab} = \sum_b \left(E_{ab} * \frac{\Delta L_{ab}}{L_{ab}}\right), \tag{4-4}$$

where E_{ab} represents the effective Young's modulus, L_{ab} is the rest length distance, and ΔL_{ab} is the incremental change in rest length distance between connected elements.

New element position ($\vec{x}_a^{n+1}$) and velocity ($\vec{v}_a^{n+1}$) are updated after each timestep, δ, via implicit Euler integration and the total internal corrective force imposed by incremental changes in rest length distance between connected elements:

$$\vec{v}_a^{n+1} = \vec{v}_a^n + \left(\frac{\vec{f}_a}{m_a} + \vec{g}\right)\delta, \tag{4-5}$$

$$\vec{x}_a^{n+1} = \vec{x}_a^n + \vec{v}_a^{n+1}\delta, \tag{4-6}$$

where m_a is the mass of element a and $\vec{g}$ is the gravitational force. Finally, the measured displacement for each element was calculated as the Euclidean distance between the initial and final positions at the conclusion of each iteration.

4.2.5 Elastography

The inverse elasticity problem was formulated as a parameter optimization problem, in which we aimed to determine an elasticity value that minimized the difference between the ground-truth DVFs and those computed by the biomechanical model during elastography. Finite mass elements were connected with neighboring elements by linear elastic connections. Each connection was assigned a randomly generated elasticity value from a defined HU-based range which was applied as a Young's modulus and Poisson's ratio during model initialization. The following elasticity estimation approach consisted of an iterative process of biomechanical property estimation and inverse deformation methods.

An HU-based elasticity search space was defined for each element with defined minimum ($E_{min,a}$) and maximum ($E_{max,a}$) elasticities. A gradient descent optimization was then employed to iteratively update voxel-specific elasticity values. Beginning with randomly assigned elasticity values during model initialization, elements were incrementally displaced according to DIR-generated DVFs, as allowed by their assigned biomechanical properties. After each iteration of the model, displacement differentials and subsequent elasticity limit updates were calculated for evaluation:

$$\Delta d_a = d_{0,a} - d_a \begin{cases} \Delta d_a < 0: & E_{min,a} = E_a \\ & E_{max,a} = E_{max,a} \\ \Delta d_a > 0: & E_{min,a} = E_{min,a} \\ & E_{max,a} = E_a \end{cases}, \tag{4-7}$$

where Δd_a is the difference between registration and model-generaed displacement magnitudes, $d_{0,a}$ is the registration defined displacement magnitude and d_a is the model-generated displacement magnitude for a given iteration. New voxel-specific elasticity values E_a were then calculated and applied in the next iteration of the model.

$$E_a = \frac{(E_{min,a} + E_{max,,a})}{2} \tag{4-8}$$

This iterative elasticity update for each parenchymal voxel continued until the convergence criteria were met.

4.2.6 Convergence Metrics

The optimization process iteratively updated voxel-specific elasticity values until a defined percent accuracy within 0.5 mm (p_ϵ) for ≥ 95% of voxels was accomplished or the maximum iteration limit of 100 was reached. A second convergence criterion evaluated the percentage of voxels converged within 10% of the maximum deformation, or $\epsilon_2 = 0.1 * \max_a(|d_a|)$. Upon criteria satisfaction, the resultant elasticity and the model-achieved displacement vector were recorded for each voxel. Convergence status and percent accuracy p_ϵ were calculated as follows:

$$c_a = \begin{cases} 1: & \|d_a - d_g\| < \epsilon \\ 0: & otherwise \end{cases} \tag{4-9}$$

$$p_\epsilon = \frac{\sum_1^n c_a}{n} * 100 \tag{4-10}$$

where c_a represents the convergence status with a value of 1 if the L2-norm of the difference between model-achieved displacement (d_a) and registration DVF value (d_g) is less than the defined threshold value $\epsilon = 0.5$ mm. In Equation 10, the percent accuracy is then defined as the sum of the error (c_a) divided by the total number of voxels (n) in the geometry and multiplied by 100.

4.2.7 Quantitative Validation

For quantitative evaluation of model performance during the elastography process, final model-generated displacements were evaluated against registration defined DVFs. First, we computed the percentage of voxels differing by less than 1 mm, which was the spatial resolution limit of our datasets. Similarly, the percentage of voxels converging within 2 mm of the registration

defined displacement values were measured. This value was chosen as it was found to be approximately 5% of the mean maximum observed displacements across the deformably registered datasets. In addition, Jacobian determinant values representing the expansion of each voxel in the anatomy were calculated using both registration and model-achieved DVFs.

A landmark validation tool was utilized to evaluate the accuracy of registration and model-generated DVFs.[120] This involved the manual selection of 100 landmarks per patient located at the boundaries of identifiable structures (e.g. bifurcations, sharp transitions, and other structures) on the source CT images. An example distribution of landmarks for a single patient is provided in Figure 4-2a. Additionally, Figure 4-2b shows the result of a k-means clustering performed with a k-value of 6, determined by locating the inflection point on the plot of the sum squared distance between each point and the centroid of its defined cluster. Displacement vectors were then applied to manually selected landmark voxels and the user was prompted to choose manually identified ground-truth locations in the corresponding target images. Target registration errors (TRE) were then calculated as the Euclidean distance between the model-generated voxel displacements and the ground-truth locations.

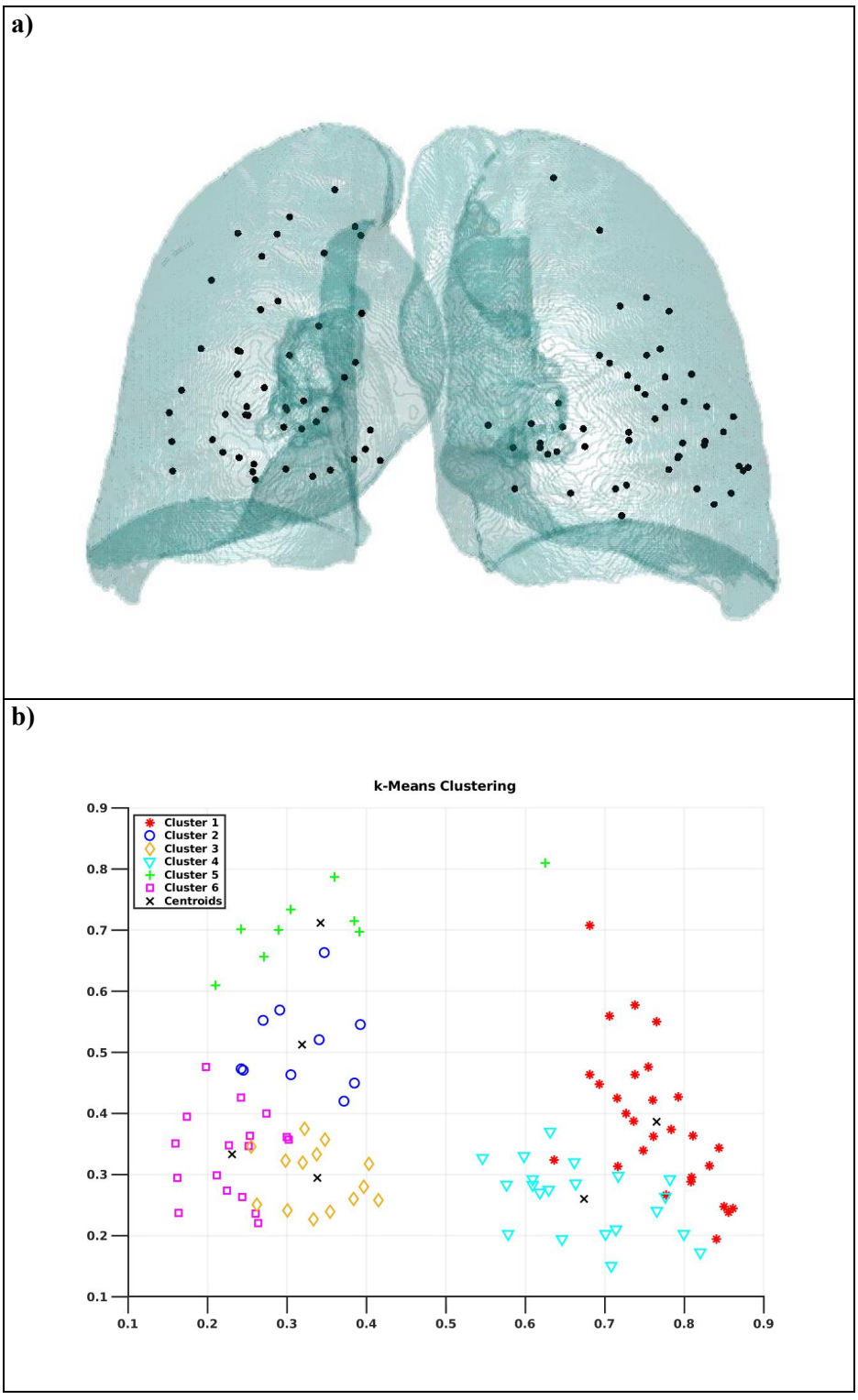

Figure 4-2: a) Distribution of landmarks displayed on rendered lung anatomy and b) the k-means clustering results with centroid locations

In addition, the landmark validation tool calculated several regional image similarity metrics (ISMs) between target and warp images, which were created by applying the DVF vectors to source images to generate pseudo-target images. For each manually selected landmark point, a 20 mm^3 volume centered at the corresponding target image point (*t*) was compared to the same volume at the same location in the warp image (*w*). One ISM calculated between these regional volumes included structural similarity index (SSIM), which considered patterns of pixel intensities and the loss of structural information between images:[121]

$$SSIM\ (t,w) = \frac{(2\mu_t\mu_w + C_1)(2\sigma_{tw} + C_2)}{(\mu_t^2 + \mu_w^2 + C_1)(\sigma_t^2 + \sigma_w^2 + C_2)} \tag{4-11}$$

where *t* and *w* represent the target and warp volumes being compared, μ is average pixel value, σ_{tw} is the covariance of t and w, σ is standard deviation, and C_1 and C_2 are constants introduced to avoid instability in the case of denominator terms approaching 0.

The second ISM calculated was the Normalized Cross-Correlation Coefficient (NCC), which calculated correlation for multiple basis functions present in one volume matrix and produced a weighted-sum correlation value to a separate volume matrix. NCC is calculated according to Equation 12:

$$NCC(t,w) = \frac{\sum_{i,j}(t(i,j) - \bar{t}) * (w(i,j) - \bar{w})}{\sqrt{\sum_{i,j}(t(i,j) - \bar{t})^2 \ \sum_{i,j}(w(i,j) - \bar{w})^2}} \tag{4-12}$$

where *t* and *w* represent target and warp volumes, *i* and *j* are voxel position coordinates, and $\bar{t}$ and $\bar{w}$ are mean target and warp values. These ISMs have also been used in previous works to evaluate elasticity distributions and DVFs.[67,79]

4.3 Results

Example patient lung geometries at RV and TLC, and an overlay of the two, are shown in Figure 4-3, displaying the large deformations that typically occur during forced breathing

maneuvers as can be seen in the inferior lung. These images also represent the antero-posterior motion that causes some blood vessels to be visible in only one of the images.

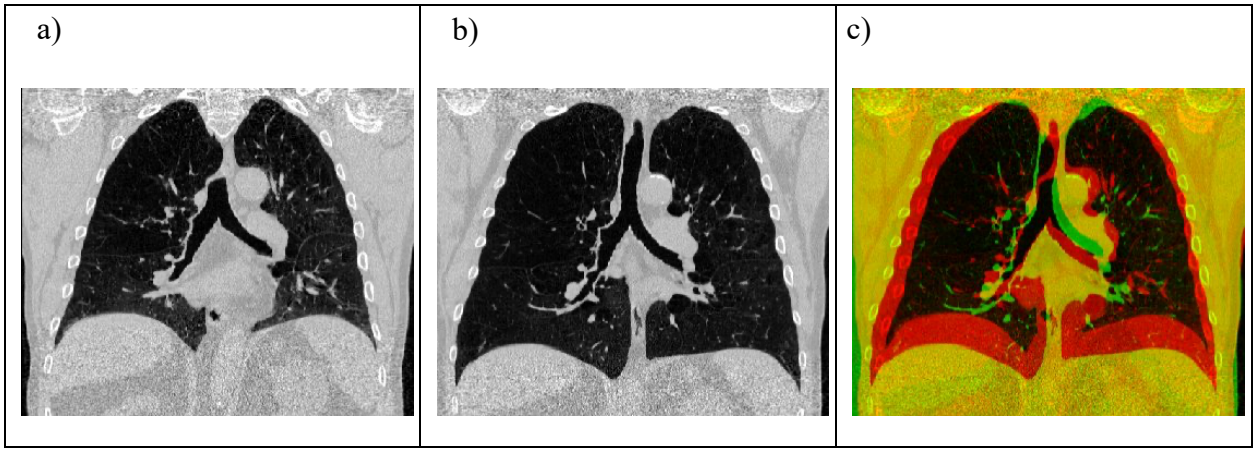

Figure 4-3: Example CT slices for a patient 5 showing a) RV (5.11 Liters), b) TLC (7.80 Liters) geometry, and c) an overlaid image where red and green represent RV and TLC, respectively

As shown in Table 4-1, the mean and maximum distances measured between identified landmark points in RV and TLC geometry, prior to image registration, were 19.45 ± 5.78 mm and 32.60 ± 11.28 mm, respectively. TRE and ISM values calculated for each patient using the landmark validation tool, described in Section 2.6, are displayed in Table 4-2. The average TRE across 10 patients was 1.09 ± 0.57 mm. Average ISM values computed between corresponding regions in the target and warp images were 0.71 ± 0.05 and 0.88 ± 0.03 for SSIM and NCC, respectively. These values demonstrate high registration accuracy between the RV and TLC datasets.

Euclidean Distance between identified landmarks in RV and TLC		
Patient	**Mean Distance (mm)**	**Max Distance (mm)**
1	27.52 ± 12.44	47.43
2	26.54 ± 11.15	43.09
3	24.12 ± 12.32	43.19
4	11.57 ± 4.37	19.26
5	23.62 ± 12.26	44.59
6	16.15 ± 8.20	26.57
7	17.62 ± 7.56	32.14
8	11.68 ± 4.04	16.03
9	19.39 ± 7.19	28.23
10	16.32 ± 6.32	25.50
Average	19.45 ± 5.78	32.60 ± 11.28

Table 4-1: Pre-registration distances between RV and TLC for landmark points

Landmark Validation Results for Registration				
Patient	**Mean TRE (mm)**	**Max TRE (mm)**	**SSIM**	**NCC**
1	1.42 ± 0.55	15.25	0.74 ± 0.11	0.92 ± 0.05
2	0.62 ± 0.78	7.23	0.67 ± 0.08	0.87 ± 0.06
3	1.34 ± 1.72	3.83	0.74 ± 0.08	0.92 ± 0.04
4	0.55 ± 0.35	1.53	0.71 ± 0.09	0.90 ± 0.05
5	2.52 ± 0.66	16.41	0.63 ± 0.15	0.81 ± 0.15
6	1.06 ± 1.29	6.22	0.65 ± 0.07	0.85 ± 0.05
7	0.94 ± 0.87	4.26	0.70 ± 0.07	0.88 ± 0.05
8	0.82 ± 0.33	1.69	0.72 ± 0.07	0.87 ± 0.06
9	0.84 ± 0.42	1.98	0.70 ± 0.06	0.90 ± 0.03
10	0.80 ± 0.38	1.48	0.81 ± 0.03	0.92 ± 0.04
Average	1.09 ± 0.57	5.98 ± 5.56	0.71 ± 0.05	0.88 ± 0.03

Table 4-2: Landmark validation analysis of registration-produced DVFs including TRE and local ISMs

The average percentages of voxels with model-generated and DIR-defined displacement magnitudes converging within 1 mm were found to be 93.5 ± 0.05% and 94 ± 0.04% for the left and right lungs, respectively. Similarly, the average percentages of voxels converging within 2 mm were found to be 98.8 ± 0.01% for both the left and right lungs, as reported in Table 4-3. This high rate of convergence reflects the accuracy of the estimated elasticity values through the DIR-generated deformations reproduced by the biomechanical model with the assigned optimized biomechanical properties.

In addition, the average maximum displacements were observed to be 40.2 ± 11.1 mm and 34.9 ± 9.15 mm for the left and right lungs, respectively. Mean displacement values were 15.9 ± 5.57 mm and 14.7 ± 4.09 mm for the left and right lungs, respectively. These displacement magnitudes are also presented for each patient in Table 4-3 and show significantly larger deformations than those observed in images acquired during free breathing. For comparison, in a study by Hasse et al., for which elastography was performed for 15 free-breathing CT datasets, average mean and maximum displacements were reported to be 6.24 ± 0.790 mm and 16.57 ± 5.03 mm, respectively.[79] These values are shown in Table 4-4. Given the significant difference between mean and maximum displacement values recorded for free- and forced-breathing lung deformations and the convergence magnification method proposed in Hasse et al., a more accurate elasticity estimation could be obtained for voxels that underwent minimal displacement during free breathing.

Patient	1 mm Convergence (%)		2 mm Convergence (%)		Max Displacement (mm)		Mean Displacement (mm)	
	Left	Right	Left	Right	Left	Right	Left	Right
1	87.7	92.7	97.6	97.6	55.6	43.3	20.2	17.6
2	93.5	94.9	99.2	98.9	48.6	35.5	27.2	14.7
3	87.0	87.6	96.8	97.0	50.6	53.7	20.4	17.4

4	94.7	92.1	99.3	99.3	27.1	27.7	10.0	9.10
5	87.5	91.7	96.4	98.3	49.9	40.2	18.5	18.6
6	94.0	98.4	99.6	100.0	35.7	34.2	13.9	20.8
7	97.3	97.8	99.8	99.9	40.7	29.4	12.8	10.4
8	99.2	98.7	100.0	100.0	21.1	20.7	9.2	9.5
9	96.1	87.0	99.4	97.0	36.8	31.8	14.2	16.0
10	98.4	98.9	100.0	100.0	35.7	32.2	12.7	12.6
Mean	93.5 ± 0.05	94.0 ± 0.04	98.8 ± 0.01	98.8 ± 0.01	40.2 ± 11.1	34.9 ± 9.15	15.9 ± 5.57	14.7 ± 4.09

Table 4-3: Convergence of model-generated with registration defined displacement vectors and maximum and mean displacement values

Patient	Mean Displacement (mm)	Max Displacement (mm)
1	7.66	20.30
2	5.87	6.31
3	6.23	8.58
4	4.91	12.12
5	7.07	26.31
6	6.37	14.85
7	6.72	15.68
8	6.79	19.97
9	6.45	17.32
10	5.17	16.99
11	5.37	18.58
12	6.14	20.32
13	7.25	15.53
14	6.20	21.11
15	5.46	15.59
Average	**6.24 ± 0.790**	**16.57 ± 5.03**

Table 4-4: Mean and maximum displacements observed in free-breathing patient datasets as reported by Hasse et al.

For elastography performed with images acquired during forced breathing, the mean elasticity values for the left and right lungs were recorded to be 3.54 ± 1.04 kPa and 3.27 ± 0.38 kPa, respectively. Elasticity distribution analysis results are tabulated in Table 4-5. The mean left and right lung elasticity values of 3.56 kPa and 3.57 kPa were consistent with a similar elastography study performed with free-breathing images of COPD patients.[112] In a previous publication from Hasse at al., an increased percentage of voxels with elasticity values in the 1-3 kPa range (%$Elast_{1-3}$) was proposed as a biomarker for COPD. For the patients in this study, the average %$Elast_{1-3}$ for the left and right lungs were 40.69 ± 10.64% and 43.35 ± 11.82%. These values are indicative of significant regions of disease-affected lung and suggest that these patient datasets have global elasticity measures consistent with COPD patients as identified in previous studies.

Patient	Mean Elasticity (kPa)		%YM1-3	
	Left	Right	Left	Right
1	3.58 ± 1.65	3.12 ± 1.45	34.49	47.70
2	3.19± 1.41	3.24 ± 1.47	40.16	41.31
3	6.38 ± 1.12	2.70 ± 1.12	0.02	62.96
4	3.42 ± 1.61	3.62 ± 1.50	39.82	34.62
5	3.51 ± 1.58	3.73 ± 1.46	36.92	29.59
6	3.46 ± 1.36	3.78 ± 1.45	38.37	24.87
7	3.00 ± 1.61	2.89 ± 1.49	51.08	53.30
8	2.93 ± 1.50	3.13 ± 1.42	57.01	50.32
9	3.32 ± 1.64	3.56 ± 1.27	42.55	30.65
10	2.62 ± 1.40	2.96 ± 1.36	66.47	58.24
Mean	3.54 ± 1.04	3.27 ± 0.38	40.69 ± 10.64	43.35 ± 11.82

Table 4-5: Mean elasticity values and percent voxels in 1-3 kPa range

Figure 4-4 shows example registration- and model-generated displacement magnitude colormaps along with a difference colormap and associated CT RV geometry. In accordance with reported convergence levels above, it was observed that differences between registration and model displacement outputs were minimal. Examples of resulting elasticity distributions and associated geometry are shown in RV geometry in Figure 4-5. As mentioned previously, resulting elasticity distributions were consistent with those of COPD patients in previous elastography studies.

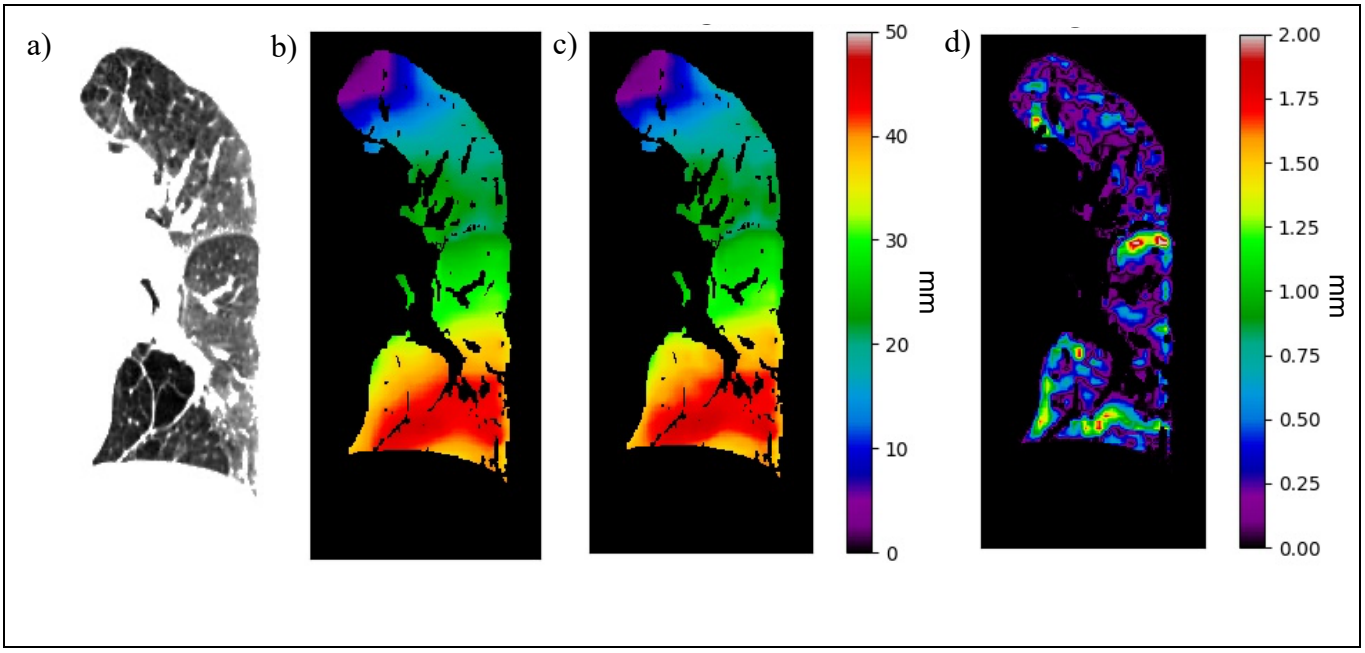

Figure 4-4: CT source image and displacement magnitude distributions for (a) registration and (b) model-generated outputs; (c) Difference map (in mm) in RV geometry

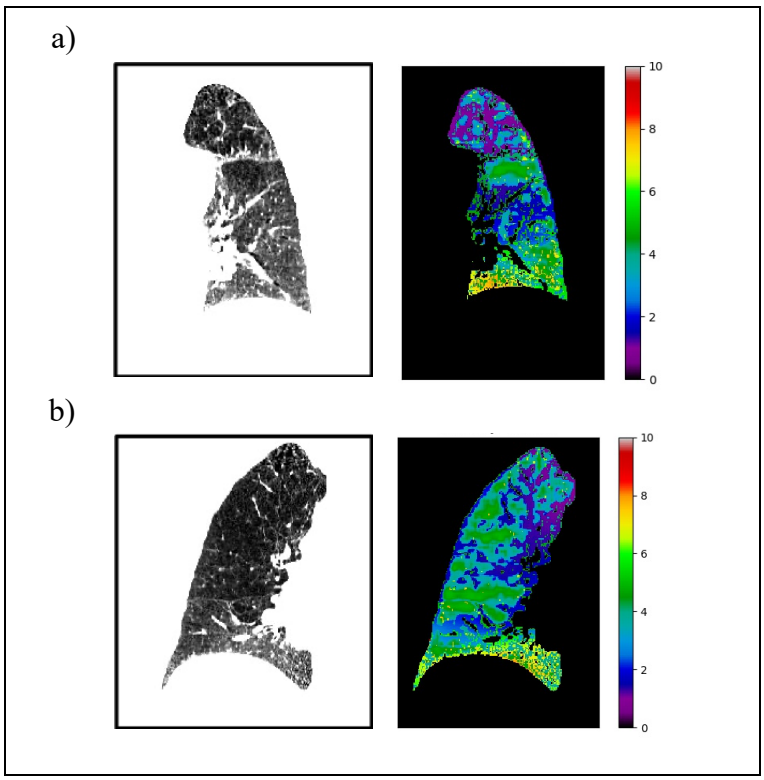

Figure 4-5: Elasticity distributions for (a) left and (b) right lung, shown in RV geometry

4.4 Discussion

In this paper, we present a feasibility study applying an elasticity estimation framework for images acquired during forced breathing maneuvers. The high level of convergence observed between registration- and model-generated displacement magnitude demonstrates the feasibility of performing elastography using breath-hold images representing relatively large deformations when compared to those recorded during free-breathing.

Images acquired during RV and TLC demonstrate a large deformation for each patient. Due to the mechanisms and corrective force calculations involved, elasticity values can be more accurately measured in regions where significant expansion occurs. Using images with such large deformations in the elastography process greatly reduces the percentage of lung voxels that do not expand significantly relative to free-breathing images. This was shown by a comparison of the

percentage of non-expanding voxels, as defined by Jacobian value, present in elasticity distributions obtained using forced vs. free-breathing images. For this reason, the additional acquisition of breath-hold CT scans at RV and TLC would be beneficial to the assessment of lung function through elastography for patients undergoing radiotherapy treatment.

Convergence levels between model- and registration-generated displacement vectors were used in this study to evaluate the elasticity distribution estimations. We envision that future work will include the acquisition of images at both free-breathing and forced-breathing for the same patient. Performing elastography on both datasets and analyzing differences in regional distributions could reveal additional functional information useful to the sparing of healthy tissue in radiotherapy treatment planning and other lung interventions.

In a related work by Hasse et al., elasticity distributions obtained from elastography with free-breathing images were used in retrospective functional avoidance treatment planning and they were able to reduce dose to functional lung regions.[55] Future work will also include a similar study with elasticity distributions generated from forced breathing images. This could result in improved functional lung sparing during radiation therapy.

The current approach to lung vessel and rigid structure segmentation in CT images is performed by applying a simple threshold that ensured the exclusion of non-parenchymal tissue. More sophisticated vessel identification methods are currently being investigated and will be employed in future work.

One limitation of the current approach is the lack of consideration of airflow dynamics in the biomechanical model. Achieving an accurate representation of airflow and pressure distributions within the lung geometry is current being investigated.[122] Our initial results have demonstrated that such airflows can be simulated with 5D imaging datasets.[68] Airflow dynamics

can be a determining factor in informing a biomechanical modeling approach, particularly for patients with lung diseases that cause obstructed airflow and narrowed airways. Our future work will focus on adding the airflow dynamics to develop a multi-physics-based elasticity estimation process.

A potential limitation of this study was the linear elastic nature of the connections between finite elements in the modeled lung geometry. While this approach is capable of accurately modeling elastic properties and deformations within a certain range of breathing amplitudes, several studies have suggested that a hyperelastic lung model may be more accurate when modeling forced breathing maneuvers. Our future work will focus on an imaging protocol that acquires both free and forced breathing CT scans, which will facilitate the modeling of hyper-elastic behavior.

4.5 Conclusion

In this study, a biomechanical modeling framework was employed to solve an inverse elasticity optimization problem posed by the deformation of patient lungs from RV to TLC geometry. Measured convergence rates between DIR- and model-generated displacement magnitude showed good agreement was achieved when applying the calculated optimal elasticity distributions. Thus, we established the feasibility of performing elastography using images acquired during a forced breathing maneuver. In combination with recent efforts toward functional lung sparing for radiotherapy, elastography performed using forced maneuver images could provide additional information about the underlying tissue physiology that could not previously be obtained through elastography using only free-breathing images or other methods.

CHAPTER 5: Scalable Quorum-based Deep Neural Networks with Adversarial Learning for Automated Lung Lobe Segmentation in Fast Helical Free Breathing CTs

Quorum-based Automated Lung Lobe Segmentation

A version of this chapter has been published as a manuscript: Int J Comput Assist Radiol Surg, Vol. 16, 2021. doi: 10.1007/s11548-021-02454-6

5.1 Introduction

Radiotherapy planning for lung and liver tumors has benefitted from 5D acquisition of the thoracic deformations.[123,124] In addition, novel applications of the 5D protocol have been investigated for surgical applications such as lobectomy and LVRS. Advances in these surgical techniques (minimally invasive approaches and sub-lobar resections) as well as perioperative care with improved outcomes are challenging historical criteria on how patients are evaluated for operative candidacy.[33] For the current surgical applications, tasks such as patient selection are critical to ensure clinically acceptable post-operative pulmonary complications (PPC) and mortality rates.[34] Current strategies for patient selection involve PFTs which are approximate and do not consider lung physiology and function heterogeneities. As an example, Baldi et al [125] showed that patients with FEV1/FVC > 70% of predicted values had reduced post-lobectomy FEV1/FVC, while patients with FEV1/FVC < 55% of predicted values had an increased post-lobectomy FEV1/FVC, indicating that the removed lobes of patients with poor preoperative lung function might have had worse function than their remaining lung.

Recent advancements in CT imaging have led to improved characterization of lung heterogeneity and pulmonary lung function.[126] In addition, lung biomechanics and airflow dynamics modeling have been developed by peers and our team of investigators to the extent that

they can provide patient-specific models. However, such strategies have not been integrated into the patient selection process for lung interventions such as lobectomy and LVRS.

Commercial 4DCT imaging protocols were inspired by 4D cardiac imaging and assumed breathing cycle regularity. Many COPD patients cannot breath regularly [127], causing breathing-sorting artifacts, which significantly degrade biomechanical property estimation efforts. Since biomechanical model instantiation of diseased lung anatomy largely depends on artifact-free image data, we avoid the historical challenges of commercial 4DCT by utilizing a Fast Helical Free Breathing CT (FHFBCT) protocol for lung model development efforts.[123,128] FHFBCT has several advantages including that it is free breathing, has no sorting artifacts, is acquired over a number of breathing cycles, and delivers relatively low dose.

Lobe segmentation is one of the tasks required to simulate the underlying planning process for surgical lung procedures, a process that is impractical to perform even semi-automatically for the number of images we propose to use. An accurate segmentation of the lung lobes from the FHFBCT scans is critical to our proposed workflow. Current state-of-the-art approaches in lobe segmentation use breath-hold CT as data and use algorithms that identify vessels and lobe fissures and couple them with lobe shape models to identify the lobes of the lung.[129,130] While these algorithms are automatic, they are known to produce inaccurate results because of patient anatomy variations. Furthermore, applying a semi-automatic segmentation requiring manual correction for 25 CT scans (number of scans in FHFBCT) would be impractical in a clinical setup.

In this paper, we present a machine learning approach for automatic lung lobe segmentation in CT datasets that has been observed to be more precise than the current state-of-the-art algorithm in our preliminary studies.[131] The method discussed in this paper addresses the following three limitations:

Image quality: We present a novel machine-learning based approach for automated lobe segmentation that takes advantage of the unique characteristics of the FHFBCT image datasets, namely the large number of images and lack of sorting artifacts common with traditional 4DCT approaches.[76]

Learning the fuzzy boundaries: Peers have employed deep neural network (DNN) for segmentation of anatomical structures. A conventional DNN learning using convolutional neural networks has been investigated for lung segmentation. Such approaches have been observed to inaccurately identify lobe boundaries since the lobes are only separated by a fissure that can be as thin as 1 mm^3. We identify the problem to be that the learning process does not account for the fuzziness in the boundary. In this paper, we investigate a quorum-based cGAN approach for learning the lobe boundaries, which is detailed in the methods section below.

Learning Complexity: Conventional machine learning strategies involve a single convolutional DNN learning the segmentation process.[129] In addition, the learning process is not scalable because adding more datasets requires a learning process that guarantees optimal transfer learning. To address this, we present a novel quorum-based inferencing process. During the training process, we divided the FHFBCT 3D datasets into a set of 12 batches and instantiated CGAN learning for each of the batches independently. Inferencing was performed by a quorum of CGAN members given equal weighting factors. For computational purposes, we dedicated a multi-GPU computing setup. The final segmentation results for each lobe were the weighted averages of the results from the inferenced CGAN quorum member networks. This inferencing strategy also allows for a scalable training process, in which new CGAN generator networks can be trained and added to the quorum as new data is acquired.

5.2 Methods

In this paper, we present a machine learning-based approach for segmenting the lung lobes. While airways and vessels help indicate lobe boundaries, they are insufficient to segment lobes. Airways and vessels do not cross lobe boundaries but lobe boundaries are typically adjacent to parenchymal tissue where airways and vessels are too small to identify and segment. In our approach, a machine learning framework was employed that learned the lung lobe segmentations from semi-automatically segmented datasets to automatically segment lobes. To generate lobe segmentation training data, we used a semi-automated segmentation process using ridge surface image features and published shape models.[130] The voxel-by-voxel lobe association was designated as a label and the associated FHFBCT scan was used as source data for the learning process. The steps in the learning process are now described.

5.2.1 FHFBCT Acquisition Protocol

CT data was collected using a Siemens AS 64 scanner located in the UCLA Radiology Department. The scans were/ acquired using a conventional helical protocol, with a pitch of 1.5, rotation speed of 0.25s, for an effective 40 mAs. We scanned in alternating directions with an approximately 2s delay between successive scans and acquired 25 free breathing scan datasets. The free-breathing component of the scan protocol is based on the standard imaging protocol we use when acquiring and studying free-breathing patients and corresponds to a total effective lung dose of 14.4 mSv per imaging session [132] While such a protocol delivers more dose than a typical diagnostic CT, the proposed dose is consistent with other interventional imaging protocols. Rintoul, et al [133] recently showed that the effective dose (typically from CT and PET) for lung cancer diagnostic workups averages 15.1 mSv, 25.8 mSv, and 28.6 mSv for best supportive care, chemoradiotherapy, and surgical interventions, respectively.

5.2.2 Pre-processing for Lobe Segmentation Training

The proposed approach for machine learning based lobe segmentation relies on pre-learning data generation and image processing steps taken to prepare the image datasets. This process is schematically illustrated in Figure 5-1. A set of 12 patient datasets was used for training purposes in which each dataset consisted of 25 FHFBCT scans (totaling 300 3DCT scans). For each patient, an arbitrarily-selected reference scan was semi-automatically segmented using the Pulmonary Toolkit (PTK) software for Matlab.[130] The automated segmentation of the lung lobes by PTK utilized fissure identification and ridge selection, however the resulting segmentations were observed to be largely inaccurate. Figure 5-2a shows an example of a PTK automatic segmentation result. Therefore, we employed a semi-automatic approach, where we first generated an initial estimate of the segmentation using PTK's automatic segmentation tool and then manually corrected for errors on a slice-by-slice basis with segmentation editing tools. These corrections were reviewed by pulmonary experts and the segmentations were modified accordingly until clinically acceptable results were obtained. Figure 5-2b shows a manually corrected image.

The reference FHFBCT was registered to each of the 24 additional scans using the DEEDs registration algorithm.[134,135] The registration process was observed to be accurate within clinically acceptable levels for FHFBCT scans, with an average mean error of 1.15 ± 0.37 mm and 95th percentile error estimated at 2.47 ± 0.78 mm, as previously reported in Dou et al..[128] The resulting DVFs were applied to the reference lobe segmentation to acquire segmentations for each of the additional 24 geometries for each patient. The registration performance and deformed segmentation results were verified by experts. The acquisition of 25 lobe segmentations per patient enabled a supervised learning process. For each set of patient data, images from 25 FHFBCT scans and 25 lobe segmentations were resized to 256x256 and combined into individual large datasets

for training. The FHFBCT images were then concatenated with the corresponding lobe segmentation images and normalized to create 512x256 training images.

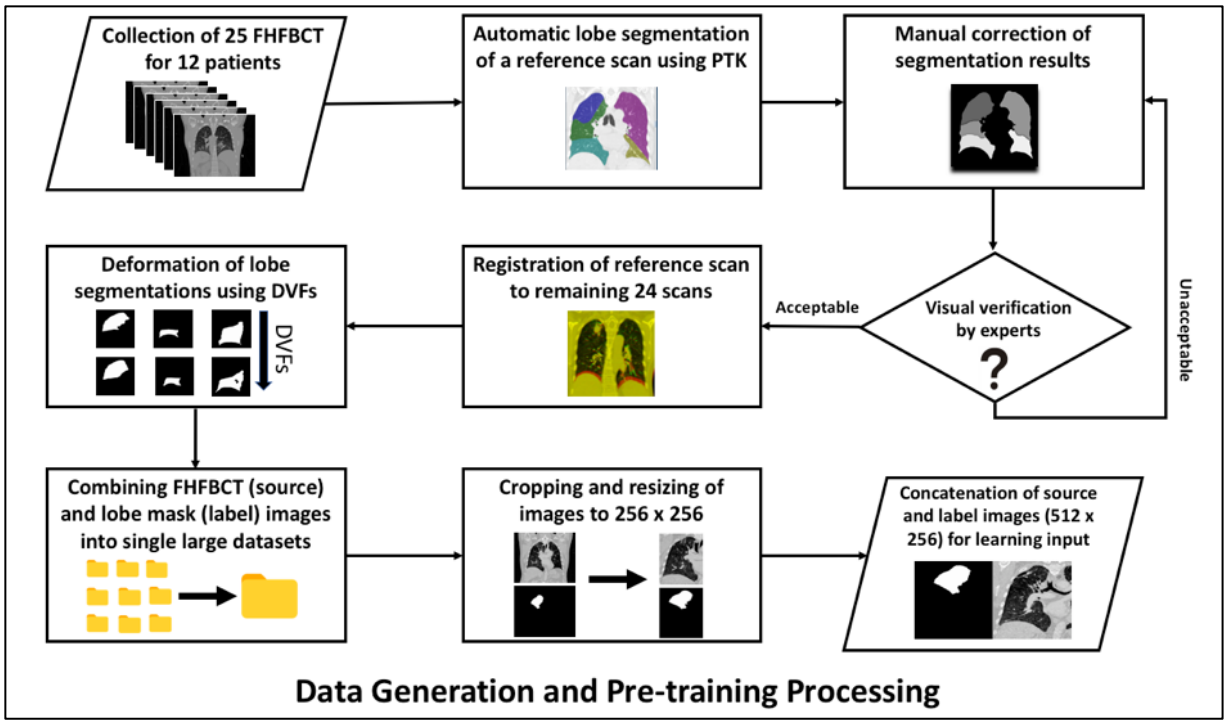

Figure 5-1: A schematic representation of the data generation and pre-processing steps involved in the lobe segmentation process

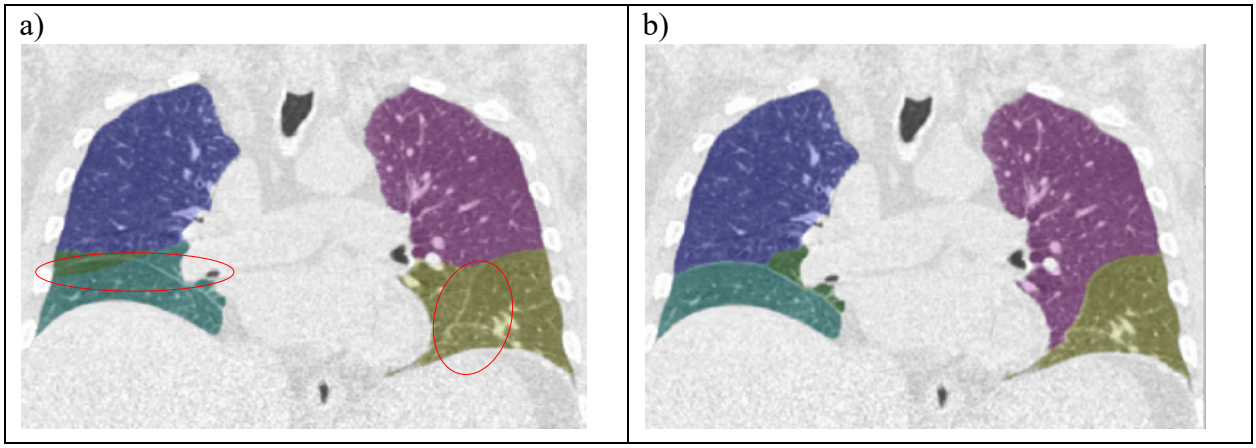

Figure 5-2: Segmentation results obtained from the state-of-the-art automatic lobe segmentation approach and after manual correction are shown in (a) and (b), respectively. Lobes are identified by different colors and errors are marked by red circles.

5.2.3 CGAN Network-based Lobe Segmentation

Figure 5-3 schematically represents the adversarial learning process. We implemented a CGAN network-based lobe segmentation, which we have shown to be effective in estimating lung elasticity using single CT scans.[136] The widely-cited Python implementation of the CGAN-based pix2pix algorithm was the basis for network construction.[137] The network consisted of two deep neural networks (each being a combination of convolutional and fully connected network layers) namely, generator and discriminator neural networks. A supervised learning process was used, where the generator network was trained to generate lobe segmentation results and was optimized using ground-truth lobe segmentations.

5.2.3.1 Generator Deep Neural Network

The generator network consisted of a five-layer neural network, in which the first three layers were convolutional neural networks and the final two layers were fully connected neural networks. The generator network training was initiated with random weights and biases, subsequently optimized using the training data. The accuracy of the generator network was iteratively monitored and optimized by inferring a sample output image from the discriminator.

5.2.3.2 Discriminator Deep Neural Network

The discriminator network consisted of a 4-layer neural network, in which the first two layers were convolutional neural networks and the last 2 layers were fully connected neural networks. To train the discriminator, the input values came from the generator neural network and ground-truth segmentation results. The discriminator network was refined by updating assigned weights and biases of the hidden and output layers.[138] The loss function calculated the error

between the output of the output layer results and the ground-truth lobe segmentations. A quadratic cost was implemented as the loss function in this study.

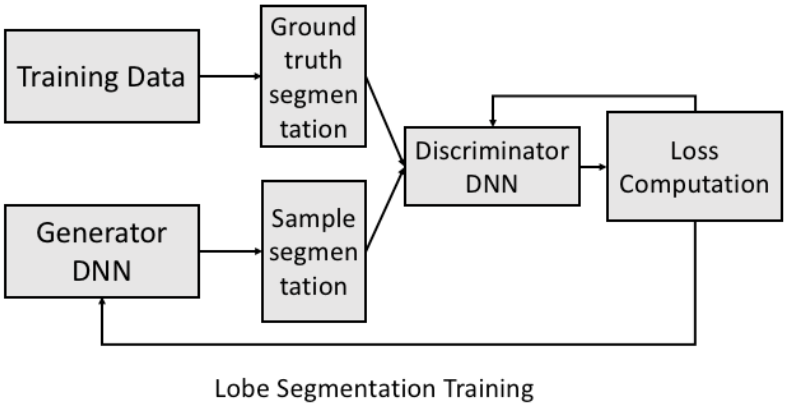

Figure 5-3: Schematic representation of steps involved in the lobe segmentation training process

5.2.4 Quorum-based DNN Inferencing

Figure 5-4 schematically illustrates the quorum-based inferencing process. The quorum consisted of a scalable number of generator DNNs each trained using a set of 25 FHFBCT scans and corresponding lobe segmentations. In our implementation, a set of 12 generator DNNs served as quorum members. During inferencing, the input FHFBCT image was segmented for the individual lobes by each of the 12 generator DNNs associated with that lobe, totaling 60 DNN-based segmentations.

The results were then compiled for quorum analysis and segmentation generation and an accumulator array representing the empty segmentation voxel map was generated. For each voxel in the array and corresponding voxel in DNN segmentation results, we iteratively identified lobe voxels assigned by generator DNNs. If more than 50% of the DNN results agreed that a specific voxel in the image volume belongs to the lobe then the accumulator array value was set to 1 for that voxel, indicating that the segmentation for that voxel was approved. If not, the accumulator

was set to 0 indicating that the segmentation for that voxel was not approved. Voxel lobe assignments were therefore determined according to Equation 1 where each voxel x in binary image array T is assigned value 1 if a 50% agreement threshold of quorum-member outputs, U_i, is met and 0 if not met for the voxel.

$$T(x) = x = \frac{\sum_{i=1}^{12} U_i(x)}{12} = \begin{cases} 1, & x \geq 0.5 \\ 0, & x < 0.5 \end{cases} \tag{5-1}$$

The process was repeated for all image voxels and lobe segmentations to produce a weighted average lobe segmentation based on quorum member segmentation results. For real-time purposes, a GPU-based quorum framework allowed voxels to be processed in a parallelized manner.

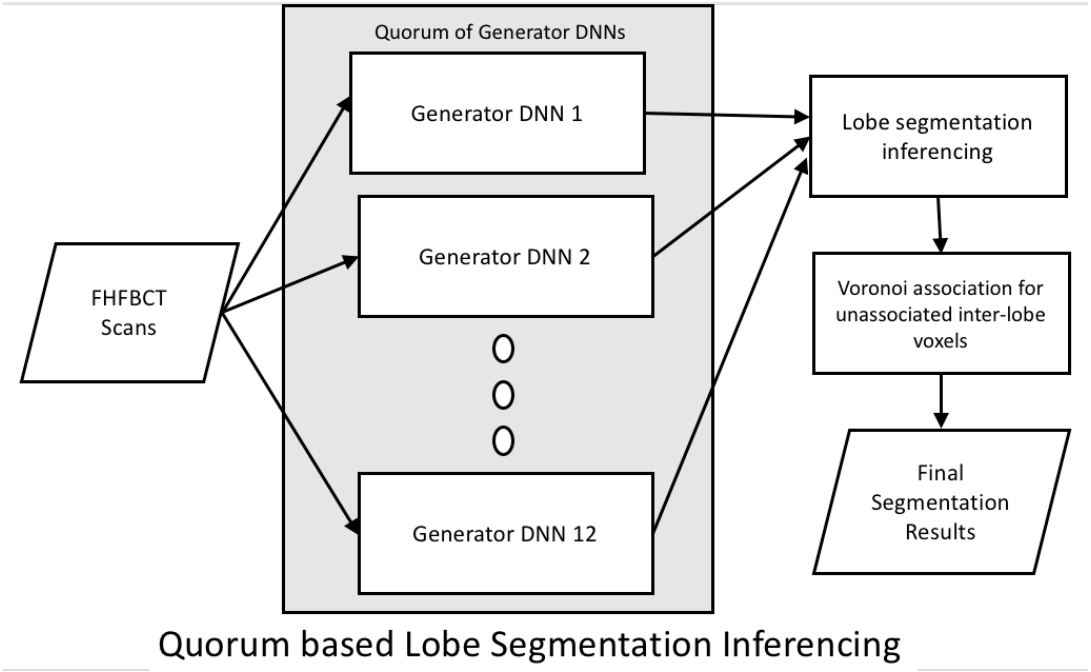

Figure 5-4: Schematic representation of quorum-based inferencing process

5.2.5 Association for Unselected Voxels

We anticipated a subset of lung voxels, identified during pre-processing via thresholding, to be unassigned to any of the lobes during the DNN inferencing. Additionally, voxels assigned to two or more lobes during quorum inferencing were also considered unassigned. Unassigned lung voxels were subsequently associated with a lobe using a nearest-neighbor algorithm which located the lung voxel at the smallest distance and determined that voxel's quorum-based lobe assignment. The lobe assignment of the identified nearest neighbor was then given to the unassigned voxel. Let *I* represent one such unassigned voxel at location (i,j,k). Let **A** be a n-by-n binary matrix representing a given lung volume. Euclidean distances from the unassigned voxel to each lung-containing voxel in **A** were then calculated and the location of the voxel found at the smallest distance, and its associated lobe assignment, were recorded by indexing the lobe-assignment matrix. Specifically, we computed the distance *d* between voxel *X* with coordinates (i_1,j_1,k_1) and each voxel *Y* in **A** with coordinates (i_2,j_2,k_2), according to the following equation.

$$d(X,Y) = \sqrt{(i_2 - i_1)^2 + (j_2 - j_1)^2 + (k_2 - k_1)^2} \tag{5-2}$$

The unassigned voxel *X* was then attributed to the lobe containing point *Y* in **A** with the smallest distance to *X*. At this stage, all lung voxels were assigned to a lobe and the segmentations were considered complete.

5.2.6 Image Similarity Metrics

To evaluate the accuracy of the generated lobe segmentation datasets, several image similarity metrics were utilized. Structural Similarity Index (SSIM), unlike the standard mean square error, considers local patterns of pixel intensities to provide a similarity assessment that considers the loss of structural information between images.[121] The equation for SSIM is as

follows, where x and y are the images being compared, μ_x and μ_y are average pixel values of x and y, σ_{xy} is the covariance of x and y, σ_x and σ_y are the variance of x and y, and C_1 and C_2 are constants introduced to avoid instability:

$$SSIM\ (x,y) = \frac{(2\mu_x\mu_y + C_1)(2\sigma_{xy} + C_2)}{(\mu_x^2 + \mu_y^2 + C_1)(\sigma_x^2 + \sigma_y^2 + C_2)} \tag{5-3}$$

The second similarity metric used to compare segmentation images was a fast-calculation Normalized Cross-Correlation Coefficient (NCC) intended for template matching. This method calculates correlation for multiple basis functions occurring in an image and produces a single weighted-sum correlation value to another. The formulation of this equation is described in Equation 4, where s is the sum table of the image function, *x* and *y* are image voxel position, *u* and *v* are the template voxel position, f is the intensity of the image, $\bar{f}$ is the mean intensity, and $\bar{t}$ is the template function:

$$\tilde{\gamma}(u,v) = \frac{\sum_{i=1}^{k} k_i \left(s\left(x_u^i+u, y_u^i+v\right) - s\left(x_u^i+u, y_l^i+v-1\right) - s\left(x_l^i+u-1, y_u^i+v\right) + s\left(x_l^i+u-1, y_l^i+v-1\right)\right)}{\sqrt{\sum_{x,y}(f(x,y)-\bar{f}_{u,v})^2 \sum_{x,y}(t(x-u,y-v)-\bar{t})^2}} \tag{5-4}$$

Dice Similarity Coefficient (DICE) was used to measure geometric correlation between segmentations [139]. The equation used in computing DICE between two images is shown in Equation 5, where V_1 and V_2 represent the images being compared:

$$DICE\ = \frac{2(V_1 \cap V_2)}{|V_1| + |V_2|} \tag{5-5}$$

5.2.7 Implementation and Computing Setup

The learning process was both computationally and time expensive with each patient- and lobe-specific DNN requiring a single GPU and 24 hours of runtime to complete a single instance of adversarial learning, thereby requiring 5 GPUs to run in parallel (120 hours of computation

time). With 12 patients for learning and 5 lobe-specific learning processes, 60 networks were trained on a server consisting of 6 machine setups holding a total of 42 GPUs (1440 hours of computing time). During inferencing, we enabled all 42 GPUs to load DNN models simultaneously, generate lobe segmentations, and perform necessary post-processing in < 1 minute per validation dataset.

5.3 Results

Results from a quantitative analysis of quorum-based DNN generated lobe segmentations showed an improvement in accuracy from the current state-of-the-art segmentation method. The average percentage of voxels unassigned or attributed to more than one lobe after quorum-inferencing, with a per voxel requirement of 50% agreement amongst quorum members, was 2.74% and 14.1% for the left and right lungs, respectively. In each of the ten test patient datasets, a performance comparison of PTK's automatic lobe segmentation and our quorum-based DNN inferencing lobe segmentation results displayed similar or improved values in all three of the evaluated similarity metrics. Table 5-1 shows these calculated values for each patient. The average SSIM across test patient datasets for PTK- and the quorum-generated lobe segmentations were 0.911 and 0.929, respectively. This signifies that the internal structures were optimally accurate during the segmentation process. Similarly, the average NCC was calculated to be 0.698 and 0.806 for PTK- and our quorum-generated segmentations, respectively. The average DICE coefficients for PTK- and quorum-generated segmentations were 0.696 and 0.814, respectively. These results demonstrate that an optimal automated lobe segmentation can be performed using a quorum-based DNN inferencing method.

	SSIM		NCC		DICE	
Patient	**PTK**	**Quorum**	**PTK**	**Quorum**	**PTK**	**Quorum**
1	0.820	0.903	0.628	0.789	0.674	0.806
2	0.900	0.935	0.707	0.836	0.713	0.848
3	0.894	0.957	0.561	0.873	0.537	0.875
4	0.920	0.935	0.747	0.850	0.745	0.856
5	0.904	0.952	0.668	0.837	0.662	0.836
6	0.941	0.942	0.835	0.816	0.838	0.824
7	0.915	0.847	0.465	0.547	0.468	0.559
8	0.932	0.951	0.679	0.785	0.675	0.782
9	0.963	0.931	0.916	0.877	0.926	0.884
10	0.916	0.933	0.769	0.849	0.725	0.874
Average	**0.911**	**0.929**	**0.698**	**0.806**	**0.696**	**0.814**

Table 5-1: Image similarity metric results comparing PTK-generated and quorum-based segmentation results to ground-truth segmentations for 10 test patients; Structural Similarity Index (SSIM), Normalized Cross-correlation coefficient (NCC) and DICE coefficient shown

Table 5-2 presents image similarity metrics calculated for each lung lobe of a single test patient. The average SSIM over the 5 lobes for PTK- and quorum-generated lobe segmentations were 0.894 and 0.957, respectively. These values show near perfect agreement in structural information between generated and ground-truth segmentations. Average NCC values for the 5 lobe segmentations were calculated to be 0.561 and 0.873 for PTK- and our quorum-generated segmentations, respectively. Finally, the average DICE coefficients calculated for PTK- and quorum-generated segmentations were 0.537 and 0.875, respectively. Specifically, DICE showed that for the middle right lobe (MRL), the accuracy of PTK was considerably low (0.322), but

greatly improved for our algorithm (0.827). Similar results were obtained for other lobes and in nearly all test patients, suggesting the fact that the individual lobes were accurately segmented.

	SSIM		NCC		DICE	
Lobes	**PTK**	**Quorum**	**PTK**	**Quorum**	**PTK**	**Quorum**
URL	0.919	0.960	0.645	0.948	0.620	0.958
MRL	0.886	0.955	0.320	0.822	0.322	0.827
LRL	0.933	0.957	0.787	0.892	0.776	0.890
ULL	0.860	0.953	0.550	0.952	0.508	0.961
LLL	0.872	0.960	0.504	0.749	0.457	0.740
Average	**0.894**	**0.957**	**0.561**	**0.873**	**0.537**	**0.875**

Table 5-2: Image similarity metric results comparing PTK-generated and quorum-based segmentation results to ground-truth segmentations for each lung lobe of a single test patient; SSIM, NCC, and DICE for upper right (URL), middle right (MRL), lower right (LRL), upper left (ULL), and lower left (LLL) lobes

	DICE Coefficients				
Quorum Member	**URL**	**MRL**	**LRL**	**ULL**	**LLL**
1	0.912	0.517	0.841	0.934	0.871
2	0.880	0.495	0.800	0.922	0.611
3	0.889	0.416	0.814	0.908	0.709
4	0.904	0.405	0.535	0.886	0.731
5	0.366	0.339	0.760	0.913	0.865
6	0.728	0.294	0.659	0.948	0.667

7	0.938	0.224	0.610	0.917	0.776
8	0.885	0.400	0.769	0.854	0.681
9	0.913	0.418	0.522	0.869	0.499
10	0.628	0.358	0.747	0.862	0.797
11	0.838	0.348	0.816	0.926	0.813
12	0.758	0.482	0.756	0.915	0.720
Average	**0.793**	**0.380**	**0.708**	**0.902**	**0.715**
Quorum Result	**0.946**	**0.562**	**0.881**	**0.965**	**0.830**

Table 5-3 DICE coefficients calculated between each of the 12 quorum member DNN results compared and the ground-truth lobe segmentations for a single test patient dataset; upper right (URL), middle right (MRL), lower right (LRL), upper left (ULL), and lower left (LLL) lobes

Table 5-3 shows the performance, measured by DICE similarity coefficient, of each of the 12 quorum-member networks for the 5 lung lobes of a single test patient prior to the quorum-inferencing process. As displayed in the bottom two rows of the table, the average DICE scores for the quorum member DNNs were 0.793, 0.380, 0.708, 0.902, and 0.715, while the quorum-inferenced results were 0.946, 0.562, 0.881, 0.965, and 0.830 for URL, MRL, LRL, ULL, and LLL, respectively. On average for the 5 lobes, the quorum-inferenced result showed an improvement over the average quorum member DICE score of 0.137.

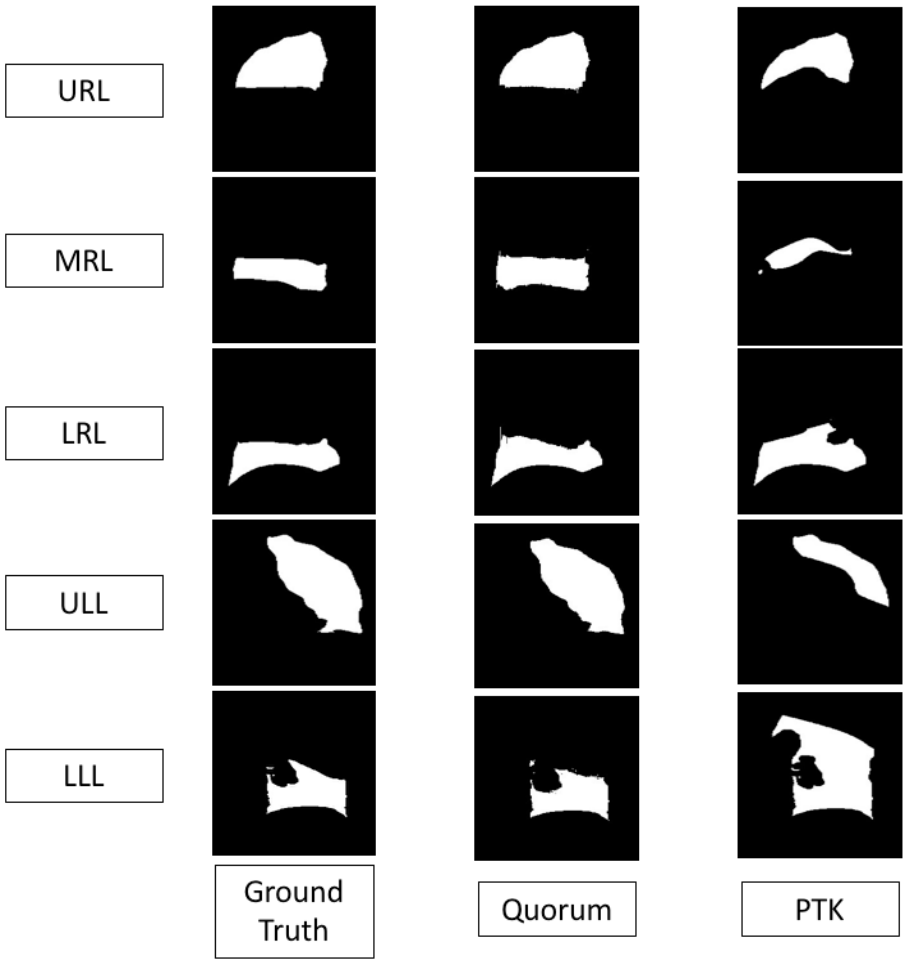

Figure 5-5: Representative slices for a single patient with rows specifying lung lobe and columns representing ground truth, quorum-based, and PTK-generated segmentations, from left to right, respectively

Figure 5-5 shows representative lobe-specific binary segmentation slices for ground-truth, quorum-based, and PTK-generated segmentation datasets. In this comparison, the quorum-based DNN-generated lobe segmentations more closely matched ground-truth segmentations than their PTK-generated counterparts. This was the trend amongst all test patients. The segmentations generated by our quorum method also produced more accurate fissure and lobe boundary identifications.

Figure 5-6 shows the overlay of ground-truth, quorum-generated, and PTK lobe segmentations with the associated FHBCT scans. It can be observed that the quorum-based DNN-generated segmentations demonstrated greater accuracy than the corresponding PTK automatically generated lobe segmentations when compared to the ground truth. Lobe boundaries and fissures can also be seen to be more accurately defined in the quorum-based DNN result. The improved accuracy in differentiation of lung lobes along boundaries and fissure identification is crucial to several clinical applications as discussed in previous sections.

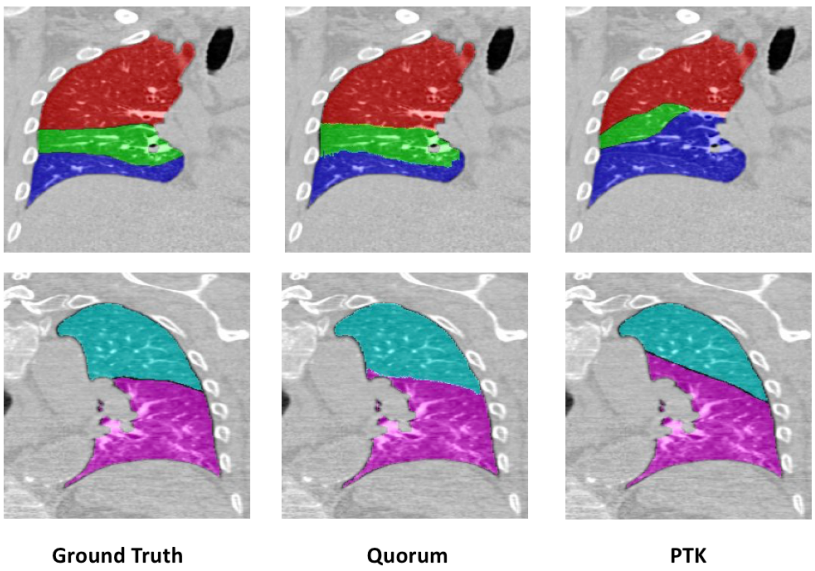

Figure 5-6: Lobe segmentation overlay with associated FHBCT right (top row) and left (bottom row) lungs for ground-truth, quorum-based, and PTK methods

5.5 Discussion and Conclusions

In this paper, we presented a novel approach for automatically segmenting the lung lobes using a machine learning-based process. An adversarial learning process was employed to obtain optimal learning accuracy. The key contribution of this work is the development and utilization of a quorum of adversarial learned generator DNNs, which allows for the segmentation of lung lobes in real time. Using an in-house GPU cluster, we observed the run-time to be near-real-time thereby

bolstering the potential for the algorithm to be implemented in a clinical setup. The proposed algorithm is also scalable as the quorum can be increased in size as more FHFBCT and lung segmentation ground-truth datasets are made available. We envision that this algorithm will be used for enabling improvements in lung DIR, lung biomechanics estimation, and the clinical use of novel protocols such as 5DCT protocol. In addition, for surgical intervention scenarios (e.g., lobectomy), the algorithm will produce a precise and automated characterization of the lobe boundaries and fissures.

The proposed algorithm uses FHFBCT scans for lobe segmentation as they are devoid of motion and sorting artifacts and any other source of potential motion blur. To enable conventional 3D/4D CT protocols to use the process, there is a need to re-run the learning process and re-build the quorum. Our future work would focus on investigating a transfer learning-based approach where the learned generator DNNs can be used to train on data from conventional 3D and 4DCT protocols.

The proposed algorithm implements a static weighted quorum for predicting the lobe segmentation results. We envision that a dynamic quorum where the weights automatically change based on image properties may be needed to further increase segmentation accuracy. Such a dynamic quorum would require a larger cohort of patients and their ground-truth segmentations. Future work would focus on the development of such a novel segmentation framework as well as an investigation into the performance of different sized quorums for optimal segmentation accuracy.

Our current algorithm performs with an accuracy at a clinically satisfactory level. Quantitative results, including the similarity metrics SSIM, NCC, and DICE, showed agreement between the quorum-based and the ground-truth manual lobe segmentations. Similarly, the

qualitative analysis showed the ability of the quorum-based segmentation results to accurately depict lung boundaries and fissures. However, it was observed that for slices along the lung anterior and posterior ends, the error was more dominant. This is because even with 12 quorum members there is far less data available that can represent the end slices. In our future work, we will utilize a biomechanical lung model to generate synthetic outer slices at different breathing phases and utilize them to bolster the training data and improve learning accuracy. We envision that this strategy will ultimately improve overall segmentation accuracy.

The setup in this study employs a set of 60 generator DNNs (12 for each lobe) for segmenting the lung lobes. Running such a large cohort of DNNs is a complex task. Our current implementation utilizes an in-house GPU cluster to enable near real-time segmentation. Our future work would investigate the task of designing generator DNNs that can be efficiently loaded and executed on single GPUs to achieve lower computational requirements.

CHAPTER 6: A quantitative prediction of the post-operative lobectomy lung physiology using a GPU-based linear elastic lung biomechanics model and a conditional generative adversarial learning approach

A version of this chapter has been published as a conference proceeding: SPIE Medical Imaging, Vol. 11598, 2021. doi: 10.1117/12.2582271

6.1 Introduction

Lobectomy is a common surgical approach for treating early stage non-small cell lung cancer (NSCLC).[29,30] Recent studies have confirmed that lobectomy remains the standard of care and consistently resulted in better outcomes than proposed alternatives.[31,140] Removal of a lung lobe may result in the reduction of pulmonary function and capacity for the patient, so lung surgeons routinely screen patients to evaluate the risk of postoperative pulmonary complications (PPC).[32] Advances in surgical techniques (minimally invasive procedures and sub-lobar resections) and perioperative care with improved outcomes are challenging historical criteria on how patients are evaluated for operative candidacy.[33] For current lobectomy strategies, patient selection is critical to ensure clinically acceptable PPC and mortality rates.[34]

Pre-operative pulmonary function is used to assess surgical candidacy and is conventionally quantified using spirometry measurements. While multiple factors are measured during these tests, specific measurements that correlate with patient eligibility for surgery include Forced Vital Capacity (FVC) and Forced Expiratory Volume at 1 second (FEV1).[141] These two measurements are also utilized in another key metric defined as the ratio FEV1/FVC. Although spirometry-based predictions alone may have limitations when determining patient eligibility, current state-of-the-art clinical decision guidelines (CDG) are based on these measurements.[142]

The presence of lung comorbidities leads to compromised pre-operative lung function and poor, unreliable, post-operative predictions. For example, 80% of lung cancer patients may have

some form of COPD, which negatively impacts their pulmonary function.[143] Even with this high COPD rate, approximately 60% of patients remain eligible for lobectomy surgery based on PFT measurements and PPC estimates. Improved postoperative pulmonary function predictions might identify the high-risk patients in advance, thus improving the lobectomy mortality rate. At the other end of the spectrum, approximately 10% of patients have sufficiently poor pulmonary function to be considered unsuitable for lobectomy. Most relevant to this application, 30% of early-stage NSCLC patients have marginal lung function and are referred to as high-risk patients.[144] Little guidance is available to clinicians to determine if these high-risk patients are suitable lobectomy candidates. A quantitative technique is needed to pre-operatively predict post-surgical pulmonary function, which could ultimately result in (a) a subset of currently deemed high-risk patients being eligible for lobectomy and (b) an overall reduction in mortality rates due to improved patient selection.

Biomechanical models of human anatomy have been developed for applications ranging from computer animation to CT image registration. Such approaches have been used by peers to model complex motion of the face, neck, torso, hand, leg, and lungs.[93,145-150] Previous efforts toward developing high-resolution biomechanical models has focused on the anatomical sites of head/neck and the lungs.[92,93] Relevant to this work, we have developed physics-based lung models in a clinical context to simulate the onset of open and closed pneumothorax and predict radiotherapy treatment efficacy.[93,151]

4DCT and 5DCT imaging protocols provide the necessary imaging data for lung biomechanical model development and assembly.[93] Although commercial 4DCT systems have been employed by others to study lung motion for radiotherapy treatment planning, little work has been done to investigate the use of data acquired from model-based CT approaches for lobectomy

simulation. This could be due to irregular patient breathing and airway obstructions that cause dynamic changes in the regional ventilation.

Early lung elasticity measurements were based on the measurement of biomechanical properties of excised tissue, which were found to be patient, location, and disease specific. Therefore, an accurate characterization of these properties may be acquired through non-invasive in-vivo methods at voxel level. Biomechanical property estimations are obtained using an iterative inverse deformation method and physics-based biomechanical models with 3D in vivo images as input. Estimated elasticity distributions are updated until a set of convergence criteria with the DIR-defined deformations are met.[152] Successful elasticity measurements were performed using 4DCT image datasets acquired for lung and breast cancer patients.[93,153-155] Based on this extensive research, we envision that the implementation of biomechanical elastic models could serve as a tool for the quantitative prediction of PPC in the areas of both lung cancer and COPD. In this paper, we propose and evaluate the feasibility of a framework that considers conventional breath-hold CT images and pre-operative PFTs to predict post-operative lung function.

The rest of the chapter is organized as follows: Section 6.2 presents the materials and methods for the biomechanical model development and the underlying machine learning algorithms. Section 6.3 presents the results for the lobectomy simulation and the post-operative prediction. Section 6.4 and 6.5 conclude the chapter with a discussion on the direction of future work and a brief conclusion, respectively.

6.2 Materials and Methods

6.2.1 Workflow

In this paper, we present a novel framework for a biomechanically guided prediction of post-operative pulmonary lung function. Figure 6-1 schematically represents the proposed

framework. The approach takes breath-hold CT images and spirometry results acquired pre-operatively as input. Conventionally, the model building process requires 4D imaging, which are not typically acquired in the lobectomy imaging protocol. To this end, we developed a machine learning framework for enabling the model assembly (Section 6.2.2). Specifically, we developed a cGAN learning process to perform lobar segmentation of the lungs (Section 6.2.3), estimate underlying lung tissue elasticity (Section 6.2.4), and predict the boundary condition changes between pre- and post-operative lung anatomies (Section 6.2.5). These machine learning components provide the required parameters for the model assembly process. A high-resolution finite element biomechanical model is then assembled (Section 6.2.6). The removal of the identified lobe is then biomechanically simulated and the remaining lung anatomy is allowed to deform. Finally, the predicted post-operative lung boundaries are applied to estimate the post-operative patient lung anatomy. This estimated anatomy was then taken as input to biomechanical simulations of PFTs used clinically to measure lung function. Specifically, FEV1 and FEV1/FVC maneuvers were simulated and resulting values measured using the post-operative lung model.

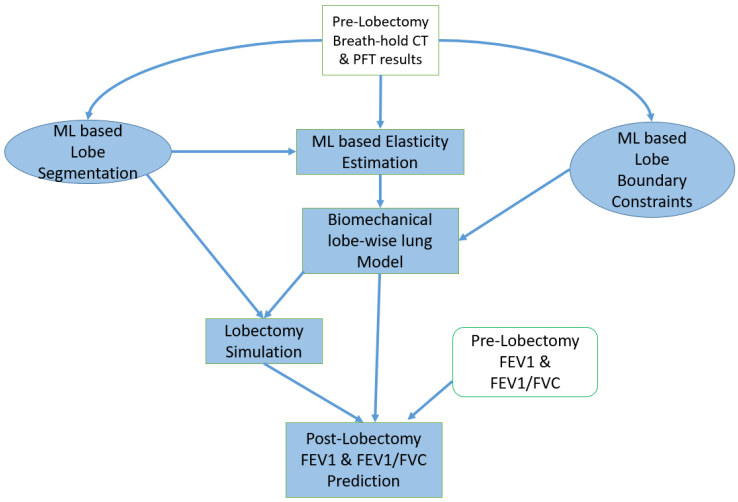

Figure 6-1: A schematic diagram of the proposed workflow for quantitative model guided post-lobectomy predictions of lung function.

6.2.2 Conditional Generative Adversarial Networks

To assemble a physiologically accurate biomechanical model, we first needed lung lobe segmentation, elasticity estimation, and estimated post-operative boundary conditions. These were obtained using a cGAN based learning process due to its demonstrated accuracy when previously applied to image-translation problems.[136] The cGAN consisted of generator and discriminator neural networks. The generator network was tasked with producing lobe segmentations from CT scans and consisted of a 12-layer neural network, of which the first 9 layers were convolutional neural networks and the last 3 layers were regular fully connected neural networks. Generator network training was initiated with random weights and biases, which were subsequently optimized during model training. Each layer of the neural network functions as follows: The neurons of the hidden layer take the data from each neuron of the input layer, apply a linear matrix multiplication with weighting factors, add a bias, and then apply a non-linear activation function. Using a non-linear activation function is important because a composition of linear functions remains a linear function, so the network abstraction would be otherwise limited no matter its depth. We employed a sigmoid function because it is essentially a smoothed step function and there is no loss of data for negative values, which is typical of other activation functions.[156,157]

The discriminator network consisted of a 5-layer neural network of which the first 2 layers were convolutional neural networks and the last 2 layers were regular fully connected neural networks. The accuracy of the generator network was iteratively monitored and optimized by inferring an output from the discriminator. The inputs to the discriminator include pseudo-label images from the generator and the ground truth labels. To compute generator accuracy, the inputs were sent through hidden and output layers. The result of the output layer was then evaluated according to a loss function, an accuracy function, and the training algorithm. The loss function was applied during training to calculate the error between the output of the feed-forward neural

network segmentation and the ground truth segmentation.[138] The discriminator network was continuously refined during model updating the weights and biases of hidden and output layers.

6.2.3 Lung lobe segmentation

In this section, we present a machine learning-based approach for segmenting the lobes of the lung. While airways and vessels help to identify lobe boundaries, they are insufficient to accurately segment the lobes on their own. Lobe boundaries are typically adjacent to parenchymal tissue, where minor airways and vessels can be difficult to visualize and segment due to their small size and resolution of the CT images. In our approach, a cGAN machine learning framework was employed to learn lung lobe segmentation from semi-automatically generated binary lobe masks. The semi-automated process used to perform lobe segmentation and obtain ground-truth lobe masks utilized ridge surface image features and published shape models to perform segmentation.[130] Voxel-by-voxel lobe associations were considered label images and associated breath-hold CT scans served as the source data for the learning process.

The steps in automatic lobe segmentation process are as follows. To prepare training data for the supervised training process, lung lobes were manually segmented. The training process was performed with a GPU cluster computing setup. During model inferencing, the generator network predicted lobe masks from breath-hold CT images of lobectomy patients in near real-time.

6.2.4 Lung elasticity estimation

In this section, we present a machine learning-based method that predicted the three-dimensional (3D) lung tissue elasticity distribution for a given end-expiration 3DCT. Current approaches for characterizing lung tissue elasticity require four-dimensional (4D) lung motion as an input. Since 4DCT imaging is only widely used in a radiotherapy treatment setup, there is a

need to predict elasticity distributions in the absence of 4D imaging for feasibility in lobectomy and other interventional lung procedures.

To predict the lung tissue elasticity from an end-expiration 3DCT a deep neural network was implemented. This approach to image-to-image translation is previously discussed in Santhanam et al. and for brevity, we now present the method. For training and validation purposes, five-dimensional CT (5DCT) datasets and a finite element biomechanical lung model were used in a CT-based elastography approach to generate training data.[136] The 5DCT model was first used to obtain end-expiration lung geometry, which was taken as source geometry to the biomechanical model, as well as end-inspiration geometry. The deformation vector field (DVF) pointing from end-expiration to end-inhalation was computed by deformably registering the two 5DCT-generated datasets and taken as an additional input to solve for the lung tissue elasticity. An inverse elasticity estimation process was then performed, in which we iteratively solved for the lung elasticity distribution until convergence criteria assessing model reproduction of ground-truth deformation vector field were met. The machine learning process used a similar cGAN architecture that learned the lung tissue elasticity in a supervised manner. The biomechanically estimated tissue elasticity paired with the end-exhalation CT was taken as input for the model training step. The trained cGAN generated the elasticity from a given breath-hold CT image.

6.2.5 Post-operative boundary conditions

For biomechanical modeling of lung deformations, it is necessary to characterize the lung boundary conditions, which are defined by rib cage and diaphragm positions. It is also important to know the change in boundary conditions resulting from the lobe removal itself. The diaphragm is compressed superiorly by the lung volume and inferiorly by the liver. Since the lung has lesser volume, post-lobectomy, an imbalance in the internal pressures occurs, which may be measured

as a function of the air volume in the removed lobe. To model the change in boundary conditions, we used a cGAN approach. A set of 10 lobectomy patient datasets were retrospectively studied for this purpose. The ipsilateral lung was segmented in both pre- and post-operative images and deformably registered to one another. This process resulted in a deformation vector field that characterized the change in ribcage and diaphragm position at the start of the inhalation from pre- to post-operative anatomy. This cGAN model was trained to predict the DVF associated with the boundary of the ipsilateral lung of each lobectomy patient. Along with the resulting lobe masks from lobe segmentation and elasticity distribution prediction, the predicted lung boundary DVF describing the deformation from pre- to post-operative anatomy are integrated with the biomechanical model.

6.2.6 Biomechanical model assembly

We formulated the elasticity parameter using a generalized Ogden material model, which defines a strain energy, *W*, in terms of principal stretches, λ_i, and a shear modulus, μ:

$$W = \sum_{p=1}^{N} \frac{\mu_p}{\alpha_p}\left(\lambda_1^{\alpha_p} + \lambda_2^{\alpha_p} + \lambda_3^{\alpha_p} - 3\right); where\ 2\mu = \sum_{p=1}^{N} \mu_p \alpha_p \quad (6\text{-}1)$$

where α_p is the hyperelastic model power term for parameter *p* of *N* parameters.[158] The principal stretches were determined by solving for the image deformation tensor field eigenvectors. The principal Cauchy stresses, σ_i, were determined from the 2nd Piola-Kirchoff stress tensor, which itself was derived from the partial derivative of the strain energy *W* with respect to the principal stretches.

$$\sigma_i = \lambda_i \tau_i = 2\lambda_i \frac{\partial W}{\partial \lambda_i} = \sum_{p=1}^{N} \mu_p \lambda_i^{\alpha_p} \quad (6\text{-}2)$$

The internal force vectors were computed from the principal Cauchy stress at each element, enabling updates to individual velocity, assuming near-linearity for small incremental position changes. In order to maintain performance at interactive speeds, we implemented a multi-GPU

framework using an in-house compute cluster we have previously employed for real-time calculations.[158,159 160]

Equations 6-1 and 6-2 represent traditional approaches to biomechanical modeling, using image data acquired at two different timepoints or physiologic states. Therefore, we modified the approach to solving these equations by applying tidal volume as an additional boundary condition by equating the sum of deformation-field Jacobians to the measured tidal volume change (ΔV) as

$$\sum(J - 1) = \Delta V/V \tag{6-3}$$

Lobe Removal: The physiological changes associated with the removal of a lung lobe were simulated with the flow-structure interaction model using a two-step iterative approach. In the first step, the lobe resection was computed as a finite volume reduction process with its surrounding lobes and boundary conditions (e.g. ribcage and diaphragm) providing a rigid-body constraint.[92] In the volume reduction process, we represented the lobe resection by reducing the resected lobe volume to zero through a defined number of infinitesimal changes to the length of element connections. For a given change in the resected lobe volume, we decreased the rest length of each connection between the lobes' finite elements. Once target volume is achieved, the reduced lobe is treated as a rigid body constraint and the remaining residual lung anatomy surrounding the resected lobe was allowed to deform according to resulting internal corrective forces. The two-step iterative process was continued until the entire residual lobe and the resected lobe deformations converged with predicted boundary condition changes.

The finite element internal corrective forces were calculated as a summation of tensile spring force, shear spring force, and a dashpot damping force. At rest state, elastic internal corrective forces were set to 0. Deforming the model's finite elements led to non-zero internal

corrective forces. The calculation of the internal corrective forces began by computing the tensile spring force, shear spring force, and dashpot damping force as discussed by Neylon et al.[92] The internal corrective force on each voxel was then computed by summing these forces over each neighboring voxel connection. Finally, the new positions and velocities for each finite element were updated using implicit backward Euler integration. The new positions were then used to compute the positions of the resected and residual lobes.

6.3 Results

We first demonstrate our approach to segment the lung lobes from breath hold CT scans using a machine learning framework. Figure 6-2a presents the initial results obtained from our approach. For comparison purposes, we employed a semi-automatic approach, Pulmonary Toolkit.[130,131] The neural network was trained using 7 breath-hold CT-derived lobe segmentations and evaluated using 3 test breath-hold CTs. Figure 6-2b shows that segmentation errors in the lower lobe that occurred during the semi-automatic segmentation were avoided by the deep neural network. A direct comparison with the ground truth data showed that the deep learning approach estimated the lobe segmentation with a mean prediction error of 0.8±0.4 mm, as compared against the shape models that had a mean prediction error of 1.3±0.7 mm. In addition, the lobe segmentations matched the ground-truth segmentations with MI, SSI, and NCC values of 1.77, 0.89, and 0.94, respectively. These results demonstrate that for lobectomy patients, a machine learning lobe segmentation can be a useful and time-saving tool for the biomechanical model building process.

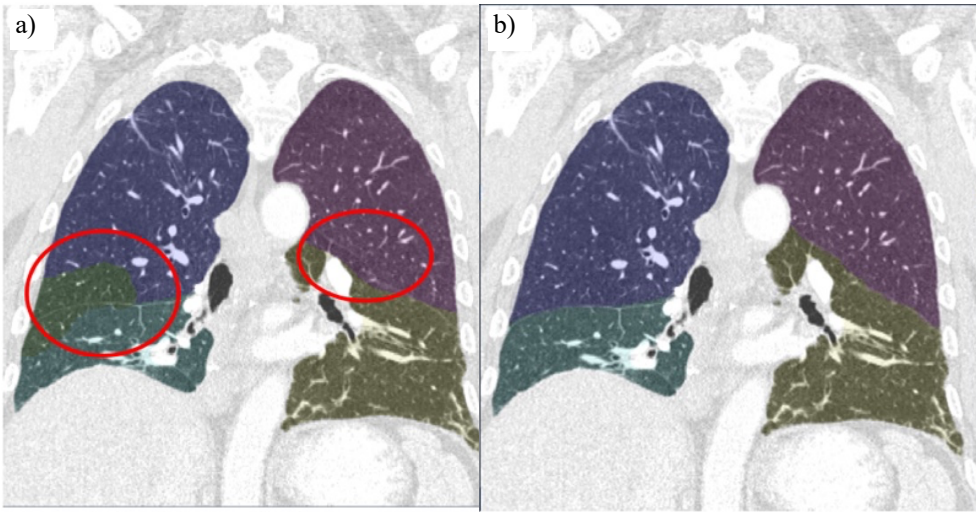

Figure 6-2: Segmentation results obtained from the state-of-the-art automatic lobe segmentation approach Doel et al [130] approach and our approach is shown in (a) and (b), respectively. The lobes are identified by different colors. Errors in the current segmentation are shown in circles

Figure 6-3 presents the simulation results using the biomechanical framework. Figure 6-3a shows the 3 right lung lobes, with color-coded elements reflecting lobe assignment. In this simulation the middle lobe was removed. Figure 6-3b, c, and d show stress maps associated with the lobe removal process. As the middle lobe volume decreases, the stress associated with the lobe contraction is shown in a color-coded manner from yellow (low) to red (high). The role of the biomechanical model is in properly simulating the forces exerted by the reduced lobe on the residual lobes. The stress associated with the elongation process is shown in light blue (low) to dark blue (high). The regions of the lung that are unaffected are color-coded in green. Figure 6-4 presents the simulation results using the biomechanical framework for a lower lobe removal. Figure 6-4a shows the lung anatomy before the lobe removal and Figure 6-4b shows the lung anatomy after the lower lobe removal. These simulations demonstrate that the lobe removal or reduction procedure may be biomechanically modeled.

We employed retrospective pre-operative and post-operative clinical breath-hold CT scans for validating the lobe removal process. Figure 6-5 shows an example of lower lobe removal simulation from the perspective of the biomechanical model. The model elements are again color coded to represent their assigned anatomy. Figure 6-5a shows the pre-operative anatomy and Figure 6-5b shows the post-operative anatomy. Figure 6-5c shows our post-lobectomy simulation results. Arrows identify two corresponding vessel bifurcations, indicating that the post-surgical scan and lobe removal simulations reliably estimated their relative geometry. To provide a view from within the lung volume, the pre- and postoperative CT anatomy are shown in Figure 6-6. Figure 6-6a and 6-6b show the pre-operative and post-operative CT images, respectively. Figure 6-6c shows our simulated post-lobe removal anatomy. The three images are aligned at an identified bifurcation landmark as identified by the red arrows. Our postsurgical simulation was sufficiently accurate to model the deformation of the lung tissue that caused the vessel to rotate into the image plane.

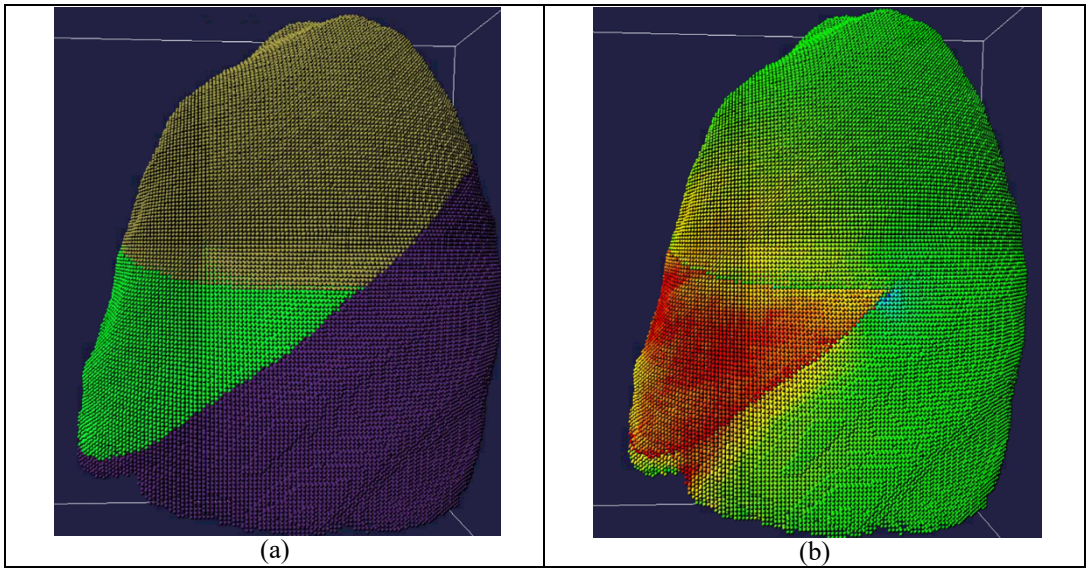
(a) (b)

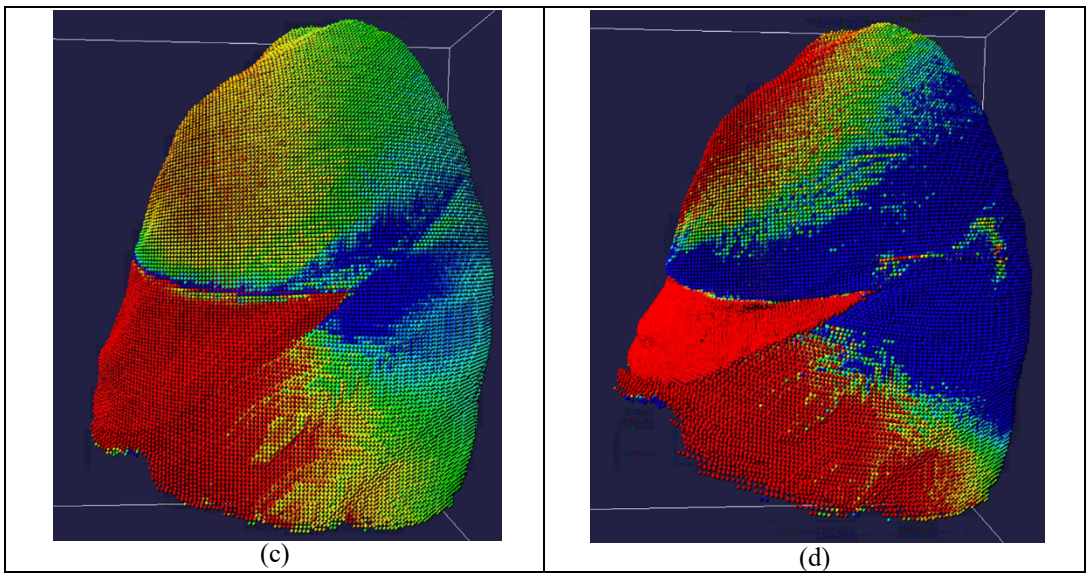

Figure 6-3: A novel lobe-wise lung biomechanical model is shown in (a). The biomechanical changes for lobe volume changes to 80%, 60% and 40% are as shown in (b), (c) and (d), respectively. The elements are color coded as yellow to red representing local contraction stress, green to blue representing elongation stress. The elements represented in green had no stress activity.

To demonstrate biomechanically guided predictions of post-operative lung function, we evaluated the impact of lobe removal on the proposed deep inhalation and forced expiration process. We assembled a biomechanical model, incorporating results from machine learning approaches for elasticity estimation, lobe segmentation and boundary conditions for each patient.[161] We simulated an end exhalation post-lobectomy CT scan using the lobe removal simulated process and compared against the actual end exhalation scan.

We generated two CT scans for pre- and post-lobectomy geometries: at deep inhalation and residual volume. The deep inhalation volume was approximated as 170% of the end-inhalation volume, which was itself approximated as 116% of the end exhalation volume (the volume at which the CT scans were acquired), and the residual volume was approximated as 50% of the

exhalation volume as per West and Luke.[162] The phase-specific rib cage and diaphragm geometries (boundary conditions) were approximated by differentially expanding or contracting the rib cage and diaphragm to the requisite volumes.[163] This technique was used to generate the deep inhalation and residual volume boundary conditions and we applied our biomechanical simulation to expand the lungs into the deep inhalation geometry. We then simulated the forced expiration maneuver, which we determined would require 4s on average, by stopping the simulation after 1s.[163] We used the resulting simulated CT to represent the FEV1 lung geometry to measure its corresponding FEV1 value. We were then able to calculate the simulated FEV1/FVC and repeated this process with the simulated post-lobectomy end-exhalation CT scan, providing us with an estimated post-operative FEV1/FVC.

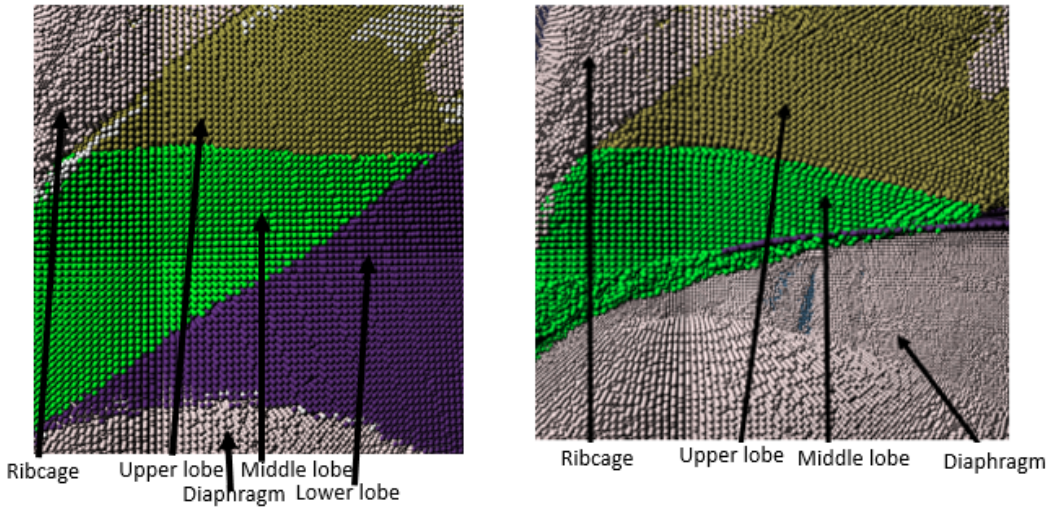

Figure 6-4: Simulation of a lower-lobe removal. These images reflect the biomechanical elements, and are color coded to reflect their anatomical assignments.

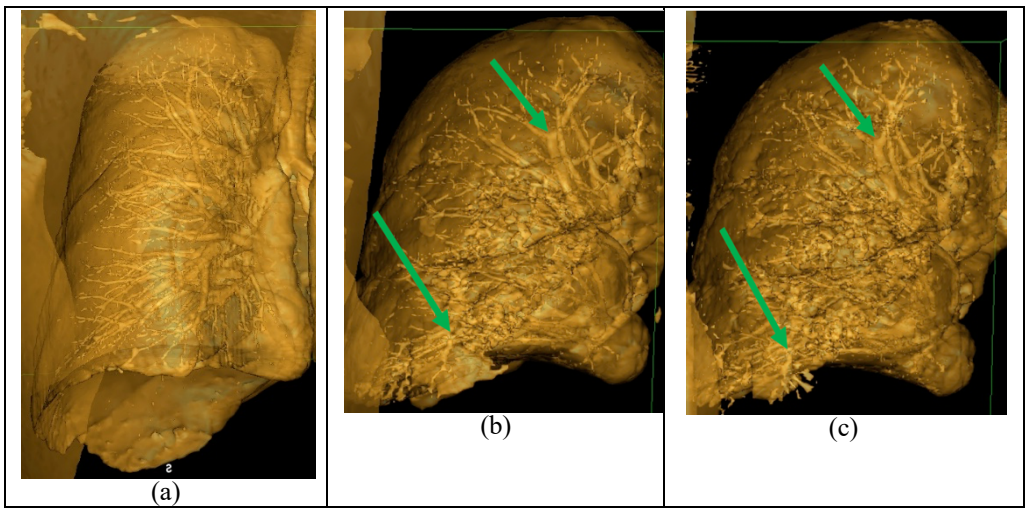

Figure 6-5: Volume rendering of the pre-lobectomy and the post-lobectomy CT anatomy is shown in (a) and (b), respectively. The simulated post-lobectomy anatomy is shown in (c). Arrows point to corresponding airway bifurcations.

Figure 6-7a and 6-7b show coronal slice overlays of the simulated pre-lobectomy and post-lobectomy lung anatomy, respectively, at deep inhalation and FEV1 shown in red and green, respectively. The patient's actual pre-lobectomy FEV1/FVC value was 70% and the estimated ratio of the pre-lobectomy to post-lobectomy FEV1/FVC values was 1.1, so the estimated post-lobectomy FEV1/FVC was determined to be 77%. The patient's actual post-lobectomy FEV1/FVC was 65%**.**

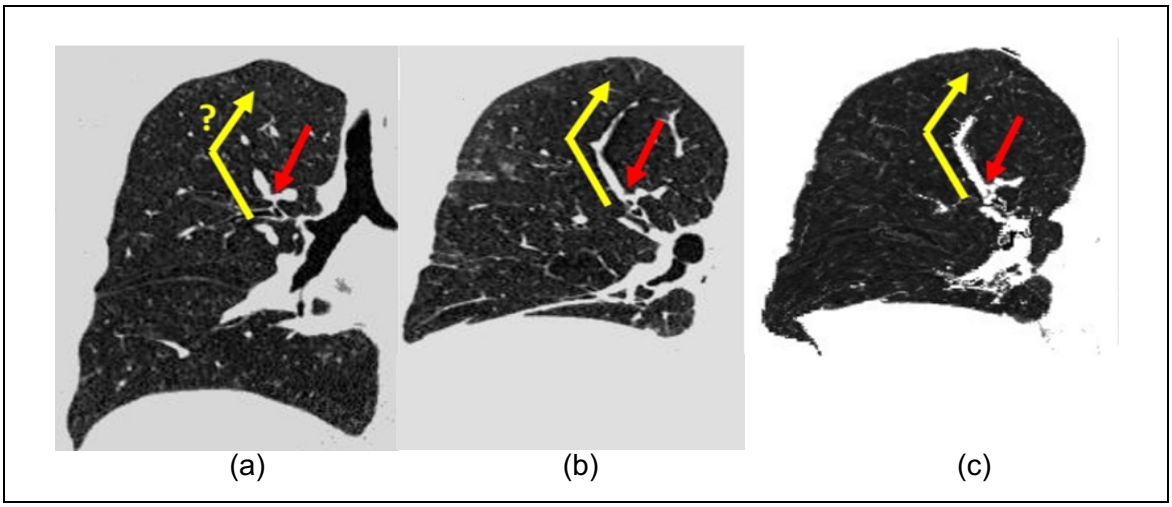

Figure 6-6: Comparison between simulated and actual lung geometry of a lobectomy patient (right lower lobe removed). a) CT of the pre-lobectomy patient. b) Actual post-lobectomy CT. c) CT after lobectomy simulation, including lobe removal and postoperative lung geometry changes. Red arrows identify common bifurcation. Yellow arrows indicate a vessel that lies in-plane in the postoperative images but is out of plane in the preoperative image.

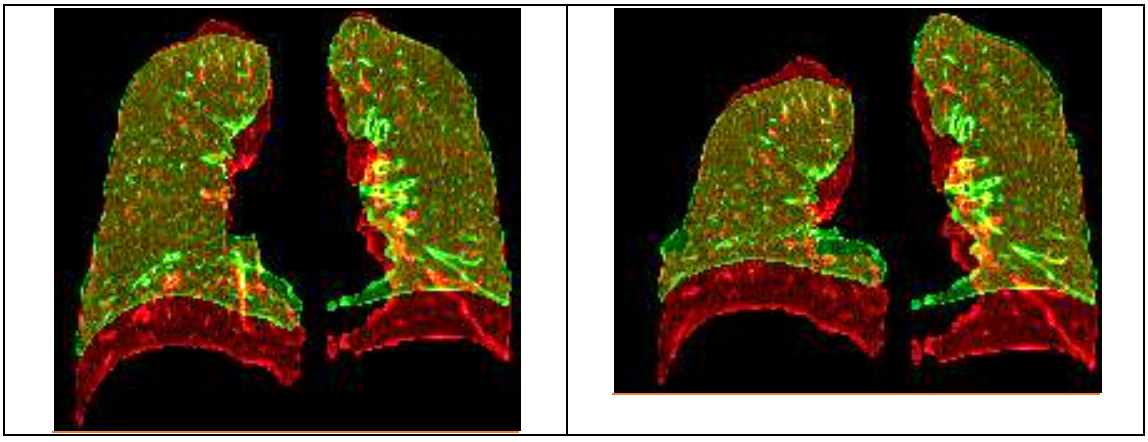

Figure 6-7: Results of simulating a forced expiration maneuver for pre-lobectomy and post-lobectomy CT scans (the text describes the reasons we analyzed lobectomy patients). (a) Pre-lobectomy deep inspiration (FVC) simulated CT (red) and FEV1 simulated CT (green). These scans are generated from a clinical breath-hold pre-lobectomy CT scan. (b) Post-lobectomy deep

inspiration (FVC) simulated CT (red) and FEV1 simulated CT (green). These scans are generated from a clinical breath-hold post-lobectomy CT scan for the same patient as (a).

6.4 Discussion

Lobe segmentation, elasticity distributions and boundary constraints were needed to assemble the biomechanical model. To this end, we employed a machine learning framework that facilitated learning these parameters from 5DCT datasets. Once assembled, the model was used to simulate lobe volume reductions and the associated changes in the pulmonary lung function. Post-operative predictions were then made to compute the lung FEV1 and FEV1/FVC results.

Many COPD patients cannot breath regularly, causing breathing-sorting artifacts in CT images, which significantly degrade biomechanical property estimation.[127] Since biomechanical model instantiation of diseased lung anatomy largely depends on artifact-free image data, in future work we may be able to avoid the typical challenges of commercial CT by employing our Fast-Helical Free-Breathing CT (FHFBCT) protocol for lung model development efforts.[123,128] FHFBCT has several advantages including that it is acquired during free breathing over a number of breathing cycles, has no sorting artifacts, and delivers relatively low dose. Using FHFBCT imaging and a 5DCT motion model for lobectomy patients could improve the biomechanical modeling process and the associated predictions. The multiple FHFBCT imaging protocol may also better quantify patient lung motion and ventilation. Future work will also focus on developing an alternative to conventional PFT measurements with more quantitative regional or lobe-wise functional measurements facilitated by the lung biomechanical model.

Diseased lungs are characterized not only by their pathologic biomechanical properties but also by airway narrowing and obstructions that restrict airflow into the lungs.[164] Xenon (Xe) gas diffusion imaging is one method used for measuring steady-state volumetric ventilation, but the

dynamic nature of airflow through the airways can only be crudely modeled with the technique. The limitations of Xe gas diffusion imaging for airflow modeling may be avoided by taking advantage of the high spatial resolution capabilities of the FHFBCT images. Efforts have been made to employ Computational Fluid Dynamics (CFD) coupled with patient-specific lung geometry and elasticity to quantitatively estimate lung airflow dynamics.

Accurate segmentation of the lung lobes from the FHFBCT scans is a critical task for our proposed workflow. Current state-of-the-art approaches use breath-hold CT as data and employ algorithms that identify vessels and lobe fissures and couple them with lobe shape models to identify the lobes of the lung. While these algorithms are automatic, they are known to produce inaccurate results because of variations in patient anatomy. Also, applying a semi-automatic segmentation for 12 CT scans (the number of scans we propose) would be impractical. A quorum-based machine learning approach was developed for this purpose. The method yielded an automatic segmentation approach that was observed to be more precise than a comparable state-of-art algorithm in preliminary studies.[131]

Although outside the scope of this paper, predicting postoperative pulmonary function beyond FEV1 and FEV1/FVC is an exciting aspect of developing a personalized postoperative flow-structure interaction predictive model. We believe that, as we further validate and optimize our approach, other quantitative descriptors of breathing function may prove to be more effective postoperative clinical respiratory status predictors than traditionally used PFTs.

We believe the proposed free breathing CT acquisition and PFT-prediction approach, integrated with a flow structure interaction model, has the potential to significantly improve pulmonary function testing for intervention planning. To our knowledge, this is the first proposed practical application of this technology for the purpose of aiding lobectomy surgeons in predicting

postoperative pulmonary function, requiring only non-invasive, patient-specific, imaging, and surrogate measurements. We hypothesize that by applying our free-breathing CT imaging protocol, preoperative PFT measurements, biomechanical modeling, and airflow dynamics models of lung tissue, we can quantitatively predict postoperative FEV1 and FEV1/FVC for each patient. We envision that such a PFT prediction could significantly improve the patient selection process. Future work will focus on a clinical study that includes a large cohort of lobectomy candidates to study prediction accuracy of post-operative lung function. A larger goal of these efforts is the development of a treatment planning system for lobectomy candidates that uses the biomechanically guided post-operative predictions to better select lobectomy candidates suitable for the procedure.

6.5 Conclusions

In this paper, a novel framework was proposed for assembling and employing a lobe-wise biomechanical lung model for the prediction of post-interventional lung function.

CHAPTER 7: Conclusion and Summary

7.1 Summary of Work

The research presented in this dissertation was performed with the goal of further investigating the role of biomechanical modeling and biomechanical property estimation in obtaining functional lung information for use within the radiotherapy domain. In addition, this work explored the possibilities of extending the developed biomechanical modeling techniques and machine learning applications to outcome prediction and patient evaluation undergoing lung intervention procedures. The works described and reported in this thesis utilized previously developed and newly improved techniques in biomechanical modeling and elastography, in combination with machine learning and unique datasets, to accomplish these goals.

We began in Chapter 2 with a systematic study of CT-based elastography model consistency using image datasets acquired over different ranges of each patient's breathing pattern. The results of this work showed that when we considered variations in patient breathing, both qualitative and quantitative measures reflected the high level of agreement in inter-patient elasticity estimation and overall consistency of the elastography method.

Next, a machine learning approach to elastography was developed and evaluated in Chapter 3 for the purpose of expediting the lengthy elastography process and allowing elasticity estimation from a single breath-hold CT scan. The trained cGAN model was shown to generate elasticity distributions with good agreement to their elastography model-generated counterparts. These results suggest that elastography could have potential utility at other points in the radiotherapy domain and for other applications in which model-based CT is not typically acquired.

We then investigated the feasibility of using large deformation images, acquired during forced breathing maneuvers, in the elastography process in Chapter 4. This work was motivated

by the observation that relatively small deformations occur in certain lung regions during free breathing, limiting the ability for accurate elasticity estimation in these voxels. Displacement convergence results showed a high level of agreement between DIR-generated and model-generated displacement values and confirmed the feasibility of performing elastography using breath-hold CT scans at RV and TLC. The work in Chapters 2-4 constituted the effort to further investigate and expand the uses of elastography within the radiotherapy context toward the larger goal of informing functional avoidance throughout treatment. However, each of these elastography applications have the potential to be extended to other research and clinical areas in future works.

The lobe-wise analysis of patient lung anatomy and biomechanical modeling of lobe-specific deformations requires an accurate lobar segmentation. Due to this typically being a lengthy manual process carried out by a physician, even in semi-automated workflows, we developed and tested a fully-automated quorum-based machine learning approach in Chapter 5. Our results showed that this approach performed lobar segmentation with improved accuracy while also providing significant time savings.[130]

In Chapter 6, the final work of this dissertation proposed a framework that took conventional imaging for lobectomy, predicted post-operative outcome, and calculated a quantitative measure of predicted post-operative lung function. The preliminary results established the feasibility of combining biomechanical modeling and property estimation methods for the purpose of post-procedural outcome and lung function prediction for various lung intervention candidates. This work served as an important proof-of-concept for what we envision may be a useful tool for experts in the field of function-preserving lung interventions. In addition, ongoing challenges that we face in the development and validation of such a tool were highlighted and future work will focus on addressing them.

7.2 Future Directions

7.2.1 Functional Avoidance Treatment Planning

There is currently a need for a CT-based lung functional biomarker for use in function-preserving treatment planning to reduce lung toxicity and the occurrence of RILI after radiation therapy. Elastography has been shown to provide regional functional information and may serve as a biomarker for indicating the presence of disease in COPD patients.[50,51] In this dissertation, we further validated and expanded the use of CT-based elastography methods and investigated machine learning approaches to reduce computation time to a clinically feasible timeframe. Therefore, we envision that the estimation of elasticity distributions could be useful in the identification of functional lung regions and informing of functional avoidance treatment planning efforts.

In future work, we intend to further investigate the incorporation of functional information obtained through elastography into a radiotherapy treatment planning workflow. Preliminary results of a proof-of-concept study by Hasse et al. found that for a small number of cases analyzed retrospectively, dosage to identified regions of functional lung could be reduced while maintaining acceptable target dose.[165] However, a larger validation study is needed to conclude the impact of elastography-derived functional lung information on the treatment planning workflow.

7.2.2 Free vs. Forced Breathing Elastography Comparison

A feasibility study investigating an elastography approach using large deformation datasets acquired at forced breathing, as opposed to free breathing, was presented in Chapter 4 of this dissertation. We hypothesize that elasticity values could be more accurately estimated for voxels that would otherwise have little or no displacement during free breathing. However, to fully test and validate this overarching hypothesis, a study comparing the elasticity estimation results

generated from free-breathing and forced-breathing images for the same patient cohort is needed. For this purpose, we propose the addition of RV and TLC breath-hold scan acquisition to the imaging protocol for thoracic radiotherapy patients. This would enable direct regional comparisons of elasticity values obtained from each method and their associated displacement convergence metrics, as described in Section 4.2.6.

7.2.3 Lobectomy Framework Validation and FSI Model

A proof-of-concept study was presented in Chapter 6 which investigated the ability to predict post-interventional lung geometry and PFT results using an approach that combined biomechanical modeling and machine learning applications. While initial results showed the feasibility of such an approach for a small number of datasets, a larger validation study is needed. The availability of additional lung intervention image datasets and associated functional outcome measurements is currently a limitation of this effort. Furthermore, the proposed framework in the Discussion section of Chapter 6 (Section 6.4) described a larger goal of incorporating a flow structure interaction model with the current approach for the development of biomechanically measured alternatives to traditional PFTs. In a separate work by Lauria et al., an automatic method for the mesh generation of airways for use in a computational fluid dynamics (CFD) model was developed.[166] We envision that the eventual integration of these two approaches could serve as an important treatment planning tool for pulmonologists and lobectomy surgeons.

7.2.4 Post-BLVR Elastography

Another related ongoing work involves the biomechanical modeling and property estimation for patients undergoing BLVR through placement of EBVs. As described in Section 4.2.1, the large deformation datasets consisted of RV and TLC images acquired pre-procedurally as part of the VENT clinical trial, in which patients underwent EBV treatment.[40,167] We have since

acquired corresponding post-interventional images for the same patient cohort. Figure 7-1a and 7-1c show examples of patient anatomy prior to undergoing BLVR and Figure 7-1b and 7-1d show the post-procedural anatomy, in which the endobronchial valves are circled in red. A current work in progress is performing elastography on post-BLVR datasets for comparison with the pre-interventional values documented in Chapter 4. Table 7-1 reports measured mean and maximum DIR displacement magnitudes, DIR and model-generated displacement differences, and estimated elasticity values for both pre- and post-BLVR datasets for a single patient. This analysis could provide quantitative regional information about patient lung function changes or improvements following a procedure. The results may also then be compared with post-procedural PFTs for validation.

a) 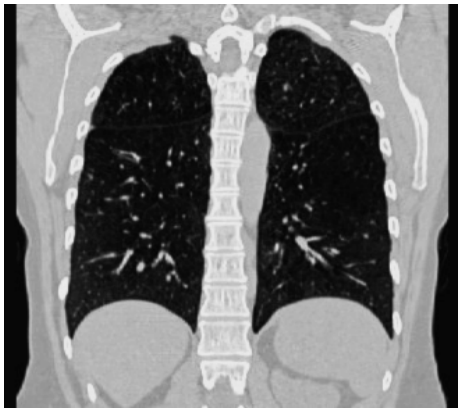	b) 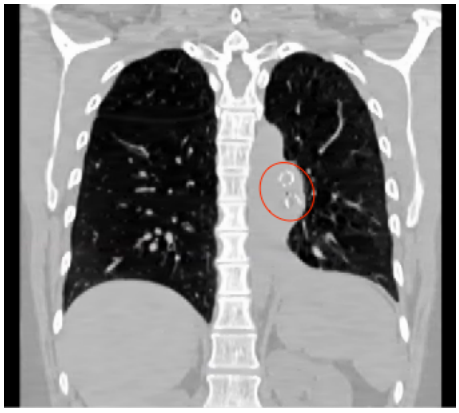
c)	d)

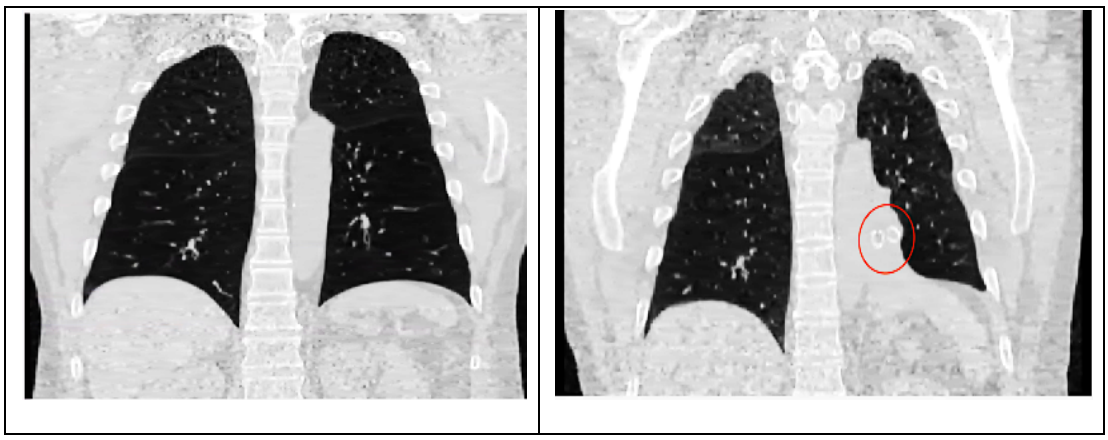

Figure 7-1: (a, c) Pre-BLVR and (b, d) post-BLVR CT images for two with identified endobronchial valves circled in red

	Displacement (mm)				DIR vs. Model Difference (mm)				Elasticity (kPa)			
	Pre		Post		Pre		Post		Pre		Post	
	Mean	Max	Mean	Max	Mean	Max	Mean	Max	Mean	Max	Mean	Max
Lobe 1	9.89 ± 3.47	27.83	14.91 ± 4.00	25.99	0.29 ± 0.44	4.97	0.14 ± 0.12	3.16	2.49 ± 1.44	8.00	2.87 ± 1.47	7.98
Lobe 2	13.44 ± 2.75	23.45	17.1 ± 3.22	31.28	0.6 ± 0.72	6.72	0.31 ± 0.44	4.46	3.56 ± 1.36	8.00	3.4 ± 1.44	7.99
Lobe 3	25.41 ± 6.49	53.70	29.67 ± 6.64	44.34	0.5 ± 0.6	6.00	0.3 ± 0.48	5.58	3.79 ± 1.23	8.00	4.06 ± 1.49	8.00
Lobe 4	11.43 ± 4.36	37.05	17.03 ± 5.64	37.20	0.34 ± 0.47	6.92	0.17 ± 0.25	3.43	2.58 ± 1.37	7.99	2.89 ± 1.57	8.00
Lobe 5	30.71 ± 7.46	50.59	32.57 ± 6.49	50.95	0.59 ± 0.75	8.45	0.16 ± 0.24	2.84	3.89 ± 1.1	8.00	4.47 ± 1.67	8.00

Table 7-1: Lobe-wise mean and max DIR displacement, DIR/Model displacement disagreement, and elasticity values calculated for pre- and post-interventional datasets

7.2.5 Post-BLVR Anatomy and Outcome Prediction

In addition to these post-BLVR image datasets, we have also obtained corresponding radiographically determined RV and TLC target lobe and whole lung volume measurements calculated for baseline and 6-month follow-up, collected as part of the VENT trial.[40,167] We are interested in using this new data to validate the ability to predict post-interventional geometry and PFT values. This data has been instrumental in identifying the challenges we face in further developing our approach to achieving this goal.

One initially observed challenge is in the ability to predict the post-procedural lung boundary conditions correctly and consistently. Other challenges include properly accounting for diaphragmatic changes and the presence and effect of collateral ventilation, which has been identified as an important indicator for outcome prediction.[168] The reshaping of anatomy in the thoracic region can be unpredictable due to mediastinal shifts, the appearance of scar tissue, or large changes in the contralateral lung volume.

Current Challenges	Potential Approaches
1. Boundary condition predictions	• Machine learning (with sufficient training data) • Physiologically informed model • Incorporate patient-specific characteristics, treatment plan information, and intended outcome[169]
2. Modeling of diaphragm and muscle group influence	• Investigate muscle group participation in breathing efforts • Measure respiratory muscle blood flow using near-infrared spectroscopy (NIRS)[170] • Monitor phrenic nerve stimulation driving diaphragm function with a diaphragm electromyogram (EMG)[171]
3. Collateral Ventilation[172]	• Explore currently available tools[173] • Investigate the directionality of deformation vectors at lobe boundaries generated in DIR • Region growth algorithms for identification of lobe fissure completeness

Table 7-2: Current challenges and potential solutions to integrated post-procedural outcome and PFT prediction tool

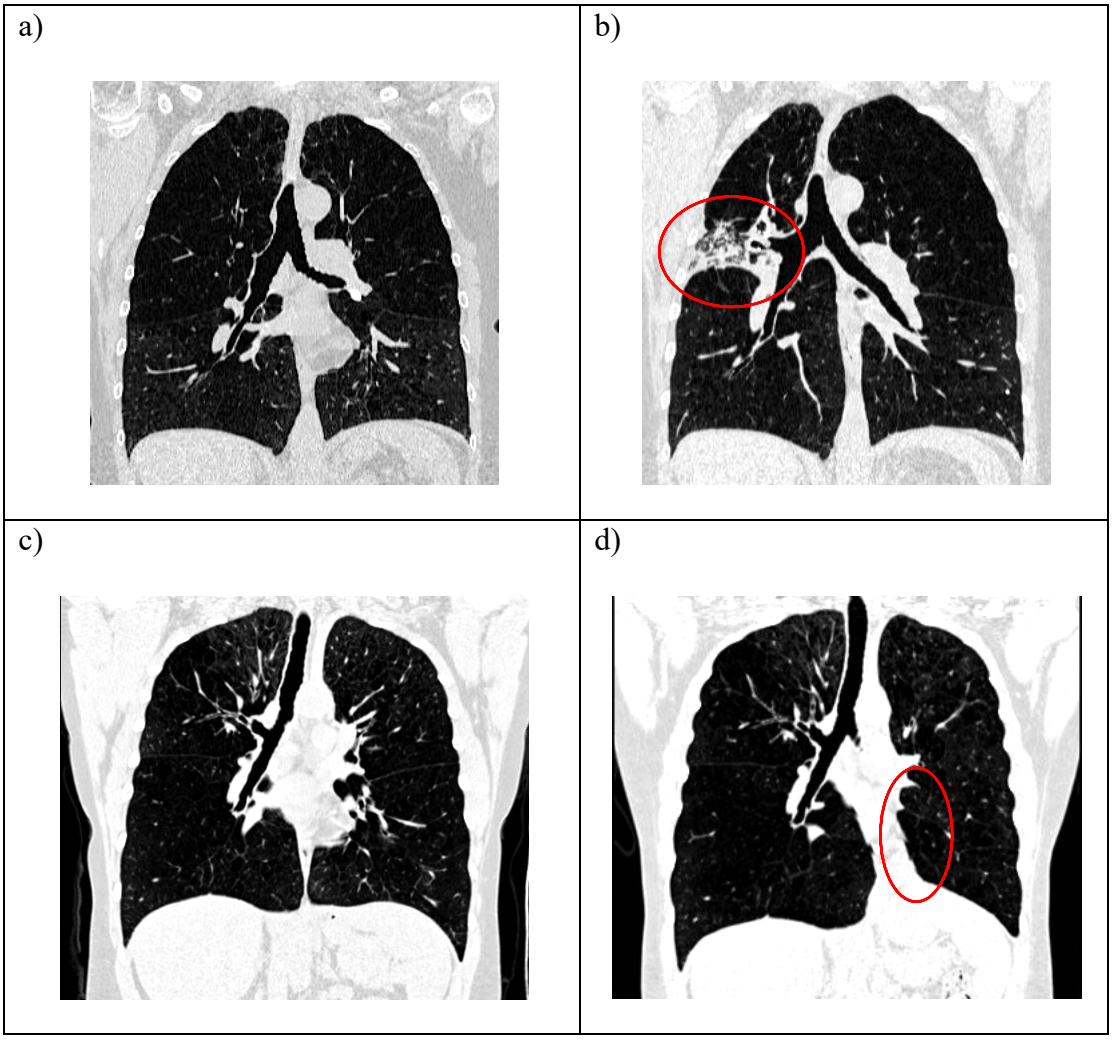

Figure 7-2: (a, c) Pre-BLVR and (b, d) post-BLVR CT images with boundary condition changes circled in red

Examples of boundary condition changes are displayed in Figure 7-2. Pre-interventional anatomies are shown in 7-2a and 7-2c and their corresponding post-treatment anatomies including the appearance of scar tissue and mediastinal anatomy shift in 7-2b and 7-2d, respectively. While the number of datasets available to us is currently too limited, we believe a machine learning approach could eventually provide accurate predictions of post-operative lung anatomy and

physiology. Table 7-2 presents an organized list of current challenges and potential areas of investigation to be explored in future works. This knowledge may further inform our approach to modeling lung intervention procedures.

References

1. Vinod SK, Hau E. Radiotherapy treatment for lung cancer: Current status and future directions. *Respirology.* 2020;25(S2):61-71.

2. Giuranno L, Ient J, De Ruysscher D, Vooijs MA. Radiation-Induced Lung Injury (RILI). *Frontiers in Oncology.* 2019;9.

3. Arroyo-Hernández M, Maldonado F, Lozano-Ruiz F, Muñoz-Montaño W, Nuñez-Baez M, Arrieta O. Radiation-induced lung injury: current evidence. *BMC Pulmonary Medicine.* 2021;21(1):9.

4. Palma DA, Senan S, Tsujino K, et al. Predicting Radiation Pneumonitis After Chemoradiation Therapy for Lung Cancer: An International Individual Patient Data Meta-analysis. *International Journal of Radiation Oncology*Biology*Physics.* 2013;85(2):444-450.

5. Zhou Z, Song X, Wu A, et al. Pulmonary emphysema is a risk factor for radiation pneumonitis in NSCLC patients with squamous cell carcinoma after thoracic radiation therapy. *Scientific Reports.* 2017;7(1):2748.

6. Ueki N, Matsuo Y, Togashi Y, et al. Impact of Pretreatment Interstitial Lung Disease on Radiation Pneumonitis and Survival after Stereotactic Body Radiation Therapy for Lung Cancer. *Journal of Thoracic Oncology.* 2015;10(1):116-125.

7. Papiez L, Timmerman R, DesRosiers C, Randall M. Extracranial stereotactic radioablation: physical principles. *Acta Oncol.* 2003;42(8):882-894.

8. Benedict SH, Yenice KM, Followill D, et al. Stereotactic body radiation therapy: The report of AAPM Task Group 101. *Medical Physics.* 2010;37(8):4078-4101.

9. Ng CSH, MacDonald JK, Gilbert S, et al. Optimal Approach to Lobectomy for Non-Small Cell Lung Cancer: Systemic Review and Meta-Analysis. *Innovations.* 2019;14(2):90-116.

10. Garner JL, Shah PL. Lung Volume Reduction in Pulmonary Emphysema. *Semin Respir Crit Care Med.* 2020;41(6):874-885.

11. van Geffen WH, Slebos DJ, Herth FJ, Kemp SV, Weder W, Shah PL. Surgical and endoscopic interventions that reduce lung volume for emphysema: a systemic review and meta-analysis. *Lancet Respir Med.* 2019;7(4):313-324.

12. Lee M, Mora Carpio AL. Lung Volume Reduction Surgery. In: *StatPearls.* Treasure Island (FL): StatPearls Publishing Copyright © 2022, StatPearls Publishing LLC.; 2022.

13. Patients at High Risk of Death after Lung-Volume–Reduction Surgery. *New England Journal of Medicine.* 2001;345(15):1075-1083.

14. An Update on Cancer Deaths in the United States. Centers for Disease Control and Prevention (CDC). https://www.cdc.gov/cancer/dcpc/research/update-on-cancer-deaths/ Published 2020. Accessed.

15. Leading Cancer Cases and Deaths. Centers for Disease Control and Prevention. https://gis.cdc.gov/Cancer/USCS/?CDC_AA_refVal=https%3A%2F%2Fwww.cdc.gov%2Fcancer%2Fdataviz%2Findex.htm#/AtAGlance/. Published 2018. Accessed.

16. Radiation Therapy for Non-Small Cell Lung Cancer. The American Cancer Society. https://www.cancer.org/cancer/lung-cancer/treating-non-small-cell/radiation-therapy.html. Published 2019. Accessed.

17. Delaney GP, Barton MB. Evidence-based estimates of the demand for radiotherapy. *Clin Oncol (R Coll Radiol).* 2015;27(2):70-76.

18. Hanania AN, Mainwaring W, Ghebre YT, Hanania NA, Ludwig M. Radiation-Induced Lung Injury: Assessment and Management. *Chest.* 2019;156(1):150-162.

19. Rancati T, Ceresoli GL, Gagliardi G, Schipani S, Cattaneo GM. Factors predicting radiation pneumonitis in lung cancer patients: a retrospective study. *Radiotherapy and Oncology.* 2003;67(3):275-283.

20. Kharofa J, Gore E. Symptomatic Radiation Pneumonitis in Elderly Patients Receiving Thoracic Irradiation. *Clinical Lung Cancer.* 2013;14(3):283-287.

21. Kimura T, Togami T, Takashima H, Nishiyama Y, Ohkawa M, Nagata Y. Radiation pneumonitis in patients with lung and mediastinal tumours: a retrospective study of risk factors focused on pulmonary emphysema. *The British Journal of Radiology.* 2012;85(1010):135-141.

22. Bahig H, Filion E, Vu T, et al. Severe radiation pneumonitis after lung stereotactic ablative radiation therapy in patients with interstitial lung disease. *Practical Radiation Oncology.* 2016;6(5):367-374.

23. Ireland RH, Tahir BA, Wild JM, Lee CE, Hatton MQ. Functional Image-guided Radiotherapy Planning for Normal Lung Avoidance. *Clinical Oncology.* 2016;28(11):695-707.

24. Hegi-Johnson F, de Ruysscher D, Keall P, et al. Imaging of regional ventilation: Is CT ventilation imaging the answer? A systematic review of the validation data. *Radiotherapy and Oncology.* 2019;137:175-185.

25. Vinogradskiy Y, Castillo R, Castillo E, et al. Results of a Multi-Institutional Phase 2 Clinical Trial for 4DCT-Ventilation Functional Avoidance Thoracic Radiation Therapy. *International Journal of Radiation Oncology*Biology*Physics.* 2022;112(4):986-995.

26. Yamamoto T, Kabus S, Bal M, Keall P, Benedict S, Daly M. The first patient treatment of computed tomography ventilation functional image-guided radiotherapy for lung cancer. *Radiotherapy and Oncology.* 2016;118(2):227-231.

27. Novel Lung Functional Imaging for Personalized Radiotherapy. ClinicalTrials.gov Identifier: NCT02308709. https://clinicaltrials.gov/ct2/show/NCT02308709. Updated August 18, 2021. Accessed.

28. Bucknell NW, Hardcastle N, Bressel M, et al. Functional lung imaging in radiation therapy for lung cancer: A systematic review and meta-analysis. *Radiotherapy and Oncology.* 2018;129(2):196-208.

29. Society AC. Surgery for non-small cell lung cancer.

30. Burt BM, Kosinski AS, Shrager JB, Onaitis MW, Weigel T. Thoracoscopic lobectomy is associated with acceptable morbidity and mortality in patients with predicted postoperative forced expiratory volume in 1 second or diffusing capacity for carbon monoxide less than 40% of normal. *J Thorac Cardiovasc Surg.* 2014;148(1):19-28, dicussion 28-29 e11.

31. Klapper JA, Hittinger SA, Denlinger CE. Alternatives to Lobectomy for High-Risk Patients With Early-Stage Non-Small Cell Lung Cancer. *Ann Thorac Surg.* 2017;103(4):1330-1339.

32. Agostini P, Lugg ST, Adams K, et al. Postoperative pulmonary complications and rehabilitation requirements following lobectomy: a propensity score matched study of patients undergoing video-assisted thoracoscopic surgery versus thoracotomydagger. *Interact Cardiovasc Thorac Surg.* 2017;24(6):931-937.

33. Howington JA, Blum MG, Chang AC, Balekian AA, Murthy SC. *Treatment of stage I and II non-small cell lung cancer: diagnosis and management of lung cancer, 3rd edition.* 2013.

34. Taylor MD, LaPar DJ, Isbell JM, Kozower BD, Lau CL, Jones DR. Marginal pulmonary function should not preclude lobectomy in selected patients with non-small cell lung cancer. *J Thorac Cardiovasc Surg.* 2014;147(2):738-744; Discussion 744-736.

35. Criner GJ, Sue R, Wright S, et al. A Multicenter Randomized Controlled Trial of Zephyr Endobronchial Valve Treatment in Heterogeneous Emphysema (LIBERATE). *Am J Respir Crit Care Med.* 2018;198(9):1151-1164.

36. Cooper JD, Trulock EP, Triantafillou AN, et al. Bilateral pneumectomy (volume reduction) for chronic obstructive pulmonary disease. *The Journal of Thoracic and Cardiovascular Surgery.* 1995;109(1):106-119.

37. Gaissert HA, Trulock EP, Cooper JD, Sundaresan RS, Patterson GA. Comparison of early functional results after volume reduction or lung transplantation for chronic obstructive pulmonary disease. *J Thorac Cardiovasc Surg.* 1996;111(2):296-306; discussion 306-297.

38. Meyers BF, Patterson GA. Chronic obstructive pulmonary disease • 10: Bullectomy, lung volume reduction surgery, and transplantation for patients with chronic obstructive pulmonary disease. *Thorax.* 2003;58(7):634.

39. Van Der Molen MC, Klooster K, Hartman JE, Slebos DJ. Lung volume reduction with endobronchial valves in patients with emphysema. *Expert Rev Med Devices.* 2018;15(11):847-857.

40. Endobronchial Valve for Emphysema Palliation Trial (VENT). ClinicalTrials.gov Identifier: NCT00129584. https://clinicaltrials.gov/ct2/show/NCT00129584. Updated August 18, 2009. Accessed.

41. Sciurba FC, Ernst A, Herth FJF, et al. A Randomized Study of Endobronchial Valves for Advanced Emphysema. *New England Journal of Medicine.* 2010;363(13):1233-1244.

42. Al-Mayah A, Moseley J, Velec M, Brock K. Toward efficient biomechanical-based deformable image registration of lungs for image-guided radiotherapy. *Phys Med Biol.* 2011;56(15):4701-4713.

43. Al-Mayah A, Moseley J, Hunter S, Brock K. Radiation dose response simulation for biomechanical-based deformable image registration of head and neck cancer treatment. *Phys Med Biol.* 2015;60(21):8481-8489.

44. Flynn C, Stavness I, Lloyd J, Fels S. A finite element model of the face including an orthotropic skin model under in vivo tension. *Comput Methods Biomech Biomed Engin.* 2015;18(6):571-582.

45. Bracq A, Delille R, Marechal C, Bourel B, Roth S, Mauzac O. Rib fractures prediction method for kinetic energy projectile impact: from blunt ballistic experiments on SEBS gel to impact modeling on a human torso FE model. *Forensic Sci Int.* 2019;297:177-183.

46. Hart RT, Hennebel VV, Thongpreda N, Van Buskirk WC, Anderson RC. Modeling the biomechanics of the mandible: a three-dimensional finite element study. *J Biomech.* 1992;25(3):261-286.

47. Al-Mayah A, Moseley J, Velec M, Brock KK. Sliding characteristic and material compressibility of human lung: parametric study and verification. *Med Phys.* 2009;36(10):4625-4633.

48. Chronic obstructive pulmonary disease (COPD) Key Facts. World Health Organization. www.who.int/en/news-room/fact-sheets/detail/chronic-obstructive-pulmonary-disease-(copd). Published 2017. Accessed June 3, 2019.

49. COPD Causes. Mayo Clinic. https://www.mayoclinic.org/diseases-conditions/copd/symptoms-causes/syc-20353679. Published 2017. Accessed June 3, 2019.

50. Hasse K, O'Connell D, Min Y, Neylon J, Low DA, Santhanam A. Estimation and validation of patient-specific high-resolution lung elasticity derived from 4DCT. *Medical Physics.* 2018;45(2):666-677.

51. Hasse K, Neylon J, Min Y, et al. Feasibility of deriving a novel imaging biomarker based on patient-specific lung elasticity for characterizing the degree of COPD in lung SBRT patients. *Br J Radiol.* 2019;92(1094):20180296.

52. Neylon J, Qi X, Sheng K, et al. A GPU based high-resolution multilevel biomechanical head and neck model for validating deformable image registration. *Medical Physics.* 2015;42(1):232-243.

53. Hasse K, Han F, Neylon J, et al. Estimation and validation of patient-specific liver elasticity distributions derived from 4DMR for radiotherapy purposes. *Biomedical Physics & Engineering Express.* 2018;4(4):045038.

54. Hasse K, Neylon J, Sheng K, Santhanam AP. Systematic feasibility analysis of a quantitative elasticity estimation for breast anatomy using supine/prone patient postures. *Med Phys.* 2016;43(3):1299.

55. Hasse KE. *Estimation and Incorporation of Organ-Specific Biomechanical Information Into Radiotherapy Treatment Planning* [Ph.D.]. Ann Arbor, University of California, Los Angeles; 2018.

56. Rabin C, Benech N. Quantitative breast elastography from B-mode images. *Medical Physics.* 2019;46(7):3001-3012.

57. Kennedy P, Wagner M, Castéra L, et al. Quantitative Elastography Methods in Liver Disease: Current Evidence and Future Directions. *Radiology.* 2018;286(3):738-763.

58. Zhou B, Bartholmai BJ, Kalra S, Osborn TG, Zhang X. Lung US Surface Wave Elastography in Interstitial Lung Disease Staging. *Radiology.* 2019;291(2):479-484.

59. Mariappan YK, Glaser KJ, Hubmayr RD, Manduca A, Ehman RL, McGee KP. MR elastography of human lung parenchyma: technical development, theoretical modeling and in vivo validation. *J Magn Reson Imaging.* 2011;33(6):1351-1361.

60. Mariappan YK, Glaser KJ, Levin DL, et al. Estimation of the absolute shear stiffness of human lung parenchyma using (1) H spin echo, echo planar MR elastography. *J Magn Reson Imaging.* 2014;40(5):1230-1237.

61. Marinelli JP, Levin DL, Vassallo R, et al. Quantitative assessment of lung stiffness in patients with interstitial lung disease using MR elastography. *J Magn Reson Imaging.* 2017;46(2):365-374.

62. Zhou B, Yang X, Zhang X, Curran WJ, Liu T. Ultrasound Elastography for Lung Disease Assessment. *IEEE Trans Ultrason Ferroelectr Freq Control.* 2020;67(11):2249-2257.

63. Sperandeo M, Trovato FM, Dimitri L, et al. Lung transthoracic ultrasound elastography imaging and guided biopsies of subpleural cancer: a preliminary report. *Acta Radiologica.* 2015;56(7):798-805.

64. Wu G, Lian J, Shen D. Improving image-guided radiation therapy of lung cancer by reconstructing 4D-CT from a single free-breathing 3D-CT on the treatment day. *Med Phys.* 2012;39(12):7694-7709.

65. Mecham RP. Elastin in lung development and disease pathogenesis. *Matrix Biology.* 2018;73:6-20.

66. Hasse K, Neylon J, Santhanam AP. Feasibility and quantitative analysis of a biomechanical model-guided lung elastography for radiotherapy. *Biomedical Physics & Engineering Express.* 2017;3(2):025006.

67. Stiehl B, Lauria M, O'Connell D, et al. A quantitative analysis of biomechanical lung model consistency using 5DCT datasets. *Med Phys.* 2020;47(11):5555-5567.

68. Low DA, Parikh PJ, Lu W, et al. Novel breathing motion model for radiotherapy. *Int J Radiat Oncol Biol Phys.* 2005;63(3):921-929.

69. Suki B, Ito S, Stamenovic D, Lutchen KR, Ingenito EP. Biomechanics of the lung parenchyma: critical roles of collagen and mechanical forces. *J Appl Physiol.* 2005;98(5):1892-1899.

70. Suki B, Bates JH. Extracellular matrix mechanics in lung parenchymal diseases. *Respir Physiol Neurobiol.* 2008;163(1-3):33-43.

71. Mikulski MA, Gerke AK, Lourens S, et al. Agreement between fixed-ratio and lower limit of normal spirometry interpretation protocols decreases with age: is there a need for a new GOLD standard? *J Occup Environ Med.* 2013;55(7):802-808.

72. Regan EA, Hokanson JE, Murphy JR, et al. Genetic epidemiology of COPD (COPDGene) study design. *Copd.* 2010;7(1):32-43.

73. Galban CJ, Han MK, Boes JL, et al. Computed tomography-based biomarker provides unique signature for diagnosis of COPD phenotypes and disease progression. *Nat Med.* 2012;18(11):1711-1715.

74. Boes JL, Hoff BA, Bule M, et al. Parametric response mapping monitors temporal changes on lung CT scans in the subpopulations and intermediate outcome measures in COPD Study (SPIROMICS). *Acad Radiol.* 2015;22(2):186-194.

75. Risholm P, Ross J, Washko GR, Wells WM. Probabilistic elastography: estimating lung elasticity. *Inf Process Med Imaging.* 2011;22:699-710.

76. Low DA, White BM, Lee PP, et al. A novel CT acquisition and analysis technique for breathing motion modeling. *Phys Med Biol.* 2013;58(11):L31-36.

77. Dou TH, Thomas DH, O'Connell DP, Lamb JM, Lee P, Low DA. A Method for Assessing Ground-Truth Accuracy of the 5DCT Technique. *International Journal of Radiation Oncology*Biology*Physics.* 2015;93(4):925-933.

78. Thomas DH, Ruan D, Williams P, et al. Is there an ideal set of prospective scan acquisition phases for fast-helical based 4D-CT? *Physics in Medicine and Biology.* 2016;61(23):N632-N641.

79. Hasse K, O'Connell D, Min Y, Neylon J, Low DA, Santhanam A. Estimation and validation of patient-specific high-resolution lung elasticity derived from 4DCT. *Med Phys.* 2018;45(2):666-677.

80. Karimi R, Tornling G, Forsslund H, et al. Lung density on high resolution computer tomography (HRCT) reflects degree of inflammation in smokers. *Respir Res.* 2014;15(1):23-23.

81. Booth AJ, Hadley R, Cornett AM, et al. Acellular normal and fibrotic human lung matrices as a culture system for in vitro investigation. *Am J Respir Crit Care Med.* 2012;186(9):866-876.

82. Du K, Bayouth JE, Cao K, Christensen GE, Ding K, Reinhardt JM. Reproducibility of registration-based measures of lung tissue expansion. *Medical Physics.* 2012;39(3):1595-1608.

83. Tehrani JN, Wang J. Mooney-Rivlin biomechanical modeling of lung with Inhomogeneous material. Paper presented at: 2015 37th Annual International Conference of the IEEE Engineering in Medicine and Biology Society (EMBC); 25-29 Aug. 2015, 2015.

84. White BM, Santhanam A, Thomas D, et al. Modeling and incorporating cardiac-induced lung tissue motion in a breathing motion model. *Medical Physics.* 2014;41(4):043501.

85. Timmerman R, Paulus R, Galvin J, et al. Stereotactic body radiation therapy for inoperable early stage lung cancer. *JAMA.* 2010;303(11):1070-1076.

86. Association AL. Lung Health and Diseases. www.lung.org/lung-health-and-diseases. Published 2016. Accessed 03-23, 2016.

87. Westover KD, Loo BW, Jr., Gerber DE, et al. Precision Hypofractionated Radiation Therapy in Poor Performing Patients With Non-Small Cell Lung Cancer: Phase 1 Dose Escalation Trial. *Int J Radiat Oncol Biol Phys.* 2015;93(1):72-81.

88. Chen H, Louie AV, Boldt RG, Rodrigues GB, Palma DA, Senan S. Quality of Life After Stereotactic Ablative Radiotherapy for Early-Stage Lung Cancer: A Systematic Review. *Clin Lung Cancer.* 2015.

89. Santhanam AP, Min YG, Mudur SP, et al. An inverse hyper-spherical harmonics-based formulation for reconstructing 3D volumetric lung deformations. *Cr Mecanique.* 2010;338(7-8):461-473.

90. Doyley MM. Model-based elastography: a survey of approaches to the inverse elasticity problem. *Phys Med Biol.* 2012;57(3):R35-73.

91. Krouskop TA, Wheeler TM, Kallel F, Garra BS, Hall T. Elastic moduli of breast and prostate tissues under compression. *Ultrason Imaging.* 1998;20(4):260-274.

92. Neylon J, Qi X, Sheng K, et al. A GPU based high-resolution multilevel biomechanical head and neck model for validating deformable image registration. *Med Phys.* 2015;42(1):232-243.

93. Santhanam AP, Imielinska C, Davenport P, Kupelian P, Rolland JP. Modeling real-time 3-d lung deformations for medical visualization. *IEEE Trans Inf Technol Biomed.* 2008;12(2):257-270.

94. Villard PF, Beuve M, Shariat B, Baudet V, Jaillet F. Simulation of lung behaviour with finite elements : Influence of bio-mechanical parameters. *Third International Conference on Medical Information Visualisation - BioMedical Visualisation (MediVis 2005), Proceedings.* 2005:9-14.

95. Al-Mayah A, Moseley J, Brock KK. Contact surface and material nonlinearity modeling of human lungs. *Phys Med Biol.* 2008;53(1):305-317.

96. Liu F, Tschumperlin DJ. Micro-mechanical characterization of lung tissue using atomic force microscopy. *J Vis Exp.* 2011(54).

97. Karami EG, S. ; Lee, T; Samini, A. A biomechanical approach for in vivo lung tumor motion prediction during external beam radiation therapy. *SPIE Proceedings.* 2015;9415(Medical Imaging 2015: Image-Guided Procedures, Robotic Interventions, and Modeling).

98. Doyley MM, Meaney PM, Bamber JC. Evaluation of an iterative reconstruction method for quantitative elastography. *Phys Med Biol.* 2000;45(6):1521-1540.

99. Hinz B. Mechanical aspects of lung fibrosis: a spotlight on the myofibroblast. *Proc Am Thorac Soc.* 2012;9(3):137-147.

100. Kallel F, Bertrand M. Tissue elasticity reconstruction using linear perturbation method. *IEEE Trans Med Imaging.* 1996;15(3):299-313.

101. Fu D, Levinson SF, Gracewski SM, Parker KJ. Non-invasive quantitative reconstruction of tissue elasticity using an iterative forward approach. *Phys Med Biol.* 2000;45(6):1495-1509.

102. Min Y, Neylon J, Shah A, et al. 4D-CT Lung registration using anatomy-based multi-level multi-resolution optical flow analysis and thin-plate splines. *Int J Comput Assist Radiol Surg.* 2014;9(5):875-889.

103. Qi XS, Santhanam A, Neylon J, et al. Near Real-Time Assessment of Anatomic and Dosimetric Variations for Head and Neck Radiation Therapy via Graphics Processing Unit-based Dose Deformation Framework. *Int J Radiat Oncol Biol Phys.* 2015;92(2):415-422.

104. Isola P, Zhu J, Zhou T, Efros A. Image-to-image translation with conditional adversarial networks. *Computer Vision and Pattern Recognition.* 2016.

105. Neilsen M. Neural Networks and Deep Learning. 2015.

106. Kline D, Berardi V. Revisiting squared-error and cross-entropy functions for training neural network classifiers. *Neural Computing & Applications.* 2005;14(4):310-318.

107. Hasse K, Hsieh SS, O'Connell D, et al. Systematic feasibility analysis of performing elastography using reduced dose CT lung image pairs. *Med Phys.* 2020;47(8):3369-3375.

108. Kubo T, Lin P-JP, Stiller W, et al. Radiation Dose Reduction in Chest CT: A Review. *American Journal of Roentgenology.* 2008;190(2):335-343.

109. Punnoose J, Xu J, Sisniega A, Zbijewski W, Siewerdsen JH. Technical Note: spektr 3.0—A computational tool for x-ray spectrum modeling and analysis. *Medical Physics.* 2016;43(8Part1):4711-4717.

110. Hasse K, Hsieh SS, O'Connell D, et al. Systematic feasibility analysis of performing elastography using reduced dose CT lung image pairs. *Medical Physics.* 2020;47(8):3369-3375.

111. Kubo T, Lin PJ, Stiller W, et al. Radiation dose reduction in chest CT: a review. *AJR Am J Roentgenol.* 2008;190(2):335-343.

112. Lauria M, Stiehl B, Santhanam A, et al. Analysis of Lobe-wise Regional Heterogeneity in Lung Ventilation and Tissue Elasticity Distributions for Lung Radiotherapy Patients with COPD. *Med Phys.* 2021(In Review).

113. Strange C, Herth FJF, Kovitz KL, et al. Design of the Endobronchial Valve for Emphysema Palliation Trial (VENT): a non-surgical method of lung volume reduction. *BMC Pulmonary Medicine.* 2007;7(1):10.

114. Valipour A, Herth FJF, Burghuber OC, et al. Target lobe volume reduction and COPD outcome measures after endobronchial valve therapy. *European Respiratory Journal.* 2014;43(2):387.

115. Brown MS, Kim HJ, Abtin FG, et al. Emphysema lung lobe volume reduction: effects on the ipsilateral and contralateral lobes. *European Radiology.* 2012;22(7):1547-1555.

116. Brown MS, Kim HJ, Abtin F, et al. Reproducibility of Lung and Lobar Volume Measurements Using Computed Tomography. *Academic Radiology.* 2010;17(3):316-322.

117. Vishnevskiy V, Gass T, Szekely G, Tanner C, Goksel O. Isotropic Total Variation Regularization of Displacements in Parametric Image Registration. *IEEE Transactions on Medical Imaging.* 2017;36(2):385-395.

118. Vishnevskiy V, Gass T, Székely G, Goksel O. Total Variation Regularization of Displacements in Parametric Image Registration. 2014; Cham.

119. Kemerink GJ, Lamers RJ, Pellis BJ, Kruize HH, van Engelshoven JM. On segmentation of lung parenchyma in quantitative computed tomography of the lung. *Med Phys.* 1998;25(12):2432-2439.

120. L Naumann, B Stiehl, M Lauria, K Singhrao, A Santhanam, Low D. A Quantitative Analysis of Lung Registration Error in a Clinically Used Deformable Image Registration Implementation Using Manually Identifiable Features in Fast Helical Free-Breathing CT Scans. *Medical Physics.* 2021;48(6):e117-e635.

121. Zhou W, Bovik AC, Sheikh HR, Simoncelli EP. Image quality assessment: from error visibility to structural similarity. *IEEE Transactions on Image Processing.* 2004;13(4):600-612.

122. Lauria M, Singhrao K, Stiehl B, et al. Automatic triangulated mesh generation of pulmonary airways from segmented lung 3DCTs for computational fluid dynamics. *Int J Comput Assist Radiol Surg.* 2021.

123. O'Connell DP, Thomas DH, Dou TH, et al. Comparison of breathing gated CT images generated using a 5DCT technique and a commercial clinical protocol in a porcine model. *Med Phys.* 2015;42(7):4033-4042.

124. O'Connell D, Shaverdian N, Kishan AU, et al. Comparison of lung tumor motion measured using a model-based 4DCT technique and a commercial protocol. *Practical Radiation Oncology.* 2018;8(3):e175-e183.

125. Baldi S, Ruffini E, Harari S, et al. Does lobectomy for lung cancer in patients with chronic obstructive pulmonary disease affect lung function? A multicenter national study. *J Thorac Cardiovasc Surg.* 2005;130(6):1616-1622.

126. Duman IE, Cimsit C, Yildizeli SO, Cimsit NC. Parenchymal density changes in acute pulmonary embolism: Can quantitative CT be a diagnostic tool? A preliminary study. *Clin Imaging.* 2017;41:157-163.

127. Disease GIfCOL. Pocket guide to COPD diagnosis, management, and prevention. http://goldcopd.org/wp-content/uploads/2016/12/wms-GOLD-2017-Pocket-Guide.pdf. Published 2017. Accessed.

128. Dou TH, Thomas DH, O'Connell DP, Lamb JM, Lee P, Low DA. A Method for Assessing Ground-Truth Accuracy of the 5DCT Technique. *Int J Radiat Oncol Biol Phys.* 2015;93(4):925-933.

129. Tang H, Zhang C, Xie X. Automatic Pulmonary Lobe Segmentation Using Deep Learning. Paper presented at: 2019 IEEE 16th International Symposium on Biomedical Imaging (ISBI 2019); 8-11 April 2019, 2019.

130. Doel T, Matin TN, Gleeson FV, Gavaghan DJ, Grau V. Pulmonary Lobe Segmentation from Ct Images Using Fissureness, Airways, Vessels and Multilevel B-Splines. *2012 9th Ieee International Symposium on Biomedical Imaging (Isbi).* 2012:1491-1494.

131. Doel T, Gavaghan DJ, Grau V. Review of automatic pulmonary lobe segmentation methods from CT. *Comput Med Imaging Graph.* 2015;40:13-29.

132. O'Connell D, Ruan D, Thomas DH, et al. A prospective gating method to acquire a diverse set of free-breathing CT images for model-based 4DCT. *Phys Med Biol.* 2018;63(4):04NT03.

133. Rintoul RC, Atherton R, Tweed K, Yates S, Chilvers ER. Exposure of patients to ionising radiation during lung cancer diagnostic work-up. *Thorax.* 2017.

134. Heinrich MP, Jenkinson M, Bhushan M, et al. MIND: Modality independent neighbourhood descriptor for multi-modal deformable registration. *Medical Image Analysis.* 2012;16(7):1423-1435.

135. Heinrich MP, Jenkinson M, Brady M, Schnabel JA. MRF-Based Deformable Registration and Ventilation Estimation of Lung CT. *IEEE Transactions on Medical Imaging.* 2013;32(7):1239-1248.

136. Santhanam AP, Stiehl B, Lauria M, et al. An adversarial machine learning framework and biomechanical model-guided approach for computing 3D lung tissue elasticity from end-expiration 3DCT. *Medical Physics.* 2020;n/a(n/a).

137. Isola P, Zhu J, Zhou T, Efros AA. Image-to-Image Translation with Conditional Adversarial Networks. Paper presented at: 2017 IEEE Conference on Computer Vision and Pattern Recognition (CVPR); 21-26 July 2017, 2017.

138. Neylon J, Min Y, Low DA, Santhanam A. A neural network approach for fast, automated quantification of DIR performance. *Med Phys.* 2017;44(8):4126-4138.

139. Dice LR. Measures of the Amount of Ecologic Association Between Species. *Ecology.* 1945;26(3):297-302.

140. Winckelmans T, Decaluwé H, De Leyn P, Van Raemdonck D. Segmentectomy or lobectomy for early-stage non-small-cell lung cancer: a systematic review and meta-analysis. *European Journal of Cardio-Thoracic Surgery.* 2020;57(6):1051-1060.

141. Lugg ST, Agostini P, Tikka T, et al. Long-term impact of developing a postoperative pulmonary complication after lung surgery. *Journal of Thoracic Surgery.* 2015;71:171-176.

142. British Thoracic S, Society of Cardiothoracic Surgeons of Great B, Ireland Working P. BTS guidelines: guidelines on the selection of patients with lung cancer for surgery. *Thorax.* 2001;56(2):89-108.

143. Na KJ, Kang CH, Jeon JH, et al. Quantification of emphysema with preoperative computed tomography has stronger association with pulmonary complications than pulmonary function test results after pulmonary lobectomy. *J Thorac Cardiovasc Surg.* 2014;147(3):915-920.

144. Kneuertz PJ, D'Souza DM, Moffatt-Bruce SD, Merritt RE. Robotic lobectomy has the greatest benefit in patients with marginal pulmonary function. *J Cardiothorac Surg.* 2018;13(1):56.

145. Sifakis E, Neverov I, Fedkiw R. Automatic determination of facial muscle activations from sparse motion capture marker data. *ACM Transactions on Graphics.* 2005;24(3):417-425.

146. Dilorenzo PC, Zordan VB, Sanders BL. Laughing out loud: control for modeling anatomically inspired laughter using audio. *ACM Transactions on Graphics.* 2008;27(5):125:121-128.

147. Lee SH, Terzopoulos D. Heads up! Biomechanical modeling and neuromuscular control of the neck. *ACM Transactions on Graphics.* 2006;25(3):1188-1198.

148. Zordan VB. Breathe easy: model and control of simulated respiration for animation. *ACM Siggraph.* 2004:29-37.

149. Tsang W, Singh K, Fiume E. Helping hand: An anatomically accurate inverse dynamics solution for unconstrained hand motion. *ACM Siggraph.* 2005:319-328.

150. komura T, Shinagawa Y, Kunii TL. Creating and retargeting motion by the musculoskeletal human body model. *The visual computer.* 2000;16(5):254-270.

151. Santhanam AP, Fidopiastis CM, Anton J, Rolland JP. Pneumothorax influenced 3D lung deformations. *Stud Health Technol Inform.* 2006;119:480-485.

152. Gao L, Parker KJ, Lerner RM, Levinson SF. Imaging of the elastic properties of tissue--a review. *Ultrasound Med Biol.* 1996;22(8):959-977.

153. Santhanam AP, Min Y, Mudur SP, et al. An inverse hyper-spherical harmonics-based formulation for reconstructing 3D volumetric lung deformations. *Cr Mecanique.* 2010;338(7):461-473.

154. Hasse K, Neylon J, Sheng K, Santhanam AP. Systematic feasibility analysis of a quantitative elasticity estimation for breast anatomy using supine/prone patient postures. *Med Phys.* 2016;43(3):1299-1311.

155. Hasse K, Neylon J, Santhanam A. Feasibility and quantitative analysis of a biomechanical model-guided lung elastography for lung radiotherapy". *Journal of Biomedical Physics and Engineering Express.* 2017.

156. Seyfi B, Santhanam A, Ilegbusi O. Effect of gravity on human lung deformation. Paper presented at: ASME International Mechanical Engineering Congress and Exposition2015; Houston TX.

157. Santhanam A, Hasse K, Min Y, Neylon J, Low D. A deep neural network approach for near real-time lung tissue elasticity estimations from 4DCT imaging. *Journal of Medical Physics.* 2017;44(6):3161.

158. Valenta J, Ruzicka M, Cihak R. Modelling tissue behaviour based on hyperelasticity theory. *Biomed Mater Eng.* 1994;4(5):381-395.

159. Dou T, Min Y, Neylon J, Santhanam A. Fast simulated annealing and adaptive monte carlo sampling based parameter optimization for dense optical-flow deformable image registration of 4DCT lung anatomy. *SPIE Medical Imaging.* 2016;97860N-97860N-18.

160. Santhanam A, Min Y, Mudur SP, et al. An inverse hyper-spherical harmonics-based formulation for reconstructing 3D volumetric lung deformations. *Cr Mecanique.* 2010;338(7):461-473.

161. Santhanam AP, Stiehl B, Lauria M, et al. An Adversarial Machine Learning Framework and Biomechanical Model Guided Approach for Computing 3D Lung Tissue Elasticity from End-Expiration 3DCT. *Med Phys.* 2020.

162. West JB. *Respiratory physiology: The essentials.* Wolters Kluwer.

163. Keys A, Aravanis C, Blackburn H, et al. Lung function as a risk factor for coronary heart disease. *Am J Public Health.* 1972;62(11):1506-1511.

164. Luo JC, Hsu KH, Shen WS. Pulmonary function abnormalities and airway irritation symptoms of metal fumes exposure on automobile spot welders. *Am J Ind Med.* 2006;49(6):407-416.

165. Hasse K, Neylon J, Min Y, et al. Incorporating 4DCT-Based Elasticity Information As a Regional Physiological Representation for Function Preserving Lung SBRT Treatment Planning. *International Journal of Radiation Oncology*Biology*Physics.* 2019;105(1, Supplement):E718.

166. Lauria M, Singhrao K, Stiehl B, et al. Automatic triangulated mesh generation of pulmonary airways from segmented lung 3DCTs for computational fluid dynamics. *Int J Comput Assist Radiol Surg.* 2022;17(1):185-197.

167. Strange C, Herth FJF, Kovitz KL, et al. Design of the Endobronchial Valve for Emphysema Palliation Trial (VENT): a non-surgical method of lung volume reduction. *BMC pulmonary medicine.* 2007;7:10-10.

168. Klooster K, ten Hacken NHT, Hartman JE, Kerstjens HAM, van Rikxoort EM, Slebos D-J. Endobronchial Valves for Emphysema without Interlobar Collateral Ventilation. *New England Journal of Medicine.* 2015;373(24):2325-2335.

169. Welling JBA, Hartman JE, Augustijn SWS, et al. Patient Selection for Bronchoscopic Lung Volume Reduction. *Int J Chron Obstruct Pulmon Dis.* 2020;15:871-881.

170. Guenette JA, Vogiatzis I, Zakynthinos S, et al. Human respiratory muscle blood flow measured by near-infrared spectroscopy and indocyanine green. *J Appl Physiol (1985).* 2008;104(4):1202-1210.

171. Nair J, Streeter KA, Turner SMF, et al. Anatomy and physiology of phrenic afferent neurons. *J Neurophysiol.* 2017;118(6):2975-2990.

172. Terry PB, Traystman RJ. The Clinical Significance of Collateral Ventilation. *Ann Am Thorac Soc.* 2016;13(12):2251-2257.

173. Welling JBA, Klooster K, Hartman JE, et al. Collateral Ventilation Measurement Using Chartis: Procedural Sedation vs General Anesthesia. *Chest.* 2019;156(5):984-990.